NASA Technical Memorandum 110382

Temperature, Pressure, and Infrared Image Survey of an Axisymmetric Heated Exhaust Plume

Edward L. Nelson, J. Robert Mahan, Larry D. Birckelbaw, Jeffrey A. Turk, Douglas A. Wardwell, and Craig E. Hange

February 1996

National Aeronautics and
Space Administration

NASA Technical Memorandum 110382

Temperature, Pressure, and Infrared Image Survey of an Axisymmetric Heated Exhaust Plume

Edward L. Nelson, Defense Group Inc., Moffett Field, California
J. Robert Mahan, Virginia Polytechnic Institute and State University, Blacksburg, Virginia
Larry D. Birckelbaw, Jeffrey A. Turk, Douglas A. Wardwell, and Craig E. Hange,
Ames Research Center, Moffett Field, California

February 1996

National Aeronautics and
Space Administration

Ames Research Center
Moffett Field, California 94035-1000

Contents

		Page
List of Tables		vi
List of Figures		vii
Nomenclature		x
Summary		1
1.0	Introduction	1
1.1	Motivation	1
1.2	Goal	3
2.0	Experiment	4
2.1	Background	4
2.2	Facility	5
2.3	Description of Test Equipment	5
2.3.1	Large Two-Axis Traverse	5
2.3.2	Small Three-Axis Traverse	6
2.3.3	Motor Controller for the Small Traverse	6
2.3.4	Motor Controller for the Large Traverse	6
2.3.5	Modified Auxiliary Power Unit	6
2.3.6	Flow Straightener	6
2.3.7	Combination Kiel and Thermocouple Probe	7
2.3.8	Thermocouple Calibration Unit	7
2.3.9	Kiel Probe Calibration Unit	7
2.3.10	Signal Conditioning Unit	7
2.3.11	Data Acquisition System	7
2.3.12	On-the-Fly Plotting of Data	8
2.3.13	Weather Station	8
2.3.14	Agema Infrared Imaging System	8
2.3.15	Mylar Backdrop	9
2.3.16	Midac System	9
2.4	Experimental Procedures	9
2.4.1	Open Gates to the OARF	9
2.4.2	Open Trailer and OARF Bunker	9
2.4.3	Uncover Test Equipment	10
2.4.4	Set Up the Aluminized Mylar Backdrop	10
2.4.5	Attach Probe to the Three-Dimensional Traverse	10
2.4.6	Reattach Motor Controllers	10
2.4.7	Set Up the Infrared Imaging System	10
2.4.8	Power-up Computer Systems	10

2.4.9 Take Weather Data 10
2.4.10 Pre-Experiment Test Meeting 11
2.4.11 Check-Out of Data Acquisition System 11
2.4.12 Turn On Fuel Pumps 11
2.4.13 Turn On 28-Vdc Power Rectifier 11
2.4.14 Warm-Up of APU 11
2.4.15 Level and Straighten Exhaust Nozzle 11
2.4.16 Establish Probe "Home" Position 11
2.4.17 Re-Start APU and Allow for "Warm-Up" 11
2.4.18 Take Data Point "Home" Position 11
2.4.19 Take Infrared Data of the APU Exhaust Plume 11
2.4.20 Begin Taking Data 12
2.4.21 Visual Inspection of the Probe Position 12
2.4.22 Save Data Regularly 12
2.4.23 Turn Off the APU 12
2.4.24 Record Position of the Test Equipment 12
2.4.25 Turn Off the 28-Vdc Power Rectifier 12
2.4.26 Secure the Fuel Pumping Station 12
2.4.27 Dismantle the Aluminized Mylar Backdrop 12
2.4.28 Store the Infrared Imaging System 13
2.4.29 Make Back-Up Copies of Survey Data 13
2.4.30 Secure OARF Bunker 13
2.4.31 Secure the Facility for Subsequent Tests 13
3.0 Results 13
3.1 Choice of the Coordinate System 13
3.2 Summary of Temperature and Pressure Data Taken 13
3.3 Uncertainty of Temperature Measurements 13
3.4 Uncertainty of Pressure Measurements 13
3.5 Data Clipping and Data Averaging 14
3.6 Probe Heating Study 14
3.7 Temperature and Pressure Data 14
3.7.1 Preliminary Experiment Data Compared to Dedicated Experiment Data 14
3.7.2 Higher Temperatures and Pressures Observed in the Dedicated Experiment 15
3.7.3 Asymmetries Observed in the Axisymmetric Plume 15
3.7.4 Limitation of x-Axis Data to Six Diameters Downstream 15
3.8 Velocity Profile 15
3.9 Weather Data 16
3.10 Infrared Image Data 16

3.10.1 Field Versus Frame 16
3.10.2 Measurement of a Dynamic System 16
3.10.3 MWB Image Data 16
3.10.4 Filtered MWB Image Data 16
3.10.5 LWB Image Data 17
3.10.6 Advantages of Time-Averaging 17
3.10.7 Infrared Image of the Backdrop 17
3.10.8 Plume Spread Angle 17
3.11 Validity of the Measured Infrared Image Data 17
3.12 Uncertainty of Measured Infrared Images 18
3.13 Midac Spectrometer Data 18
4.0 Infrared Image Prediction 19
4.1 History 19
4.2 How the Ray-Trace Method Works 19
4.3 Energy Computation 21
4.4 Line of Sight Method 21
4.5 Increasing the Number of Rays Per Pixel Improves the Quality of the Predicted Images 22
4.6 Effect of Exhaust Plume Constituents on the Predicted Infrared Image 23
4.6.1 Species Concentration Mapped to Total Temperatures 23
4.6.2 Carbon Dioxide Variance and Its Effect on the Predicted Infrared Image 23
4.7 LOS Image Compared to Filtered Experimental Data 23
4.8 Monte Carlo Ray-Trace Image Compared to Experimental Data 24
5.0 Conclusion and Recommendations 24
5.1 The Goal 24
5.2 The Experiment 24
5.3 Publication of Results 24
5.4 Public Access to Data 25
5.5 Recommendations for Future Work 25
Appendix A—Temperature and Pressure Data 27
Appendix B—Weather Data 61
Appendix C—Infrared Image Data File List 69
References 77
Tables 81
Figures 86

List of Tables

	Page
Table 1. Preliminary experiment data from May 14–15, 1993	81
Table 2. APU data measured from the exit plane through three diameters downstream	82
Table 3. APU data measured from three diameters downstream through ten diameters downstream	83
Table 4. Results from calibration of the Kiel probe	84
Table 5. Results from the Midac Spectrometer	85

List of Figures

		Page
Figure 1.	(a) Photograph of the McDonnell Douglas Harrier YAV-8B, and (b) MWB infrared image of the Harrier in a 30-ft (9.14-m) altitude and 30-kt (15.4-m/s) velocity flight condition	86
Figure 2.	Schematic diagram illustrating how the Monte Carlo ray-trace algorithm works	87
Figure 3.	(a) Photograph of the Boeing 747 Space Shuttle Carrier Aircraft, and (b) MWB infrared image of the Boeing 747	88
Figure 4.	Predicted infrared spectral image at 4.3 μm of the Boeing747 Space Shuttle Carrier Aircraft	89
Figure 5.	Photograph of the experimental equipment taken during the APU test at the OARF	90
Figure 6.	The large two-dimensional traverse used during the APU experiment at the OARF	91
Figure 7.	The small three-dimensional traverse rig shown attached to the larger two-dimensional traverse rig	92
Figure 8.	The auxiliary power unit (APU)	93
Figure 9.	The Hobart 480-to-28-Vdc power supply	94
Figure10.	The flow straightening assembly (ref. 20)	95
Figure 11.	The Zanker flow straightener (ref. 20)	96
Figure 12.	Combination thermocouple and Kiel probe	97
Figure 13.	The yaw and pitch angles of the Kiel probe	98
Figure 14.	The signal conditioning unit (SCU) with the top removed to show the linear and nonlinear thermocouple modules	99
Figure 15.	Flow chart of the Labview® data acquisition and analysis routine	100
Figure 16.	The weather station at the OARF	101
Figure 17.	The Agema 880 Dual Waveband Infrared Imaging System	102
Figure 18.	(a) Spectral response of the Agema 880 MWB camera, and (b) filtered response of the MWB infrared camera	103
Figure 19.	Spectral response of the Agema 880 LWB camera	104
Figure 20.	The aluminized Mylar backdrop	105
Figure 21.	Orientation of x-y-z axes with respect to the axisymmetric nozzle	106
Figure 22.	An example of conditioned temperature data showing "clipping"	107
Figure 23.	(a) Temperature and (b) Pressure profile as the probe enters and exits the exhaust flow	108
Figure 24.	Experimental temperature and pressure measurements obtained at the exit plane, z = 0.0 in.	109
Figure 25.	Experimental temperature and pressure measurements obtained one-half diameter downstream, z = 2.25 in.	110
Figure 26.	Experimental temperature and pressure measurements obtained one diameter downstream, z = 4.5 in.	111
Figure 27.	Experimental temperature and pressure measurements obtained two diameters downstream, z = 9.0 in.	112
Figure 28.	Experimental temperature and pressure measurements obtained three diameters downstream, z = 13.5 in.	113

Figure 29. Experimental temperature and pressure measurements obtained four diameters downstream, z = 18.0 in. 114
Figure 30. Experimental temperature and pressure measurements obtained five diameters downstream, z = 22.5 in. 115
Figure 31. Experimental temperature and pressure measurements obtained six diameters downstream, z = 27.0 in. 116
Figure 32. Experimental temperature and pressure measurements obtained seven diameters downstream, z = 31.5 in. 117
Figure 33. Experimental temperature and pressure measurements obtained eight diameters downstream, z = 36.0 in. 117
Figure 34. Experimental temperature and pressure measurements obtained nine diameters downstream, z = 40.5 in. 118
Figure 35. Experimental temperature and pressure measurements obtained ten diameters downstream, z = 45.0 in. 118
Figure 36. (a) Velocity profile at the exit plane, z = 0.0 in. (b) Velocity profile at one-half diameter downstream, z = 2.25 in. 119
Figure 37. (a) Velocity profile at one diameter downstream, z = 4.5 in. (b) Velocity profile at two diameters downstream, z = 9.0 in. 120
Figure 38. (a) Velocity profile at three diameters downstream, z = 13.5 in. (b) Velocity profile at four diameters downstream, z = 18.0 in. 121
Figure 39. (a) Velocity profile at five diameters downstream, z = 22.5 in. (b) Velocity profile at six diameters downstream, z = 27.0 in. 122
Figure 40. (a) Velocity profile at seven diameters downstream, z = 31.5 in. (b) Velocity profile at eight diameters downstream, z = 36.0 in. 123
Figure 41. (a) Velocity profile at nine diameters downstream, z = 40.5 in. (b) Velocity profile at ten diameters downstream, z = 45.0 in. 124
Figure 42. Illustration of the construction of a "field" of data 125
Figure 43. Three consecutively measured fields of filtered MWB infrared data 126
Figure 44. MWB infrared images of the APU exhaust plume 127
Figure 45. Filtered MWB infrared images of the APU exhaust plume 128
Figure 46. LWB infrared images of the APU exhaust plume 129
Figure 47. Averaged MWB infrared images of the APU exhaust plume 130
Figure 48. Infrared images of the aluminized Mylar backdrop 131
Figure 49. The uncertainty of a measured infrared image 132
Figure 50. Results from the Midac Spectrometer 133
Figure 51. The three-dimensional CFD solution space is reduced to a two-dimensional infrared image by the ray-tracing process 134
Figure 52. Diagram depicting how the initial orientation of a ray is decided 135
Figure 53. All possible outcomes for a ray as it traverses through the CFD solution space 136
Figure 54. Diagram depicting the path taken by a ray as it traverses a three-dimensional CFD solution cell 137

Figure 55. Illustration of the improvement in the quality of a predicted image as the number of rays per pixel increases 138

Figure 56. Predicted infrared images depicting the effect of varying the baseline carbon dioxide concentrations 139

Figure 57. Effect on intensity for a given pixel by varying the baseline carbon dioxide concentrations 140

Figure 58. Comparison between an infrared image predicted using the Line of Sight method and an experimental filtered-MWB image averaged over six frames of data 141

Figure 59. Comparison between an infrared image predicted using the Monte Carlo ray-trace code and an experimental filtered-MWB field of data 142

Nomenclature

A_i	Area of element i (m^2)
C_p	Pitot tube coefficient (-)
C	Species concentrations (-)
D_{ij}	Distribution factor from element i to element j (-)
E	Energy emitted or absorbed by element i within a differential wavelength band $d\lambda$, centered about λ (W)
$i'_{\lambda b}$	Spectral directional Planck blackbody radiation distribution function (W μm^{-1} m^{-2} sr^{-1})
K_p	Pitot tube constant (ft/s) $(M/R)^{0.5}$
M	Molecular weight (lbm/lbmol)
$N_{Si\,Sj}$	Number of rays emitted by surface i and absorbed by surface j
P_n	Pressure at point n (mm Hg)
Δp	Velocity head (in. H_2O)
$S(P_i)$	Average value at the centroid of a cell, P_i
s	Path length (cm)
T_n	Temperature at point n (°R)
u_n	Velocity at point n (ft/s)
V	Volume (m^3)
x,y,z	Cartesian coordinates
α_λ	Spectral absorptance (-)
ε_λ	Spectral emittance (-); spectral hemispherical emissivity (-)
λ	Wavelength (μm)
π	3.141593 (-)
σ	Standard deviation (-)
τ_λ	Spectral transmittance (-)
ω	Solid angle (sr)

Subscripts

S	Denotes a surface
V	Denotes a volume
λ	Denotes spectral dependence

Temperature, Pressure, and Infrared Image Survey of an Axisymmetric Heated Exhaust Plume

EDWARD L. NELSON,* J. ROBERT MAHAN,† LARRY D. BIRCKELBAW, JEFFREY A. TURK, DOUGLAS A. WARDWELL, AND CRAIG E. HANGE

Ames Research Center

Summary

The focus of this research is to numerically predict an infrared image of a jet engine exhaust plume, given field variables such as temperature, pressure, and exhaust plume constituents as a function of spatial position within the plume, and to compare this predicted image directly with measured data. This work is motivated by the need to validate Computational Fluid Dynamic (CFD) codes through infrared imaging. The technique of reducing the three-dimensional field variable domain to a two-dimensional infrared image invokes the use of an inverse Monte Carlo ray trace algorithm and an infrared band model for exhaust gases.

This report describes an experiment in which the above-mentioned field variables were carefully measured. Results from this experiment, namely tables of measured temperature and pressure data, as well as measured infrared images, are given. The inverse Monte Carlo ray trace technique is described. Finally, experimentally obtained infrared images are directly compared to infrared images predicted from the measured field variables.

1. Introduction

1.1 Motivation

The validation of Computational Fluid Dynamics (CFD) codes is important in the design of future generations of both military and civilian aircraft. Infrared imaging can be used as a validation tool for CFD codes, particularly for Short Take-Off and Vertical Landing (STOVL) aircraft. The validation technique involves a quantitative comparison between an experimental infrared image and a predicted infrared image, with the latter based on the CFD solution. This report describes the assembly of a data base which has been completed in support of an effort to validate CFD codes through infrared imaging. An experiment has been conducted in which the flow field of a modified auxiliary power unit (APU) has been surveyed, where temperature and pressure data, as well as corresponding infrared images have been obtained. Infrared images predicted from this data base are compared to experimentally obtained infrared images, thereby demonstrating an important step in the CFD code validation technique.

In recent years improved algorithms and advanced high-speed computers have led to increasingly complex CFD analyses. Complete Navier-Stokes analysis of such complex aerospace vehicles as the National Aeronautics and Space Administration's (NASA) Space Shuttle (ref. 1), the Stratospheric Observatory For Infrared Astronomy (SOFIA) Airborne Observatory (ref. 2), and the McDonnell Douglas Harder YAV-8B (ref. 3) have been successfully performed. However, validation of the predicted results for these complex aeropropulsive flow fields has been hampered by the lack of reliable test data. For example, definition of the complex jet-induced interactions produced by the Harrier operating in ground effect, obtained using conventional measurement techniques such as pressure transducers and thermocouples, has proven impractical due to the size scale and dynamic nature of the flow field. In addition, a critical need exists for validated CFD tools to ensure the successful design of nozzles and propulsion systems for future aircraft.

The motivation for the interest in STOVL aircraft stems from a requirement to operate aircraft, especially fighter aircraft, from a minimum operating airstrip or bomb-damaged runway. Interest in short-field takeoff capability extends from large land-based aircraft to aircraft carrier launch operations and ground-based remote forward-area operations. Current STOVL aircraft include vehicles such as the McDonnell Douglas Harrier AV-8B (ref. 4).

The aerodynamic flow field about a Harrier AV-8B operating in ground effect is difficult to model. In this flight regime, lift is augmented by four rotatable nozzles positioned fore and aft of the aircraft's center of gravity. Also, small reaction jets are located at the aircraft's nose, tail and wing tips. The ground effect flight regime is

*Defense Group Inc., Moffett Field, California.
†Virginia Polytechnic Institute and State University, Blacksburg, Virginia.

characterized by a small forward velocity component and regions of high subsonic to supersonic jet flows. The recirculating fluid dynamic interaction between the vectored jets, the ground, and the airframe can cause several effects including propulsion-induced loss of lift, or "suck down," ingestion of foreign objects or debris (FOD), and ingestion of warm, oxygen depleted, or vitiated, air (refs. 5–7). Attempts to model these effects by conventional means, such as wind-tunnel experiments, have been unsuccessful, with the end result being that full-scale powered tests are required to study the actual flow field.

The United State Air Force would like to replace the aging F-16 aircraft fleet. Also, the Navy would like to replace the A-6 and the Marines would like to replace the Harder AV-8B. In light of shrinking defense budgets, the United States government is considering a multirole tactical airplane to meet the requirements of the Air Force, Navy, and Marines (ref. 8). The US Advanced Research Project Agency (ARPA) hopes to award a STOVL Strike Fighter (SSF) contract in the late 1990s. Major airframe and engine companies are working now in hopes of making a successful bid for the ARPA contract. For example, wind-tunnel testing of an SSF model with lifting fan, made by British Aerospace and McDonnell Douglas, is planned for 1995 at NASA Ames (ref. 4). NASA Ames has been working in support of this effort in a wide variety of areas, particularly in the area of STOVL technology (ref. 9). Research activities include wind-tunnel testing of small-scale models (refs. 10–12), CFD modeling of critical flight regimes (refs. 13 and 14), and control and stability analysis in the Vertical Motion Simulator (VMS) (refs. 15 and 16).

The Powered-Lift Technology Branch at NASA Ames is directly involved in a number of STOVL initiatives. In support of their work in this area, an Agema Thermovision® Dual 880 Infrared Imaging System has been purchased in an effort to investigate the feasibility of using infrared imaging to validate CFD codes. The imaging system employs two scanning infrared cameras that are sensitive in the medium wavelength band (MWB), 2.5 to 5.5 μm, and in the long wavelength band (LWB), 8 to 12 μm. The infrared detectors are cryogenically cooled and provide a source temperature sensitivity on the order of 0.1 °C at 30.0 °C. The system operates by scanning a scene and digitally recording the infrared image to a hard disk (ref. 17). A thorough technical discussion of the Agema infrared imaging system is available from the Agema company (ref. 18). Also, the imaging system is discussed further in Section 2 of this report.

Since its delivery to NASA Ames in November of 1989, the Agema infrared imaging system has been useful as a nonintrusive measurement technique which provides real-time flow field images of sufficient detail to resolve the small- and large-scale flow structures and surface heating effects needed for the applications described above. The practicality of using infrared imaging as a means of examining these types of complex aeropropulsive flow fields has been demonstrated in a series of tests conducted at NASA Ames. Birckelbaw and Nelson (ref. 19) have shown the ability of an Agema system to resolve small- and large-scale flow structures, airframe surface heating, and interactions between the ground and plume. Inflight and ground-based infrared images of the Harrier YAV8B, the XV-15 Tiltrotor Aircraft, and the E-7 STOVL research model were shown to have value for the qualitative examination of the flow fields.

An example of the type of results which can be obtained from the infrared imaging system is shown in figure 1. Figure 1(a) shows an inflight photograph of the McDonnell Douglas Harrier YAV-8B and figure 1(b) shows a MWB experimental infrared image of the Harrier in a 30-ft (9.14-m) altitude and 30-kt (15.4-m/s) velocity flight condition. Because of the strong emission in the infrared, the hot-exhaust stream surrounding the aircraft is clearly visible. Also, the effects of ground heating and aircraft surface heating are visible. The "hot spots" which are visible on the fore and aft of the aircraft are exhaust ports, sometimes called "puffers." These "puffers" are used to maintain aircraft stability.

While the usefulness of infrared imaging as a flow-visualization tool is being explored, there exists a concurrent effort to better understand infrared imaging and modeling of exhaust plumes and gaseous radiation. Over the past six years joint research at NASA Ames and the Virginia Polytechnic Institute and State University (VPI&SU) has been underway to develop a computational technique which would permit quantitative use of measured infrared data for validation of advanced CFD codes (refs. 20–24). This research has concentrated on the development and validation of an inverse Monte Carlo radiative analysis technique that accurately generates a two-dimensional infrared image directly from an existing three-dimensional CFD solution.

The inverse Monte Carlo ray-trace algorithm was recently completed by Turk and co-workers (ref. 25). Figure 2 illustrates how the algorithm works. The computer code traces a ray from the detector of an infrared camera, through the CFD solution space, to some destination cell. The location of the destination cell is dependent upon the initial orientation of the ray, the absorptance of the destination cell, and the absorptance along the path from

the camera objective to the destination cell. The radiative contribution of each ray is computed based on the properties of the path traversed by the ray, and by the properties of the destination cell. Creating the two-dimensional infrared image involves tracing a large number of these rays for each pixel on a virtual two-dimensional image screen. Increasing the number of pixels and increasing the number of rays per pixel increases the accuracy of the predicted image, within the limits permitted by the resolution the CFD solution.

Development of this technique began with a proof-of-concept experiment by Hardman (refs. 20 and 21). In Hardman's experiment, an infrared image of an exhaust plume issuing from an APU was measured and compared with an image computed from the experimentally measured temperature distribution. A gas turbine-driven APU and an attached flow straightening assembly were used to create a uniform heated jet. A stepper-motor-driven combination Kiel and thermocouple probe was used to measure the pressure and temperature profiles at regular intervals downstream of the nozzle exit. Although the thermocouple probe was not corrected for conduction and an overly simple water-vapor-only band model was used to convert the measured temperature field into an infrared image, the experimental and predicted infrared images compared favorably. The results demonstrated the concept that infrared images could be generated from knowledge of the field variables and compared with experimentally obtained infrared images.

Hardman's experiment and results were successful and important enough to foster a continued research program in this area. Also, it was of interest to extend the ray-trace technique to the area of CFD code validation, particularly for STOVL applications. The next logical step to realizing the goal of predicting infrared images which can be compared quantitatively to experimental infrared images was to improve the water-vapor-only band model used in Hardman's computer program.

Over the past twenty years, considerable research has been done on infrared band models (refs. 26–30). Several commercial codes refs. 31 and 32) and a few company proprietary codes (ref. 33) are available. Each band model has its particular advantages; for example, some are best for high-temperature applications. In concert with the research objectives described above, Nelson (ref. 22) describes the selection of a public-domain infrared gaseous radiation band model which has been tailored for CFD code validation. In reference 22, Nelson describes the NASA Band Model, the band model published in NASA SP-3080, the Handbook of Infrared Radiation from Combustion Gases (ref. 34), and its improvement by implementing data tables from the North Atlantic Treaty Organization (NATO) Infrared Air Target Model (NIRATAM) (ref. 32). The improved band model includes the effects of water vapor, carbon dioxide, and carbon monoxide, the three gases which emit most strongly in the infrared. The improved band model provides constituents at a five-wavenumber resolution, a sufficiently high resolution for most CFD code validation applications.

The improved infrared band model has been incorporated into an inverse Monte Carlo ray-trace algorithm. The algorithm is similar to Hardman's code in that it reduces a three-dimensional solution field to a two-dimensional infrared image. However the latest algorithm, recently completed by Turk (ref. 25), operates directly on a generalized overset grid topology and CFD solution set. This means that the Monte Carlo technique, as it has been coded in the most recent computer program, can be applied to a variety of CFD solution sets.

A qualitative visual comparison between figures 3 and 4 indicates the most recent results from Turk's inverse Monte Carlo ray-trace code. Figure 3(a) shows a photograph of the Boeing 747 Space Shuttle Carrier Aircraft and figure 3(b) shows an experimental inflight infrared image of the same Boeing 747. The two red and white exhaust plumes, shown in figure 3(b), correspond with the inboard and outboard engines of the aircraft. Also, the reflected energy can be seen on the underside of the wing in figure 3(b). Notice that figure 3(b) is a MWB infrared image; the image is taken over the band of 2.5 to 5.5 μm.

Figure 4 is an infrared image which has been predicted from an existing CFD solution set about the Boeing 747 in a similar flight condition. A qualitative comparison between figure 3(b) and figure 4 reveals that the Monte Carlo algorithm is useful in identifying objects such as the fuselage, and for locating the size and structure of the exhaust plumes. The predicted image shown in figure 4 is a spectral image; the image is predicted at 4.3 μm. While a quantitative comparison between a broad-band image, such as the image shown in figure 3(b), and a spectral image, such as the image shown in figure 4, is not possible, the qualitative comparison between the two can be useful, particularly in identifying areas which may need improvement in the predicted CFD solution. The Monte Carlo algorithm and issues pertaining to infrared image prediction are discussed further in Section 4 and in reference 25.

1.2 Goal

Before the Monte Carlo algorithm can be used with confidence to validate a CFD solution, it too must be

validated. Such a process begins by generating a relatively simple CFD-like solution from a known temperature and pressure field. Next the Monte Carlo technique is used to predict an infrared image from the CFD- like solution. Finally, the predicted infrared image is compared with an experimentally obtained infrared image. It is the goal of the research described in this report to assemble the data base required for such a comparison.

Creating the CFD-like solution involves overlaying a known temperature and pressure field onto a CFD-like grid. The CFD-like grid is necessary because the Monte Carlo technique has been coded to directly interrogate a CFD solution. The data set that serves as the source for the temperature and pressure measurements must also include corresponding infrared images. The required data base of known temperature and pressure distributions, with corresponding infrared images, is not generally available.

This report describes an experiment which has been conducted in support of the research efforts described above. The experiment involves repeating Hardman's (refs. 20 and 21) experiment by conducting a complete temperature and pressure survey of the flow field exiting a gas turbine-driven APU. The experiment is unique and different from Hardman's work in that temperature and pressure surveys were taken simultaneously with corresponding infrared images. Also, efforts were made to ensure the accuracy and repeatability of the flow field surveys. The experiment was conducted in an effort to provide a data base from which the inverse Monte Carlo ray-trace technique and a potential CFD solution of this flow could be validated. Infrared images, temperature and pressure plots, velocity plots, and meteorological data from the experiment are given. Finally, infrared images predicted from these data using the inverse Monte Carlo ray-trace code are presented and compared to experimentally obtained infrared images.

2. Experiment

An experiment has been conducted in which an exhaust plume issuing from a modified auxiliary power unit (APU) has been surveyed. Exhaust flow exiting from both an axisymmetric and a rectangular nozzle were surveyed; however, only the axisymmetric data are given in this report. Temperature and pressure data were obtained using standard temperature and pressure probe techniques. Infrared images were obtained using a scanning infrared camera. The APU experiment is described in this section.

2.1 Background

In June 1989, Robert Hardman, a graduate student in Mechanical Engineering at VPI&SU, began work at NASA Ames with funding from NASA's postbaccalaureate program. One of Hardman's objectives during his eleven-month stay at NASA Ames was to prove the concept that infrared images could be predicted from a known temperature and pressure field. As a result of his work, which is thoroughly described in his Master of Science thesis (ref. 20), an APU was converted to provide an axisymmetric heated exhaust flow. Specifically, Hardman designed and attached a stainless steel flow straightening assembly and converging nozzle to the exhaust port of an APU (described in Sections 2.3.5 and 2.3.6). Hardman surveyed this exhaust flow with a combination thermocouple and Kiel probe. The results from this temperature and pressure survey were successfully used to predict an infrared image. Hardman completed his Master's degree in May 1990.

One month after Hardman graduated, Ed Nelson started graduate school in Mechanical Engineering at VPI&SU. During the following summer, in June 1991, Nelson started work at NASA Ames under the same postbaccalaureate program as Hardman. The focus of Nelson's work was the development of an infrared band-model which could be used for computational fluid dynamic (CFD) code validation applications; this work is described in his Master of Science thesis (ref. 22). Nelson's work was motivated by the need to improve upon the "weak link" in Hardman's infrared image generation code, the infrared band model.

Before Nelson returned to VPI&SU in January 1992 to complete his Master's degree, discussions between VPI&SU and NASA Ames revealed a need to develop a computer program which could predict infrared images directly from CFD solutions. Such a computer program would have applications for CFD code validation as well as infrared signature prediction for Department of Defense (DOD) applications. The computer program would be similar in concept to Hardman's code, but written differently to provide the user with options of image quality and image accuracy. An agreement was reached between Dr. J. Robert Mahan, a professor of Mechanical Engineering at VPI&SU, and Dr. Larry Birckelbaw, an aerospace engineer and civil servant at NASA Ames, that a graduate student from VPI&SU would begin work on this project.

In June 1992, Jeffrey Turk, a graduate student in Aerospace Engineering at VPI&SU, began work at NASA Ames. Turk's work focused on the development of a computer program which could predict infrared images from CFD solutions. The resulting computer code

incorporates a Monte Carlo-based ray-trace algorithm which can predict an infrared image directly from a CFD solution. This computer program is described further in Section 4 and in reference 25. During the first six months while Turk worked to develop this computer program, the need for a data base to validate this algorithm became apparent.

In January 1993, Nelson returned to NASA Ames with the objective of creating a data base which could be used to validate CFD codes, as well as to validate Turk's program for predicting infrared images. For these applications it was necessary that such a data base include a detailed temperature and pressure mapping of a heated exhaust flow. Corresponding infrared images of the exhaust flow were also necessary to complete the data set. By virtue of the accessibility to an infrared imaging system and the APU previously modified by Hardman, NASA Ames became the logical choice for an experiment site.

During the following fourteen months, from January 1993 to March 1994, Nelson worked to complete this data base. After acquiring the necessary experimental equipment and the personnel trained to operate that equipment, a preliminary experiment was conducted. On Thursday and Friday, May 14 and 15, 1993, Dr. Mahan visited NASA Ames to participate in the preliminary experiment. Six experimenters, including Dr. Mahan and Dr. Birckelbaw, tested the techniques required to conduct such an experiment.

From the preliminary experiment in May 1993, we learned that the outdoor testing should be conducted at night to avoid the high winds that are common in the summer afternoons of the San Francisco Bay Area. Concerning the acquisition of infrared images, testing at night offered the advantage of a decrease in background radiation over daytime testing. Also, we recognized the importance of leaving our equipment set up for the test; the assembly of the equipment required approximately sixteen man-hours of labor. Electrical interference between the power supply, bugs in the program for data acquisition, the requirement for a better backdrop for infrared data, the convenience of measuring atmospheric conditions, and personnel comfort were all factors that needed improvement for future tests. Several post-experiment meetings involving discussions among the experimenters on how to improve the process resulted in a much-improved experimental procedure.

During the week of July 12–16, 1993, the APU exhaust plume issuing from an axisymmetric nozzle was surveyed. The axisymmetric nozzle is shown as part of the flow straightening assembly which is described in Section 2.3.6. During the eight work days between October 18 and 27, 1993, the APU exhaust plume issuing from a rectangular nozzle was surveyed. Data from both APU experiments will be published in NASA Technical Memorandums (NASA TMs).

The rectangular nozzle data are not described in this report because of space limitations. One goal of this report is to show how the measured temperature and pressure data can be reduced to a CFD-like data file and subsequently used to predict an infrared image which is comparable to an experimentally obtained infrared image. That comparison is available only for the axisymmetric data set at this time. While the data from the rectangular nozzle experiment has been reduced, it has not yet been converted into a CFD-like data file. Once the CFD-like file has been created, some lead-time is necessary to debug the infrared image prediction computer program used to analyze the data file, a potentially time-consuming task. For these reasons only the axisymmetric data are presented here.

2.2 Facility

The experiment was conducted at the Outdoor Aerodynamic Research Facility (OARF) of the National Full-Scale Aerodynamics Complex (NFAC) at NASA's Ames Research Center at Moffett Field, California. A trailer and underground control room provided excellent storage for equipment such as computers and the data acquisition system. Also, these rooms provided personnel safety and minimum structure interference during the outdoor test. A 100-ft (30.5-m) square concrete pad provided an excellent place to conduct the experiment. A weather station was also located at the facility. Jet engine fuel, electricity, lighting, and safety equipment such as fire extinguishers and 911 service were also available at the OARF (ref. 35).

2.3 Description of Test Equipment

Figure 5 is a photograph taken during the APU experiment at the OARF. Equipment such as the aluminized Mylar backdrop, the large and small traverses, the APU, and combination temperature and pressure probe can be seen in the photograph. These items and other test equipment are described below.

2.3.1 Large Two-Axis Traverse– A large two-dimensional traverse, shown in figure 6, was used to position the probe and to support a smaller three-dimensional traverse rig. The traverse provided a maximum horizontal displacement of 40 in. (101.6 cm) and a maximum vertical displacement of 40 in. (101.6 cm). Covering an area of approximately 30 ft^2 (9.14 m^2) and having a mass of approximately 1200 lb (544 kg), the large traverse provided a very stable support structure for

other test equipment such as the smaller traverse and probe. A few modifications were made to the existing traverse rig specifically for this experiment. Namely, all of the wooden components were replaced by aluminum components, an improvement that was necessary to meet fire code safety requirements. The vertical and horizontal position adjustments to the large traverse were made using a Shaw Engineering motor-controller which is described in Section 2.3.4.

2.3.2 Small Three-Axis Traverse– A smaller three-dimensional traverse was "bolted" to the large traverse described in the preceding section. The smaller traverse was used to position the combination temperature and pressure probe within the exhaust stream. This traverse provided a freedom-of-movement of 18 in. (45.7 cm) in all three directions. The traverse could position the probe within the flow with an accuracy of ±0.001 in. (±0.025 mm) in all three directions. A Velmex motor-controller was used to operate the three stepper-motors of the traverse. Figure 7 is a photograph of the small three-dimensional traverse. Here, the small traverse is shown attached to the larger traverse for the experiment. The small traverse rig and the corresponding motor controller were on loan for this experiment from the Naval Post-Graduate School in Monterey, California (ref. 36).

2.3.3 Motor Controller for the Small Traverse– A Velmex 8300 Series Stepping Motor Controller/Driver was used to operate the small three-dimensional traverse (ref. 37). The controller utilized a RS-232C connector that accepted ASCII characters as input. The baud rate was switch-selectable between 50 and 9600 BPS. The Velmex controller was connected to the stepper motors of the small traverse by three relatively short cables. Because of the short cables, the controller was positioned on the shelf of the large two-dimensional traverse alongside the three-dimensional traverse. A digital display on the face plate of the controller showed the distance traveled by the probe from a pre-set home position. The motor controller could be operated directly from the face plate, or remotely from the trailer via a computer and cable.

2.3.4 Motor Controller for the Large Traverse– A Shaw Engineering motor-controller was used to position the large two-dimensional traverse rig. The controller could position the probe with an accuracy of ±0.001 in. (±0.025 mm) (ref. 38). A digital display on the face plate of the controller showed the distance traveled from a pre-set home position. Unlike the controller for the small traverse rig, this controller could not be operated remotely from computer. Adjustments to the large traverse were made at the controller itself, requiring someone to leave the test trailer and make traverse adjustments in a noisy test environment. Also, the motor-controller was designed to send output to only one motor. Consequently, two such controllers were required to operate the two-dimensional traverse rig. However, only one operational controller was available during APU experiment. If the large traverse needed to be moved in two directions, the cables leading from the controller to the motor had to be switched.

2.3.5 Modified Auxiliary Power Unit– An FAA Category II, Class B Gas Turbine Auxiliary Power Unit (APU) was utilized to produce the hot free-jet, or plume. The APU is an Airesearch Model GTCG30-142C manufactured by Garrett Auxiliary Power Division of the Allied Signal Aerospace Company (ref. 39). Attached to the nozzle exit is a flow-turning pipe, a diverging nozzle, and a flow-straightening assembly, which are described below. The APU was originally designed as an air-starter for larger jet engines. Modifications to the APU, namely the addition of a ten-gallon fuel tank and the flow straightening assembly, were made by Hardman (refs. 20 and 21). Figure 8 is a photograph of the APU in which the nozzle assembly and fuel tank can be seen.

The APU requires a continuous source of 28-Vdc power. This power was supplied by a 480-Vac-to-28-Vdc rectifier borrowed from the NFAC. Figure 9 is a photograph of the Hobart rectifier (ref. 40). Use of the rectifier, as opposed to other power-supply options such as a portable large-aircraft air-starter-system, decreased noise at the test site and reduced electrical interference to the data acquisition system.

The APU used JP-4, a jet engine fuel used in practically all European and U.S. military jets (ref. 41). The ten-gallon fuel tank was replaced, for this experiment, by a direct fuel line to a large 10,000 gal (37,854 l) tank at the OARF. Tapping into the large tank permitted the APU to be operated continuously, an improvement over earlier tests which offered a substantial time savings during the APU test. The APU start- and kill-engine switch was located on an attached instrument panel, along with an exhaust gas temperature gauge. An occasional visual inspection of the temperature gauge was required to make sure the APU did not overheat during continuous operation.

2.3.6 Flow Straightener– A flow-straightening section and axisymmetric exhaust nozzle assembly were added to the APU by Hardman (ref. 20). The straightening-assembly, shown in figure 10, includes a clamping flange and 90-deg elbow, a Zanker tube bank, an eddy-removal screen, and an axisymmetric nozzle. The assembly is constructed entirely from 20 gauge (0.035 in.) 304 stainless steel. An adjustable flow collar, designed to alleviate the additional back-pressure induced by the assembly, is installed immediately downstream of the 90-deg elbow. No problems, such as engine stalls due

to the added back-pressure from the assembly were encountered. For this reason the flow collar remained completely closed for all APU tests.

The Zanker tube bank, shown in figure 11, is positioned downstream of the 90-deg elbow and adjustable flow collar. The tube bank helps to straighten the exhaust flow (ref. 42). An eddy-removal screen positioned downstream of the tube bank serves to eliminate large-scale eddies. The stainless steel mesh has 450 wires per inch (177 wires/cm) in each direction of the screen. The design and fabrication of the straightener is discussed fully by Hardman (ref. 20).

2.3.7 Combination Kiel and Thermocouple Probe– A combination Kiel and thermocouple probe, shown in figure 12, was used to measure the total pressure and total temperature of the exhaust stream exiting the APU. The probe is 12.8 in. (32.5 cm) long and has a diameter of 0.188 in. (0.478 cm). The length and diameter of the probe were selected to provide adequate stiffness. Because of drag forces, stiffness was an important concern when attempting to maintain the probe's position in the flow; it was desired to keep the jet from deflecting the probe. A large aluminum brace was added to the base of the probe to increase its stiffness for this reason.

The Kiel probe was manufactured by the United Sensor Division of the United Electric Controls Co.; this company has since changed its name to the United Electric Controls Co., Flow Sensor Products Division (ref. 43). The yaw and pitch angles, defined in figure 13, of the flow entering the type-KA Kiel probe could vary up to ±50 deg without error in the total pressure reading. A true total pressure is indicated up to a Mach number of 1.0. Also, the probe is insensitive to Reynolds number except at extremely low velocities; the limiting velocity is approximately 4.0 ft/s. Errors introduced by turbulence are negligible, except for severe turbulence which may decrease slightly the acceptable range of the yaw and pitch angles (ref. 43). The type-KA Kiel probe was selected for the range of velocities encountered during the APU experiment. It is estimated that the yaw and pitch angles did not exceed 5 deg over the duration of the test.

The type-K, Chromel-Alumel, thermocouple is located 0.155 in. (3.96 mm) from the Kiel probe head. A second type-K thermocouple was used to monitor the ambient air temperature. Both thermocouples were connected to a signal conditioning unit, discussed in Section 2.3.10, which housed the thermocouple modules.

2.3.8 Thermocouple Calibration Unit– Calibration of the thermocouples was conducted using an Omega Hand-Held Calibration Unit, Model CL23-JKT Calibrator (ref. 44). The Calibration Unit checked the accuracy of the thermocouple by comparing the output voltage from the thermocouple to a reference voltage. The Calibration Unit provided an accuracy of 0.1 percent of the recorded temperature plus 1 °F. For example, if the recorded temperature was 800 °F, that measurement would be accurate to 1.8 °F.

2.3.9 Kiel Probe Calibration Unit– A pressure calibration unit (PCU) was used periodically during the experiment to test the response of the Kiel probe. The PCU was a DPI-605 manufactured by Druck Inc. (ref. 45). The unit was quoted as having an accuracy of 0.05 percent of full scale (30 psid max.), which implies accuracies of 0.015 psid. The unit was attached to the pressure lines with Swage fittings. A pressure-relief valve on the PCU was opened to "zero" the pressure reading. Next, the relief valve was closed and a pressure was applied. The pressures measured by the PCU and the pressure measured by the computer system were recorded. After a number of points, these values were compared. The process was repeated for each transducer. The PCU itself was calibrated just one week prior to the test.

2.3.10 Signal Conditioning Unit– A signal conditioning box (SCU), shown in figure 14, was constructed to house a series of analog signal conditioning modules. In the photograph of figure 14, the top cover of the SCU has been removed to show the linear and nonlinear thermocouple modules. These modules, Models 5B47, were manufactured by the National Instruments Co. (ref. 45). The modules have excellent noise resistance and amplification for millivolt sources. For the APU experiment, only the linear modules were used; these modules provided consistent treatment of the signal arriving from the thermocouples, unlike the nonlinear modules which were tried and gave erroneous and inconsistent results. The low-level input signal, in the millivolt range, arriving from the thermocouples was amplified to between 0 and +5 Vdc. The amplified voltage directly corresponds to a temperature between 0 and 500 °C. The modules were fully encapsulated and required no field adjustments.

2.3.11 Data Acquisition System– A Macintosh computer equipped with a National Instruments data acquisition board comprised the bulk of the data acquisition system used during the APU experiment. The acquisition board was a NB-MIO series board which featured an analog sampling rate of up to 100 KHz, 12-bit resolution, and 16 digital Input/Output channels (ref. 46). LabVIEW®, an icon-based programming software tool was also installed onto the hard drive of the Macintosh computer to interface between the computer and the data acquisition board. Figure 15 is a flow chart of the LabVIEW® data

acquisition and analysis routine as it was coded for the APU experiment. From the main routine, the experimenter could take dynamic data, establish probe zero position, and adjust the traverse; other functions are listed in figure 15. An experimenter could move the traverse, monitor channels in very near real time by observing histograms and x-y plots, graphically observe the probe position in relation to the nozzle, and select nozzle type (circular or rectangular), all from the main menu of the LabVIEW® software program.

2.3.12 On-the-Fly Plotting of Data– A personal computer (PC) was used to plot data on-the-fly during the APU experiment. Data were entered into a common spreadsheet program, Microsoft's Excel® (ref. 47) as they were obtained. A back-up copy of the data was created by virtue of manually entering the measured temperature and pressure results. The primary data collection was completed by the LabVIEW® data acquisition system. In addition to the spreadsheet itself, a current temperature plot and current pressure plot were each displayed on the PC monitor. Both the temperature and the pressure data plots were instantly updated upon data entry. By graphically visualizing the data as they were recorded, the experimenters gained additional insight into the validity of that data. For example, if the temperature and pressure decreased when it obviously should have increased, the experimenters would be alerted to check the probe's position.

2.3.13 Weather Station– Figure 16 is a photograph of the OARF's weather station. The weather station, located approximately 150-ft (45.7-m) from the test site, provided continuous data such as ambient temperature, relative humidity, wind speed, and wind direction. Two three-cup anemometers and an aerovane can be seen mounted on the weather station tower in figure 16. The aerovane can measure both wind speed and wind direction; a three-blade propeller rotates at a rate proportional to the wind speed while the streamlined shape and vertical fin keep the blades facing into the wind (ref. 48). The digitally displayed results from the weather station were available in the OARF bunker. The ambient weather conditions were manually recorded at regular 30-min intervals.

2.3.14 Agema Infrared Imaging System– An Agema Thermovision® Dual 880 Infrared Imaging System, shown in figure 17, was utilized to obtain infrared images of the APU exhaust plume. The imaging system employs two scanning infrared cameras that are similar in size to a hand-held video camcorder. The system is equipped with a data acquisition system, similar in size to a PC, and a color monitor and keyboard. Two sets of lenses are available for the infrared cameras; 20-deg lenses and 7-deg lenses provide a choice of field-of-view. The system operates on less than 400 W of 110-Vac power. The system is fully portable. The imaging system's tripod is equipped with a fluid-filled rotating head to minimize jerky movement while scanning.

The imaging system offers a variety of scanner modes; however, for the APU experiment the infrared cameras produced 25 images per second with 140×70 pixels per image. Each pixel of data is recorded with a full twelve-bit dynamic range. The infrared detector for the first camera is sensitive in the 2.5- to 5.5-μm wavelength band, which is referred to as the mid-waveband (MWB). The detector for the second infrared camera is sensitive from 4 to 13 μm; however, it is predominately sensitive from 7 to 12 μm, which is referred to as the long-waveband (LWB). Figure 18(a) shows the spectral response function of the MWB infrared camera, and figure 18(b) shows the response of the MWB camera when a narrow-band filter has been added to reduce the spectral bandwidth. Figure 19 shows the spectral response of the LWB infrared camera.

Each infrared camera employs a single cryogenically cooled detector element. The infrared detectors are constructed of indium antimonide (InAs) for the MWB camera, and mercury-cadmium-telludde (MCT) for the LWB camera. InAs and MCT are common infrared detector materials (ref. 49). The MWB detector provides a source temperature sensitivity of 0.1 °C at 30.0 °C, while the LWB detector provides a sensitivity of 0.05 °C at 30.0 °C. Both scanners have an accuracy of ±2 percent. To keep these detectors cooled during continuous operation, liquid nitrogen (LN_2) must be added to the cameras on an hourly basis.

The Agema system generates a multi-pixel infrared image by scanning a scene and digitally recording the infrared data to a hard disk (ref. 17). Up to 8 min of continuous MWB and LWB infrared data may be recorded on the 750 Mbyte internal hard disk. A 1/4-in. tape drive provides a medium for secondary storage. Infrared radiation arriving from the scene is received at the detector element through a rotating-mirror assembly. An internal calibration is set on each scan line by sweeping over a LN_2-cooled blackbody surface inside the camera. Measurement accuracy of the instrument is maintained by constantly monitoring internal temperature sensors, which compensate for detector-response drift by adjusting the gain.

The color monitor provides a windows-based tool for displaying live or recorded images. Post-processing analysis tools such as spotmeters, isothermal lines, and image subtraction are available with the software required to run the system. Various functions provide a means of manipulating the images, i.e., adjustments to level and

range, so that the operator can enhance certain features of the flow in the displayed image.

2.3.15 Mylar Backdrop– A cold and uniform background scene in an infrared image, such as those taken of the APU plume, can increase the quality of the image. For example, a cold or an apparently cold background will increase the contrast between the hot exhaust plume and the background. It is a goal that the low infrared emission of the background will not "wash-out," in the measured image, the small-scale structures of the exhaust plume, particularly those structures that exist near the shear layer created by the exhaust plume and the surrounding air.

Cold and uniform backgrounds can be created in a variety of ways. A water-cooled backdrop is common. Typically anti-freeze is added to the water, and the water is refrigerated to maintain temperatures below freezing. However, one problem with water-cooled backdrops is condensation, which tends to form on the face of the backdrop when the relatively warm and moist ambient air comes into contact with the cold face. Condensation in the form of water droplets can destroy the uniformity of the backdrop. Also, water-cooled backdrops typically include a pump, a heat exchanger, and a water reservoir, all of which complicate transportation and portability.

A reflective backdrop, shown in figure 20, was constructed for the APU experiment. In the visible spectrum as well as in the infrared, the reflective backdrop works like a mirror, reflecting the cold sky directly above the test site to the thermographic imaging system. The backdrop is relatively light-weight and it is portable; it can be easily moved by two people. The reflective material is aluminized Mylar, which is available at general hardware stores such as Tap Plastics in Mountain View, California (ref. 50). Mylar, a trademark of DuPont Corporation, is a thermoplastic film; aluminized Mylar has a thin film of aluminum on one surface of a Mylar sheet (ref. 51). The material is very thin, approximately 0.003 in. (0.076 mm) thick. Tightly stretching the aluminized-Mylar over a wooden frame created a flat surface. Such a flat surface, tilted at an angle of 45 deg, is necessary to ensure that only the sky above the test site is viewed. Even small ripples in this mirror-like surface were to be avoided because they would reflect other scenes about the test site, including the hot nozzle. Reflecting only a limited portion of the sky was necessary to maintain a uniform background.

The backdrop was positioned at a 45-deg angle with the ground plane for optimal reflection of the sky directly above the test site. In the MWB, the apparent temperature of the backdrop was approximately 55 °F (12.8 °C) and in the LWB the apparent temperature was –7 °F (–21.7 °C). Especially in the LWB case, the apparent temperature was lower, or better, than could be achieved by a comparable water-cooled system. Infrared images and further detailed results of the reflective-backdrop are given in Section 3.

2.3.16 Midac System– A Midac spectrometer, utilizing a plane-mirror Michelson-type interferometer, was used one night during the axisymmetric APU experiment to gather spectral data on the APU exhaust plume. The spectrometer is sensitive from 2.5 to 16 μm and has a resolution of 0.5 cm^{-1}. The system was used in conjunction with an infrared source and a laptop PC equipped with spectral analysis software (ref. 52).

An informal agreement between NASA Ames Research Center and the Lawrence Livermore National Laboratory (LLNL) in Livermore, California, arranged for Charles Bennett of LLNL to visit NASA Ames for the purpose of obtaining spectral data on the APU exhaust plume (ref. 52). Bennett and experimenters at both NASA Ames and LLNL were optimistic that data collected from the spectrometer would be useful in identifying concentrations of exhaust plume constituents such as carbon dioxide and water vapor. With this objective in mind, Charles Bennett of LLNL visited Ames Research Center during the APU preliminary experiment in May 1994, to get a "feel" for the experiment. During the July 1994 test, Bennett returned to Ames with the spectrometer to gather similar spectrometer data. Although results from the Midac spectrometer were inconclusive, a discussion of these results is given in Section 3.

2.4 Experimental Procedures

A typical night of experimentation would begin around 11:00 p.m. and end the following morning around 8:30 a.m. The routine followed by the researchers during the 9.5-hr period was the same throughout each session. An outline of a typical test session is provided here to give the reader greater insight into how the test was conducted and how the data were obtained. For the axisymmetric plume survey, only four researchers were available to do the jobs described below. With only a few exceptions, which are explained below, the work load of completing these tasks was equally shared among the four workers.

2.4.1 Open Gates to the OARF– The gates to the OARF were opened around 11:00 p.m. After the previous testing session, the gate to the facility was locked to discourage passers-by from interfering with equipment which remained set up for the duration of the test.

2.4.2 Open Trailer and OARF Bunker– Next, the trailer and OARF bunker were unlocked and the spotlights were turned on. The OARF has a large underground support bunker which is used during larger tests; the

bunker was constructed underground so that no structural interference would occur between the building and any above-ground test. This facility is heated and is equipped with a microwave oven and a rest room. Also, the digital readout of data from the weather station is available in this bunker. Two large mercury spotlights are powered from this room; the spotlights served to adequately light the test rig.

2.4.3 Uncover Test Equipment– After the mercury spotlights were illuminated, the canvas and plastic tarpaulins were removed from the traverse rigs and other equipment located outdoors. The tarpaulins were used to cover equipment such as the traverse rigs, the power rectifier, and the motors and motor controllers to protect these items from rain and dust.

2.4.4 Set Up the Aluminized Mylar Backdrop– The next task required two people to attach the aluminized Mylar sheet to the backdrop structure. The aluminized Mylar sheet is very thin and consequently cannot withstand the heavy breezes which blow during the afternoons between test periods. For this reason, after each morning of testing the Mylar was removed from the support structure. In order for the Mylar to reflect the cold sky as well as possible, it was necessary to tightly stretch the Mylar over the backdrop support to remove any wrinkles. The Mylar was held in place by duct tape which was spaced at regular intervals along the perimeter of the backdrop; one person would stretch and a second person would secure the Mylar to the backdrop with tape. Because the infrared emission from the duct tape was much greater than the radiation reflected from the backdrop, the duct tape, placed on top of the Mylar, provided a sharp contrast in the infrared. Consequently, the regular spacing of the duct tape provided a method for scaling the plume in the infrared image; the known and regular spacing of the duct tape resembles the markings on a ruler against the Mylar backdrop in the infrared images. This process of attaching the Mylar to the backdrop structure required at least twenty minutes.

2.4.5 Attach Probe to the Three-Dimensional Traverse– The next step involved attaching the combination temperature and pressure probe to the mounting block on the small three-dimensional traverse. The combination probe is a delicate and expensive transducer and was consequently treated with great care. The probe is mounted to a large aluminum block, which in turn is mounted to the small traverse. Two tightening screws secure the rear one-third of the probe to the aluminum block. The large aluminum block adds rigidity to the probe, helping the probe hold its position within the quasi-steady flow. Once the probe had been securely fastened to the aluminum block, the type-K thermocouple wire and pressure tube leading from the probe were connected to the wire and tube leading to the SCU. At this time a second probe was attached to the large traverse rig to measure ambient conditions.

2.4.6 Reattach Motor-Controllers– Next, the motor controller power cables were reattached and the controllers were turned on. The power cords were removed daily from the motor controllers in an effort to avoid accidents. A digital display on the face of the controller confirmed successful power-up self-test diagnostics.

2.4.7 Set Up the Infrared Imaging System– Each night the same person was responsible for setting up the infrared imaging system. These responsibilities included assembling the camera system, attaching the appropriate cables and lenses, obtaining the liquid nitrogen and attaching the cameras to the sturdy tripod. It was important that the subtleties of camera location and height did not vary from night to night. For this reason, duct tape was pasted on the concrete pad to mark the exact position of the legs of the tripod. A level on the head of the tripod was also used to establish camera position.

It was anticipated that by using the same operator to do these jobs, the job would be done consistently from night to night. This is especially true when taking data. When to take data, the duration of a data run, and the selection of lenses are each important operator decisions. By maintaining a consistent procedure throughout the test, the best possible data set was obtained. Also, post-processing was made easier by consistent data filename selection. Once the equipment had been set up, liquid nitrogen was added to the dewars in each of the cameras. After allowing a few minutes for the infrared detectors to cool, the system was turned on. By comparing the infrared scene created by the cameras to a scene taken from a previous night, final position adjustments were made to the camera to ensure consistent results from one testing session to the next. Finally, the experimenter would check the available space on the hard disk of the Agema system to make sure that sufficient data storage space was available for the evening's scheduled tests.

2.4.8 Power-up Computer Systems– An experimenter would turn on the power to the PC and Macintosh systems in the trailer. Successful boot-up of Microsoft Excel® and the National Instruments LabVIEW® software was verified.

2.4.9 Take Weather Data– At this point, the experimenters would begin taking weather data on the half-hour. The digitally displayed weather data such as wind-speed, wind-direction, ambient temperature, and relative humidity were available in the OARF bunker. An experimenter would walk into the bunker every half-hour

and record the displayed values on a pad of paper. The first data point was usually taken around 11:30 p.m., and the last point taken around 7:30 a.m.

2.4.10 Pre-Experiment Test Meeting– A pre-experiment test meeting was held each night to discuss the schedule of events. Personnel safety information as well as experiment objectives were reviewed. Results from the previous day's testing were shown and posted on a cork board inside of the trailer.

2.4.11 Check-Out of Data Acquisition System– Because of its important function, a thorough check of the Macintosh computer system and LabVIEW® data acquisition system was performed each night before testing began. One key item on the checklist was the verification that adequate data storage space was available on the removable hard disks that served as the primary data storage medium. On one particular night during the axisymmetric test, several hours of data were lost because we were writing to a full disk and had not programmed LabVIEW® to warn us of this error. Luckily, the average temperature and pressure data points were saved because of the manual data entry into the Excel® spreadsheet. Another important detail not to be overlooked was probe positioning. Occasionally, the probe would erroneously not move when it should have moved. For this reason, a complete checkout of the LabVIEW® system involved a visual inspection of the probe's position.

2.4.12 Turn On Fuel Pumps– A long fuel hose, approximately 100-ft (30.5-m) long, delivered fuel from a large, 10,000-gal (37,854 l) underground fuel tank to the APU. An experimenter would turn on the fuel pump at the pumping station and leave the fuel valve and pump switch accessible as a precautionary measure. Visual inspection of an in-line fuel pressure gauge was required to make certain that the line gage pressure of 12 lb_f/in^2. (82.7 kPa) remained constant throughout the experiment.

2.4.13 Turn On 28-Vdc Power Rectifier– A 480-Vac-to-28-Vdc power rectifier was used to convert the OARF 480-Vac electric service to the 28 Vdc power required to operate the APU. The alternative power source, a stand-alone 28-Vdc power supply, was extremely noisy (≈120 dB); the rectifier provided a relatively quiet alternative to this option. A 28-Vdc power source was required to run the fuel pump on the APU. For this reason, the rectifier was turned on before the APU was started.

2.4.14 Warm-up of APU– Next, an operator would start the APU and allow it to warm up. A visual inspection of the revolutions-per-minute (RPM) gauge and the exhaust-gas temperature (EGT) gauge was required to make certain the APU started correctly. A kill-engine switch, located near the RPM and EGT gauges, was actuated in the event the APU did not start correctly. Bad starts were sometimes caused by pockets of air in the fuel line. After the APU had "warmed-up," approximately fifteen minutes after start, the APU was turned off. At this point a relatively stable operating condition had been established. Also, the stainless steel exhaust nozzle and flow straightening assembly had heated to an equilibrium temperature and consequently expanded.

2.4.15 Level and Straighten Exhaust Nozzle– The level of the traverse was rechecked and if necessary, the exhaust nozzle of the APU was leveled and straightened. The level of the traverse rig was checked; it usually did not require adjustment after the initial leveling. Also, the level of the exhaust nozzle was checked. The straightness of the nozzle was checked using a plumb, which was hung from the probe and traverse rig. Making sure the nozzle was straight and level, as well as assuring that the probe traversed level and straight, was an important issue in successfully surveying the plume.

2.4.16 Establish Probe "Home" Position– After the level of the traverse rig and exhaust nozzle had been set, the probe was positioned at a "home" position. The position was measured near the exhaust nozzle exit. If the probe was positioned near this exit before the nozzle had expanded, the probe could be damaged by expansion of the nozzle. The "home" position was verified by visual inspection using a steel ruler.

2.4.17 Re-Start APU and Allow for "Warm-Up"– Next, the APU was restarted and thermal equilibrium attained. By viewing the on-line probe temperature reading, at this point centered at the exhaust exit, the experimenter could tell when a steady temperature had been obtained. Once the steady temperature was reached, five minutes elapsed before any data were recorded. The five minutes allowed for further nozzle expansion. At this point the APU was left running until some event warranted its shut down.

2.4.18 Take Data Point "Home" Position– The first data point recorded during a testing period usually occurred at the "home" position. This event served as a final check of successful system operation and gave the experimenters an indication of how the APU was running for that session. Depending upon the ambient temperature, the temperature at the "home" condition could vary as much as 20 °F (11 K) from session to session.

2.4.19 Take Infrared Data of the APU Exhaust Plume– Although one entire shift was dedicated to taking infrared data of the APU exhaust plume, additional infrared data were taken throughout the APU test. These data included, for example, images of the backdrop, start-up and

shut-down images, and images taken with and without the probe in the flow.

2.4.20 Begin Taking Data– Beginning with the first measured data point, the experiment was underway. The interaction between the LabVIEW® operator and the Excel® operator played an important role in the data acquisition process. To begin, the data points to be obtained during the nights work were listed on the Excel® spreadsheet. One column of that spreadsheet listed the axis movements required to reach the next data point. For example, that column may have read move +0.25 in. (+0.635 cm) in the x-direction. The Excel® operator would announce this traverse movement to the LabVIEW® operator, who in turn would click the appropriate icon on the terminal of the Macintosh to move the probe to that position. After a few seconds, an audible tone would alert both operators to the fact that the probe was on position. The current x-y-z position was displayed on the LabVIEW® screen so that the Excel® operator could double-check the probe position with the position listed on the spreadsheet.

Next, the LabVIEW® operator would watch the displayed average temperature. When that temperature had stabilized, i.e., when it was no longer increasing if going into the plume, or vice-versa for exiting the plume, then it was time to take data. The LabVIEW® operator would click the "take data" icon at this time. One hundred consecutive temperature and pressure measurements were then written to a removable hard disk. The average temperature and pressure measurements were displayed on the Macintosh terminal, where the average value was computed using the one hundred measured values. Extraneous data were removed by clipping those data that fell outside a two-standard-deviation window. The LabVIEW® operator would then announce those average values to the Excel® operator, who would in turn enter those values into the spreadsheet. Next, the Excel® operator would announce the subsequent traverse movement. This process was repeated until the experiment was stopped for some reason.

2.4.21 Visual Inspection of the Probe Position– Because no feedback was available on the position of the moving probe, a periodic visual inspection of the probe position was required. Two windows in the trailer gave the experimenters seated at the computers a view of the probe. However, it was generally required to look at the probe from close range to verify that it was correctly positioned.

2.4.22 Save Data Regularly– Because the standard timed-backup routine for the Excel® spreadsheet saved data too infrequently to satisfy the test crew, the experimenters frequently reminded each other to save data. Enough data was collected and entered into the spreadsheet between the standard timed-backups to assure that experimenters eagerly took a more active role in saving the data. Data were saved to a variety of filenames as an added precaution.

2.4.23 Turn Off the APU– When the final data point had been recorded, the APU was shut down. During a testing session, the APU was sometimes shut down for various reasons that included, but were not limited to, problems such as incorrect probe positioning, insufficient data storage space, high winds, or problems with the data acquisition system. Otherwise, the APU was left on until the end of the testing session.

2.4.24 Record Position of the Test Equipment– In an effort to ensure the repeatability of the experiment from one testing session to the next, daily measurements of the equipment position were made. For example, the position of the APU, the backdrop, the camera system and the traverse were all verified by using a tape measure. Photographs taken during the experiment also helped to document equipment position.

2.4.25 Turn Off the 28-Vdc Power Rectifier– After the APU had been shut down, the 28-Vdc power rectifier was turned off by actuating the appropriate switch on the instrument panel. The relatively hot rectifier had to cool down before it could be covered with a tarpaulin. The power cable leading from the rectifier to the APU was rolled up and safely stored on a rack on the side of the rectifier. The power cable leading from the rectifier to the 480-Vac power source was likewise stored in a rack on the side of the rectifier.

2.4.26 Secure the Fuel Pumping Station– After each testing session, the fuel pump power was turned off at the fuel pumping station. Next, the cover was returned to the fuel pit area which leads to the flow valves and fuel pump. This cover was removed during pump operation to give safety personnel easy access to the fuel pit area in the event of an accident. Finally, the fuel pump power switch was secured by locking the face-plate leading to the switch.

2.4.27 Dismantle the Aluminized Mylar Backdrop– The thin aluminized Mylar sheet was removed from the backdrop and stored in the trailer after each testing session. Care was taken to roll up the Mylar sheet only when the sheet was completely dry. Moisture, caused by an infrequent morning dew, would cause the Mylar to stick to itself when the sheet was rolled up, creating the possibility that the aluminum would separate from the Mylar when the sheet was unrolled. The duct tape used to secure the Mylar to the frame was carefully removed to prevent the sheet from tearing. The aluminum removed

by the duct tape posed no threat to the function of the backdrop because the duck tape was fastened to the Mylar only on the edges of the Mylar sheet. The large wooden backdrop frame was set on its side to prevent accidental damage to the frame caused by the strong winds that blew during the afternoons between tests.

2.4.28 Store the Infrared Imaging System– The infrared imaging system is an extremely delicate and expensive instrument. One cost estimate for replacing the system exceeds 200,000 U.S. dollars (ref. 54). For this reason, after each testing session the system was carefully repackaged and stored in a different building.

2.4.29 Make Back-Up Copies of Survey Data– The complete temperature and pressure data sets were saved on several removable optical diskettes. The average temperature and pressure data set was saved onto the hard drive of the PC. Back-up copies of this reduced data were made after each testing session by copying those files to a diskette. The diskettes were stored at a different location between tests. After the back-up copies were made, the computers were turned off. The keyboards to the computers were removed and stored in a different building for added security.

2.4.30 Secure OARF Bunker– The underground control room at the OARF was tidied and secured. The mercury spotlights were turned off. The last weather data were recorded and the weather conditions for the session were cataloged.

2.4.31 Secure the Facility for Subsequent Tests– The final wrap-up of events began by securing loose items in the trailer. The test equipment on the concrete pad was covered by replacing the plastic and canvas tarpaulins. Duct tape and nylon ropes were used to secure the tarpaulins. Around 8:30 a.m., the personnel would depart the OARF. The gate to the OARF was locked at this time.

3. Results

This section presents the results from the axisymmetric APU exhaust plume survey. Temperature and pressure plots, weather data, infrared data, and spectrometer data are shown and discussed.

3.1 Choice of the Coordinate System

A right-handed Cartesian coordinate system was selected for describing the APU exhaust plume. The x,y-axis plane is parallel with the exit plane of the exhaust nozzle. The positive z-axis begins at the exit plane of the nozzle and proceeds downstream along the centerline of the exhaust flow. Figure 21 shows the coordinate system in relation to the axisymmetric nozzle.

3.2 Summary of Temperature and Pressure Data Taken

Recall that two experiments were conducted (see Section 2.1) in which the flow exiting the axisymmetric nozzle was surveyed. The first experiment was a preliminary experiment conducted in May 1993, and the second experiment was a dedicated axisymmetric nozzle survey conducted in July 1993. Table 1 summarizes the data obtained during the preliminary experiment and tables 2 and 3 summarize the data obtained during the dedicated test. Notice from these tables that several repeatability runs were conducted to establish confidence in the measured data.

3.3 Uncertainty of Temperature Measurements

The temperature of the APU exhaust plume was measured using the combination temperature and pressure probe described in Section 2.3.7. The temperature probe was a type-K thermocouple, made of Chromel-Alumel. The probe was calibrated using the Omega Hand-Held Calibration Unit, Model CL23-JKT Calibrator (ref. 44), which is described in Section 2.3.8. The calibration unit provided an accuracy of 0.1 percent of the recorded temperature plus 1 °F. The thermocouple was calibrated one week prior to both the preliminary experiment in May and the dedicated APU experiment in July.

3.4 Uncertainty of Pressure Measurements

The pressure transducer portion of the combination temperature and pressure probe is also described in Section 2.3.7. The Kiel probe calibration unit is discussed in Section 2.3.9. The calibration unit provided an accuracy of 0.05 percent of full scale (30 psid max.), which implies accuracies of 0.015 psid. Table 4 lists a comparison between the pressures entered into the calibration unit and the corresponding pressures indicated by the Kiel probe. The percent difference between the pressure indicated by the Kiel probe and the pressure maintained by the calibration unit is listed in the third column of the table. The majority of the values listed in the third column show agreement within ±0.5 percent. In addition, it should be reported that maintaining a stable pressure on the calibration unit proved to be a fairly difficult task; the pressure would fluctuate between ±0.002 psid. This value is, however, within the implied

accuracy of 0.015 psid. The calibration unit itself was calibrated just prior to these measurements.

3.5 Data Clipping and Data Averaging

As mentioned in Section 2.3.11, the Labview® data acquisition system played a key role in the experiment. When the experimenters obtained a data point, one hundred essentially-instantaneous temperature and pressure measurements were recorded. These data were reduced to a single average temperature and average pressure value. The average temperature and pressure values were computed by averaging those data that fell within a two-standard-deviation, 2-σ, window. The standard deviation, σ, of the numbers was computed using the formula

$$\sigma = \sqrt{\frac{n\sum x^2 - \left(\sum x\right)^2}{n^2}} \qquad (1)$$

In equation 1, n is the number of data points and x is either the temperature or pressure. Once σ was computed, those data that fell outside of a 2-σ window were discarded. The process of removing extraneous data in this fashion is standard practice among experimental scientists at NASA Ames (ref. 36). The average temperature or pressure value, $\bar{x}$, was computed by averaging the remaining data by

$$\bar{x} = \frac{\sum x}{n^*} \qquad (2)$$

where n^* is the number of remaining data points.

An illustration of the clipping process is shown in figure 22. Here, data falling above 745.2 °F or below 742.9 °F have been "clipped" or removed. The variance of these data, temperature or pressure, is a consequence of taking measurements on a dynamic system. Although the flow was straightened and the system was relatively stable, it is reasonable to expect some fluctuation in the temperature and pressure values. This phenomenon was also observed in the infrared data and is explained further in Section 3.10.1.

3.6 Probe Heating Study

A simple experiment was conducted to investigate the effect of probe heating, i.e., to determine the effect, if any, the heating of the probe by the exhaust stream had on the measured temperature and pressure data. For this test, the probe was caused to traverse the flow by inserting the probe into the flow from the ambient air to the centerline of the exhaust stream. Temperature and pressure measurements were obtained at regular intervals during the traverse. After reaching the center of the flow, the probe was traversed backwards along the insertion line, i.e., the probe was traversed from the center of the flow to the ambient air. Temperature and pressure measurements were made at the same locations along the traverse line. A comparison of the data between the two traverses should reveal the effect heating of the probe by the exhaust stream would have on the measured data. For example, for the same spatial position in the exhaust stream, the probe would likely yield a cooler temperature on the entering traverse than on the exiting traverse due to heating of the probe by the exhaust stream.

Figure 23 shows the results from this experiment obtained during the rectangular nozzle case (no such study was conducted for the axisymmetric case). The rectangular nozzle is different from the axisymmetric nozzle in that less of the probe length is heated by the flow. However, an approximately ten percent warmer centerline temperature present in the rectangular nozzle should exaggerate the effects of heating. Figure 23(a) shows the measured temperature data during the entering and exiting traverses, while figure 23(b) shows the measured pressure data. The data obtained during the entering and exiting sweeps agree remarkably well. The favorable comparison between these data gives us confidence that the data sampling rate was sufficiently slow enough to allow the probe to properly cool on the exiting traverse.

3.7 Temperature and Pressure Data

The results from the temperature and pressure measurements are shown in figures 24–35. Figure 24 shows results at the exit plane, figure 25 shows results at one-half diameter, and figures 26–35 show results from one to ten diameters downstream at regular one diameter intervals. Where applicable, data from the preliminary experiment are shown. In general, the y- or x-axis location is shown on the horizontal axis of each graph, and the temperature or pressure is shown on the vertical axis. Each figure is a summary of all average temperature and pressure measurements obtained at a particular z-axis location. Recall that a summary of these data is given in tables 1–3. Appendix A includes forty tables that list the experimentally obtained temperature and pressure data that are presented in figure 24 –35. These tables are referenced in the caption of each figure.

3.7.1 Preliminary Experiment Data Compared to Dedicated Experiment Data– In figure 24, temperature and pressure data are presented for both y-axis and x-axis sweeps. These data are compared to measurements obtained during the preliminary experiment and are

consequently labeled, for example, "prelim. run 1." Notice that the trends of the curves from both the preliminary experiment and the dedicated experiment are similar. Because Run 1 and Run 2 fall nearly on top of one another, we have an additional degree of confidence in the measured data. The same is true for the preliminary experiment data.

3.7.2 Higher Temperatures and Pressures Observed in the Dedicated Experiment– A comparison between the preliminary experimental data and data from the dedicated test reveals that higher temperatures and pressures were obtained during the dedicated test. This phenomenon can be observed in figures 24–30. It may be hypothesized that the APU ran warmer in the dedicated experiment due to longer run times and a higher fuel line pressure. During the preliminary experiment fuel was delivered to the APU from a small 10 gal (37.8 l) fuel tank which is shown in figure 8. Because of the small capacity of this fuel tank, the APU had to be stopped approximately every forty minutes for refueling, allowing the APU to "cool off." Recall that during the dedicated APU experiment, fuel was delivered to the APU from a large fuel tank, 10,000 gal (37854 l), and fuel pumping station (see Section 2.4.12). Because the APU did not have to be shut off for refueling reasons during the dedicated experiment, the APU was left running for longer periods of time. It is hypothesized that the warmer exhaust temperatures and higher exhaust pressures that are observed in the dedicated experiment are a consequence of the longer run times.

3.7.3 Asymmetries Observed in the Axisymmetric Plume– In tracing the measured pressure values from the ambient air to the centerline of the exhaust plume, a monotone increasing line would be indicative of a symmetric flow. Likewise, data obtained on the x-axis should compare with data obtained on the y-axis if the APU exhaust plume were truly symmetric. Unfortunately, a hump in the pressure curve is observed in figures 24(a)–28(a). Likewise, an asymmetry is observed in figures 24(c)–28(c). This asymmetry is likely due to some error in the construction of the tube bank, a buildup of soot on a straightening screen, or a disturbance induced in the flow downstream of a welded seam. These asymmetries tend eventually to wash-out by four diameters downstream, as may be observed in figures 29–35.

3.7.4 Limitation of x-Axis Data to Six Diameters Downstream– Both x- and y-axis data are shown in figures 24–31, which show those graphs corresponding to the exit-plane data through data obtained at six diameters downstream of the exit. Beyond six diameters, that is from seven diameters downstream to ten diameters downstream, only y-axis traverses are presented. For the corresponding figures 32–35, the x-axis data were not measured due to a limitation on the freedom of movement of the small traverse in that direction.

3.8 Velocity Profile

The velocity at point n, u_n (ft/s), is given by

$$u_n = K_P \, C_P \left(\sqrt{\Delta p}\right)_{avg.} \sqrt{\frac{(T_n)_{avg.}}{P_n \, M_n}} \tag{3}$$

In equation 3, K_P is the Pitot tube constant given by

$$K_P = 85.29 \frac{ft}{s}\left[\frac{M}{R}\right]^{\frac{1}{2}} \tag{4}$$

C_P is the Pitot tube coefficient (dimensionless), Δp is the velocity head measured by the probe (in. H_2O), T_n is the temperature (°R), P_n is the pressure (mm Hg), which is computed by

$$P_n = P_{atm} + \Delta p \tag{5}$$

where P_{atm} is the atmospheric pressure, and M is the molecular weight of the gas (lb/lbmol).

By using equation 3 to compute the velocity, the temperature and pressure profiles presented in Section 3.7 can be converted to velocity profiles. Figures 36–41 show the velocity profiles from the exit plane to ten diameters downstream. The y-axis profiles were rotated about the centerline of the exhaust plume because, unlike the x-axis traverses, the y-axis traverses were taken at each survey plane from the nozzle exit to ten diameters downstream.

Figure 36(a) shows the velocity profile at the exit plane. Similarly figure 36(b) shows the velocity profile at one-half diameter downstream. Both figure 36(a) and figure 36(b) show steep profiles. The dip in the velocity profile at the centerline is a consequence of the pressure nonuniformity discussed in Section 3.7.3.

Figure 37(a) and figure 37(b) show velocity profiles for one and two diameters downstream, respectively. Figure 38(a) and figure 38(b) show similar profiles for three and four diameters downstream, respectively. Between figure 37(a) and figure 38(b), evidence that the exhaust plume is spreading as it progresses downstream is clearly visible.

As described in Section 3.7.3, the effect of the asymmetry begins to wash out beginning at four or five diameters downstream. Evidence of this occurrence is apparent in figures 38(b), 39(a), and 39(b), the figures corresponding to the velocity profiles at four, five, and six diameters downstream, respectively.

Figures 40 and 41 display the velocity profile at nine and ten diameters downstream, respectively. The peak velocity at ten diameters downstream is 250 ft/s (76.2 m/s). This velocity is slightly less than one-half of the peak velocity at the exit plane of 530 ft/s (161.5 m/s). This peak velocity, shown in figure 36(a), corresponds to a Mach number of 0.47.

3.9 Weather Data

As described in Section 2.3.13, the weather station at the OARF was used to gather data such as ambient temperature, atmospheric pressure, relative humidity, wind speed and wind direction. Tables B1 through B5, given in Appendix B, list these data for July 12, 1993, to July 16, 1993, respectively. The ambient weather conditions are listed for approximately every half-hour of the dedicated axisymmetric experiment. The time-averaged values of those parameters are computed and listed for each day.

The time-averaged ambient temperature over the five-day experiment varied between 57 and 58 °F (13.8 and 14.4 °C). In general, the temperature dropped through a testing session, reaching its lowest value at daybreak. The relative humidity varied between 80 and 95 percent, in general increasing through the night. The wind speed varied between 4 and 6 mi/hr (6.4 to 9.7 km/hr). The consistent ambient temperature, a stable relative humidity, and a low wind speed are desirable conditions for this type of outdoor experiment. Operating at night between 12 midnight and 8 a.m. allowed us to take advantage of these conditions.

3.10 Infrared Image Data

A large selection of infrared image data was recorded during the axisymmetric APU exhaust plume survey experiment. Appendix C includes a list of these data files. Each table in Appendix C lists the infrared data that were measured during a given night of the dedicated APU test. Over 130 data files were recorded over the duration of the experiment. The images include both MWB and LWB data. Data files include background images, images from different view points, and images measured with and without the nozzle shield. These data files were recorded using the 20-deg lenses. The infrared images that are presented and discussed in this section of the report represent only a small portion of the actual data that has been obtained. However, the data shown are representative of what is stored at NASA Ames Research Center on magnetic media. Those readers who have a need for an electronic version of these data may obtain them as well as the temperature and pressure data, by contacting the appropriate civil servant at NASA Ames, as discussed in Section 5.

3.10.1 Field Versus Frame– The Agema 880 Infrared Imaging System creates an infrared image by scanning a scene with a rotating-mirror and a fixed-mirror assembly embedded within the camera. The system is capable of a variety of scanning rates; however, only one scanner rate was employed for this experiment. Specifically, the scanners produced 6.25 images per second with 140×280 pixels per image. One image is referred to as one "frame" of data, where each "frame" is comprised of four interlaced "fields" of data. As shown in figure 42, one frame of data (140×280 pixels) is constructed by interlacing together four fields of data (140×70 pixels). The interlacing process creates the first four seventy-pixel rows of the frame, by using the first rows of the first, second, third, and fourth measured fields of data. The next four seventy-pixel rows of the frame are created by using the second row of the first, second, third, and fourth measured fields. This process is continued until the 140- $\times$ 280-pixel image is created.

3.10.2 Measurement of a Dynamic System– Because each field of data takes 0.04 s to obtain, the relatively short time span allows one the option of capturing the dynamic nature of a flow field such as the APU. Figure 43 shows three consecutively measured fields of filtered MWB infrared data. Each image of the APU exhaust plume shown in figure 43 looks slightly different. The difference between these images illustrates an important concept: while many precautions were taken to ensure that steady flow conditions were achieved, the APU exhaust plume is still a dynamic, or time-varying system.

3.10.3 MWB Infrared Data– The three infrared images shown in figure 44 are MWB data. Figure 44(a) is a MWB field of data. Figure 44(b) is a MWB frame of data that has been created by interlacing four images like the one shown in figure 44(a). The MWB image shown in figure 44(c) is the average of six frames of data. The horizontal zigzag lines, or cuts, visible on the outer fringes of the exhaust plume in figure 44(b) and figure 44(c) are a consequence of building the image by interlacing together several frames of data. An artifact of imaging a dynamic system with a scanning instrument, these horizontal lines tend to disappear as more fields of data are averaged together; see Section 3.10.6. Comparing figure 44(b) with figure 44(c), these horizontal lines are seen to nearly disappear.

3.10.4 Filtered MWB Image Data– The infrared images in figure 45 are filtered MWB data. Figure 45(a) shows one field of data, figure 45(b) shows one frame of data, and figure 45(c) shows an image averaged over six frames

of data. The color scale shown at the bottom of the figure applies to all three images. Recall that the filtered response of the MWB camera is shown in figure 18(b).

One goal of this report is to provide a data base for validating Turk's (ref. 25) infrared image prediction algorithm described in Section 1.2. The filtered MWB image shown in figure 45(c) represents an image ideal for this purpose. In figure 45(c) the backdrop is uniform, the spread angle is visible (see Section 3.10.8), and the probe has been positioned outside of the exhaust stream. An intensity scale has been added to this image. This image is compared in Section 4 to an infrared image predicted using Turk's algorithm.

3.10.5 LWB Image Data– Figure 46 shows LWB images of the APU exhaust plume. Figure 46(a) shows one field of data, figure 46(b) shows one frame of data, and figure 46(c) shows an infrared image averaged over six frames of data. The wavy streak visible at the top right-hand corner of each of these three images is the edge of the aluminized-Mylar backdrop. The edge is visible in these LWB images because the cameras were positioned to get the best possible plume and backdrop alignment for the MWB camera. Consequently, the LWB image shows some of the backdrop. Despite the appearance of the backdrop on the edge of the LWB images, the backdrop is located directly behind the APU plume. The color scale shown at the bottom of figure 46 applies to each of these three images.

3.10.6 Advantages of Time-Averaging– Figure 47 shows two MWB infrared images, each averaged using five hundred frames of data. This represents an average of data over eighty seconds in time. The horizontal cuts described in the preceding sections are less apparent in these images, making the plume appear smooth with less dynamic fluctuations. The combination temperature and pressure probe is visible as a bright point source in figure 47(a). The probe is obviously being heated by the flow. Visible above the probe is another "hot spot." This second "hot spot" is a reflection coming from the underside of the unrolled aluminized Mylar tube.

An additional point of interest about figure 47(a) concerns the white, or hot, area near the nozzle exit. For most of the infrared images obtained during the APU experiment, a foreground shield, or reflective barrier, was placed between the APU nozzle and the camera. Figure 47(b) shows a MWB infrared image where the foreground shield has been used to obscure the APU nozzle. Hot parts such as metal nozzles tend to radiate with a much larger intensity than do exhaust plumes. For this reason a shield is placed between the nozzle and the camera to prevent the additional energy from the nozzle from reaching the detector of the camera and potentially saturating the image. This has clearly occurred in figure 47(a). With the exception of figure 47(a), which is presented for illustration only, each of the infrared images presented in this section were taken with the foreground shield in place.

3.10.7 Infrared Image of the Backdrop– The aluminized Mylar backdrop, as discussed in Section 2.3.15, provides a uniform, relatively cold, and substantially large area for imaging of the APU exhaust plume. Figure 48(a) shows a MWB infrared image of the backdrop where the nozzle foreground shield is visible at the lower portion of the image. Figure 48(b) shows a LWB infrared image of the aluminized Mylar backdrop. Visible on either side of the backdrop is the horizon. The difference between the relatively uniform radiance (reflected) of the backdrop and the relatively non-uniform radiance of the horizon dramatically illustrates the advantages of using a backdrop. The average apparent temperature of the backdrop shown in figure 48(a) is 57 °F (13.9 °C) with a standard deviation of 5 °F. The corresponding apparent temperature of the backdrop in the LWB is –7 °F (–21.7 °C) with a standard deviation of 2 °F. Each of these calculations were computed using approximately twenty-six thousand pixels. The apparent temperature is lower in the LWB than in the MWB because the LWB radiation comes from higher in the atmosphere due to less absorption in that band by atmospheric gases.

Because the aluminized-Mylar backdrop works by reflection, clouds and airplanes that pass above the test scene can affect uniformity and apparent temperature. For example, an overhead cloud can cause the apparent temperature to fluctuate as much as 30 °F. For this reason the backdrop worked best on cold and cloudless nights.

3.10.8 Plume Spread Angle– The infrared images shown in figures 44–48 illustrate the plume spreading angle. Hossain and Rodi (ref. 55), Chen and Rodi (ref. 56), and Bejan (ref. 57) predict spread angles between 7.5 deg and 9 deg for turbulent, buoyant, vertical jets. The spread angle of this jet is approximately 7 deg from vertical. This result is consistent with Hardman's observations (ref. 20).

3.11 Validity of the Measured Infrared Image Data

The infrared images presented in this report are accurate only to within the limits of the Agema 880 Dual Band scanning infrared camera system. The MWB camera is quoted by Agema as having a source sensitivity of 0.1 °C at 30.0 °C. The LWB camera has a source sensitivity of 0.05 °C at 30.0 °C. The scanners have an accuracy of ±2 percent. Keep in mind that these data are quoted for a new camera system and that detector elements can

degrade with use. The Agema system used in the APU experiment was recalibrated by the Agema company just prior to the dedicated APU exhaust plume survey.

Proper use and storage of delicate instruments such as the Agema system is fundamental to good maintenance. For this reason, the cameras are stored in a temperature-controlled office in their original cases when not in use. When being used during an experiment, these instruments are handled with the utmost of care. Of particular importance is keeping the detectors cooled with liquid nitrogen. Before the cameras are turned on, the dewars are filled and the detectors are allowed adequate time to reach operating conditions. The dewars are continually topped-off with liquid nitrogen so that their response is stable.

When the Agema system was purchased by NASA Ames in 1990, it represented the state-of-the-art in infrared imaging technology. During the time of this experiment, the state-of-the-art has seen the introduction of staring Focal Plane Array (FPA) systems. An FPA system typically incorporates an array of detectors as opposed to one single detector element (ref. 58). For this reason FPA systems provide image quality that far surpasses that of older-generation scanning systems. However, FPA systems currently suffer from calibration problems due to the large number of detector elements (ref. 59).

The measurement accuracy of the Agema 880 infrared imaging system is maintained by constantly monitoring internal temperature sensors that compensate for detector response by adjusting the gain of the system after each scanning sequence. By "recalibrating" the detector at the end of each scan line, the older generation Agema 880 system offers accuracy and predictability that cannot be attained by current generation FPA systems. Because the Agema 880 system offers this advantage over FPA systems, and because of its immediate accessibility to our testing crew, it was the logical choice for instrumentation.

3.12 Uncertainty of Measured Infrared Images

As mentioned in Section 3.11, the Agema 880 Dual Band scanning infrared camera system has a source sensitivity of 0.1 °C at 30.0 °C for the MWB camera. The LWB camera has a source sensitivity of 0.05 °C at 30.0 °C. This uncertainty in the source sensitivity can produce errors in the measured radiance. Figure 49 shows how three color legends can be attached to the same measured infrared image by virtue of the instrument uncertainty. The three color legends show the minimum radiance due to uncertainty, the measured radiance, and the maximum radiance due to uncertainty, respectively. The scale for the minimum radiance is obtained by subtracting from the measured radiance the instrument uncertainty, and linearly scaling the color legend. The scale for the maximum radiance is similarly obtained by adding the instrument uncertainty to the measured radiance. In this example, the difference between the minimum and maximum measured radiance due to instrument uncertainty varies less than 0.27 percent.

3.13 Midac Spectrometer Data

One goal of the APU experiment was to gain a quantitative understanding of the levels of carbon dioxide, water vapor, and carbon monoxide in the APU exhaust plume. Charles Bennett of Lawrence Livermore National Laboratory (LLNL), in Livermore, California, offered to investigate with us the feasibility of using an infrared spectrometer for this purpose. Before the preliminary experiment we were hopeful that Bennett's technique of using the measured spectra to predict exhaust plume constituent levels would work. Unfortunately, this technology is not yet sufficiently mature, and so the focus of Bennett's post-processing analysis shifted to using the APU spectra to predict a pre-measured temperature within the exhaust plume.

Bennett visited both the preliminary experiment in May 1993 and the dedicated experiment on July 13, 1993, and took several hours of data with the Midac spectrometer, as described in Section 2.3.16. Post-experiment analysis of the spectrometer data yielded results that were unsuccessful in predicting the exhaust plume constituent distributions. The inability to resolve carbon dioxide and water vapor levels from the measured spectra is attributed to the fact that the spectra of these two species overlap significantly in the MWB. Because the spectra are inseparable in the MWB, it may be impossible to predict the levels of carbon dioxide and water vapor in the plume.

Because carbon monoxide emits in a region of the MWB that does not overlap with the spectra of water vapor and carbon dioxide, the focus of Bennett's post-processing efforts changed. It was now the goal of his research to use the carbon monoxide spectra to predict the temperature of a particular point in the APU exhaust plume. By matching the measured spectrum with the spectrum corresponding to a known temperature, the temperature of the source could be determined. The digitally controlled traverse rig was used to position the probe along the line-of-sight connecting the spectrometer with the light source. The temperature and pressure at that point were then measured by the probe. Each spectrometer survey was conducted at one diameter downstream of the nozzle exit.

Predicting the temperature of the exhaust plume using the measured spectra is complicated by virtue of looking through a column of gas through which there exists a

steep temperature gradient. In this scenario, the spectrometer looks through the relatively cold ambient air, into the hot exhaust plume, back into the relatively cold ambient air, and finally into a light source having a known spectrum. An added benefit of conducting the surveys near the nozzle exit, one diameter downstream, is that the temperature profile in the exhaust plume at these locations is fairly flat so that the measured temperature would approximate the average temperature of the exhaust plume along the line-of-sight between the light source and the spectrometer.

The process of predicting a temperature by matching the measured spectrum with a spectrum from a source of known temperature is illustrated in figure 50. Here the solid symbols represent the measured data and the open symbols represent the spectrum of carbon monoxide at some temperature. In figure 50, the spectrum corresponding to a known temperature approximates the measured data; when the two spectra match, the temperature of the emitting constituent is hypothesized to be that of the theoretical spectrum. The results from this analysis are summarized in table 5. As can be seen from the results given in table 5, the temperature determined in this way is within ten to twenty percent of the measured temperature.

4. Infrared Image Prediction

Recall that this work is partially motivated by the need to validate computational fluid dynamic (CFD) codes. Also recall that the validation technique requires a quantitative comparison between an experimental infrared image and an infrared image predicted from a CFD solution. The latter image incorporates the use of an inverse Monte Carlo ray-trace technique. This section describes the ray-tracing technique. Infrared images predicted from the data obtained during the axisymmetric auxiliary power unit (APU) experiment are also shown.

It is the intent of this report to provide to the scientific community a meticulously obtained and completely documented data base for infrared analysis of sub-sonic jet engine exhaust plumes. One motivation for creating the data base is to validate Turk's (ref. 25) infrared image prediction algorithm. Improvements are still being incorporated into Turk's computer program, and so this report describes the current state of a work-in-progress. Turk's doctoral dissertation describes the development of the Monte Carlo ray-trace technique. Specifically, his contribution focuses on methods for accelerating the ray-trace process. The reader is referred to Turk's dissertation for a more detailed description of the Monte Carlo ray-trace method (ref. 25).

4.1 History

A virtual panacea of techniques is available for infrared image prediction of exhaust plumes. In general this technology has been developed for use by the defense community. As a consequence of limited availability due to security concerns, no single scientist or engineer is likely to have seen all of the methods that have evolved for predicting infrared images. However, over the past four years the scientific community has witnessed a dramatic improvement in the ability to predict infrared images that approach measured data. By comparing General Electric's infrared image prediction program, LOIR (ref. 33), which was supposedly the state-of-the-art in 1990, to the images that can now be predicted using Turk's inverse Monte Carlo ray-trace computer program, it is obvious that a significant contribution has been made to this field. It is now possible to attach a similar radiative flux scale to both the predicted and the measured infrared images, a capability nearly unimaginable only four years ago with LOIR. It should be mentioned that many improvements to LOIR have been made since 1990 and that the current version General Electric's infrared analysis code is now called LOIR II (ref. 60).

4.2 How the Ray-Trace Method Works

The reverse Monte Carlo ray-trace computer program has been coded to predict the infrared image that would be captured by an infrared camera. The word "reverse," or "inverse," is attached to the name because the rays are not traced forward from the scene to the infrared camera as the phenomenon actually occurs. Rather, the rays are traced in reverse from the camera to the scene. By tracing the rays from the observer to the scene in the reverse manner, only that radiation leaving the scene and arriving at the infrared camera need be modeled. Accounting for only this radiation significantly reduces the work required to solve the problem. As they are described in Section 4.3, the problem can be solved in the reverse fashion because of the reciprocity relationships which govern the radiative exchange of energy between surfaces and volumes.

In order to develop a two-dimensional infrared image from a three-dimensional CFD or CFD-like solution, several rays are traced from the camera detector element, through a pixelized virtual screen, and finally into the object space or the solution domain. Figure 51 illustrates this methodology. The quality of the predicted image improves by increasing the number of pixels on the virtual screen and by increasing the number of rays used per pixel, within the resolution of the CFD solution itself. The predicted infrared image has converged when the object space has been adequately sampled such that an

increase in the number of rays does not improve the quality of the predicted image.

When a ray leaves the detector element of the camera and traverses a pixel on the virtual screen, its direction is selected at random as shown in figure 52. Two random numbers are generated which define a point on the detector element. Next, two additional random numbers are generated which define a point within a given pixel located on the virtual screen. The orientation of the outgoing ray is defined along a line connecting the point on the detector element with the point within the pixel. Note that in this scenario both the detector and the pixel have finite areas.

Once the ray leaves the infrared camera and pixelized virtual screen, it enters the CFD solution space. Here the ray encounters a cell, where a cell is a region of the CFD solution domain that is bounded by eight nodes. The ray can either be absorbed in that cell, be transmitted through it, or be scattered. Figure 53 illustrates all possible outcomes for a ray that enters a CFD solution domain. If the ray encounters a solid surface it can be absorbed by that surface or reflected from it. If the ray is transmitted through a cell, it continues to traverse the CFD solution domain until it is absorbed in another cell or until it exits the solution domain. The termination point of the ray determines the radiative contribution of that ray to a pixel on the virtual screen.

When a ray enters a cell of the CFD solution several decisions must be made to determine if the ray is absorbed in that cell. To begin with, the eight bounding nodes of the cell are used to define the six surfaces which describe that cell, as shown in figure 54. The ray's entrance point on one surface of the cell and its direction are used to compute its exit point. When the exit point has been defined, the ray's path length, s, through the cell can be computed by

$$s = \sqrt{\left(x_i - x_j\right)^2 + \left(y_i - y_j\right)^2 + \left(z_i - z_j\right)^2} \qquad (6)$$

where x, y, and z represent Cartesian coordinates, and the subscripts i and j distinguish between the entrance and exit points, respectively, as shown in figure 54.

Next, the average temperature, average pressure, and average species concentration of the cell are computed using Shepard's interpolation scheme, which is described in reference 61. Here, the average parameters are computed at the centroid of the cell by using the parameter values at the cell's eight bounding nodes. The distance between the cell centroid and each bounding node is used to weight that node's contribution to the final average.

The average value, $S(P_i)$, of the temperature, pressure or species concentration at the cell centroid, P_i, where P_i is defined by (x_i,y_i,z_i), is given by

$$S(P_i) = \frac{\sum_{j=1}^{N=8} \frac{S_j}{\left\|P_i - P_j\right\|}}{\sum_{j=1}^{N=8} \frac{1}{\left\|P_i - P_j\right\|}} \qquad (7)$$

where the summation occurs over the eight nodes, denoted by the subscript j, that define the cell, and the magnitude of the distance between the cell centroid P_i, and some point P_j, where P_j is defined by (x_j,y_j,z_j) is given by

$$\left\|P_i - P_j\right\| = \sqrt{\left(x_i - x_j\right)^2 + \left(y_i - y_j\right)^2 + \left(z_i - z_j\right)^2} \qquad (8)$$

or

$$\left\|P_i - P_j\right\| = s \qquad (9)$$

which follows from equation 6.

Once the average temperature, average pressure, species concentration, and path length have been defined for a cell, the absorptivity, α, of that cell can be computed using an infrared band model. The infrared band model used to compute $\alpha_\lambda(\lambda)$ is described in Nelson's Master of Science thesis (ref. 22). The character λ, in parentheses, denotes the wavelength dependence of this computation. All the equations necessary to make this computation are given in reference 22.

Next, a random number is generated and compared with the absorptivity of the cell to determine if the ray is absorbed in that cell or if the ray is transmitted through the cell. If the random number is less than or equal to the absorptivity, i.e.,

$$random\ number \le \alpha_\lambda(\lambda) \qquad (10)$$

then the ray is absorbed in that cell. If the random number is greater than the absorptivity, i.e.,

$$random\ number > \alpha_\lambda(\lambda) \qquad (11)$$

then the ray is transmitted through the cell. The sequence of events described above is followed until the ray is absorbed in a cell, or until the ray exits the solution domain. Upon exiting the solution domain, the ray can be absorbed by an infinite extension of the ambient atmosphere, a background simulation, or a blackbody at a temperature of absolute zero, for example.

4.3 Energy Computation

The ray tracing technique is useful in computing the radiative flux or energy arriving at the observer location from the scene. This computation is more easily described after first presenting the reciprocity relationships for radiative exchange between surfaces and volumes. The equation used to compute the energy arriving at the observer location can then be more easily understood. The reciprocity relationships are developed here because in this analysis radiation is emitted from surface and volume elements (cells), and absorbed by a surface element (the detector element).

The reciprocity relationship, in the absence of a change in the index of refraction, for a radiative exchange between surface i and surface j given by

$$D_{S_i\,S_j}\;\varepsilon_{\lambda,S_i}\left(\lambda,T_{S_i}\right)A_{S_i}=D_{S_j\,S_i}\;\varepsilon_{\lambda,S_j}\left(\lambda,T_{S_j}\right)A_{S_j} \quad (12)$$

In equation 12, D is the distribution factor, ε is the hemispherical emissivity, and A is the area of the surface. The subscript λ, denotes spectral dependence, and the subscript S identifies the variable as a surface property. The independent variables λ and T denote wavelength and temperature dependence, respectively. The distribution factor, $D_{Si\,Sj}$, is the fraction of rays emitted by surface i that are absorbed by surface j due to direct radiation and all possible reflections, refractions, and scattering events. The distribution factor for the radiative exchange between surface i and surface j is estimated by

$$D_{S_i\,S_j}=\frac{N_{S_i\,S_j}}{N_{S_i}} \quad (13)$$

where $N_{Si\,Sj}$ is the number of rays emitted by surface i and absorbed by surface j, and N_{Si} is the total number of rays emitted by surface i. The distribution factor is also equal to the ratio of energy emitted by surface i and absorbed by surface j to the total energy emitted by surface i, that is,

$$D_{S_i\,S_j}=\frac{E_{S_i\,S_j}}{E_{S_i}} \quad (14)$$

A similar reciprocity relationship can be written for a surface-to-volume energy exchange,

$$D_{S_i,V_j}\;\varepsilon_\lambda\left(\lambda,T_{S_i}\right)A_{S_i} = 4\,D_{V_j,S_i}\int_{A_{proj.\,V_j}}\varepsilon_\lambda\left(\lambda,C_{V_j},T_{V_j},P_{V_j},s_{V_j}\left(A^*\right)\right)dA^* \quad (15)$$

and a volume-to-volume energy exchange,

$$D_{V_i,V_j}\int_{A_{proj.\,V_i}}\varepsilon_\lambda\left(\lambda,C_{V_i},T_{V_i},P_{V_i},s_{V_i}\left(A^*\right)\right)dA^* = D_{V_j,V_i}\int_{A_{proj.\,V_j}}\varepsilon_\lambda\left(\lambda,C_{V_j},T_{V_j},P_{V_j},s_{V_j}\left(A^*\right)\right)dA^* \quad (16)$$

In equations 15 and 16, C is the concentration of species, P is the pressure, and s is the path length of the volume. A^* is the projected area of the volume.

In this development, the spectral emittance, ε is related to the absorption coefficient, α, by

$$\varepsilon_\lambda(\lambda,C,T,P,s)=1.0-e^{-\int_0^s\alpha_\lambda\left(\lambda,C\left(s^*\right),T\left(s^*\right),P\left(s^*\right)\right)ds^*} \quad (17)$$

The absorption coefficient, α, is computed by an infrared band model.

By invoking the reciprocity relationships given in equations 12–16, the energy arriving at the observer location, o, from all surfaces and volumes is given by

$$dE_o(\lambda)=\sum_{i=1}^{N_s}D_{oi}\frac{\varepsilon_\lambda(\lambda,T_o)A_o}{\varepsilon_\lambda(\lambda,T_i)A_i}\pi\varepsilon_\lambda(\lambda,T_i)i'_{\lambda b}(\lambda,T_i)A_i d\lambda + \sum_{j=1}^{N_V}D_{oj}\frac{\varepsilon_\lambda(\lambda,T_o)A_o}{4\int_{A_j}\varepsilon_\lambda\left(\lambda,C_j,T_j,P_j,s_j\left(A^*\right)\right)dA^*} \times 4\pi i'_{\lambda b}\left(\lambda,T_j\right)\int_{A_j}\varepsilon_\lambda(....)dA^*\,d\lambda \quad (18)$$

where $i'_{b,\lambda}(T)$ is the Plank blackbody radiation distribution function. Equation 18 may be rewritten after canceling and collecting terms to give the energy arriving at the observer location as

$$dE_o(\lambda)=\sum_{k=1}^{N_{all}}\pi\,D_{ok}\,\varepsilon_\lambda(\lambda,T_o)i'_\lambda\left(\lambda,T_k\right)A_o\,d\lambda \quad (19)$$

4.4 Line-of-Sight Method

One disadvantage of the Monte Carlo technique is the time required to obtain broad-band high quality images. Because the ray-trace must be conducted over small wavelength intervals, $\Delta\lambda$, broad-band images are time

consuming to obtain. A broad-band image is obtained by integrating across the wavelength band; the broader the wavelength band, the longer it takes to predict an infrared image.

The Line-of-Sight (LOS) method for predicting infrared images is faster than the Monte Carlo technique because fewer rays are required to sample the solution domain. The LOS method is like the Monte Carlo technique in that it utilizes a graphical ray-trace method. The sequence of tracing rays begins by generating a random initial direction for the ray as described in Section 4.2. When a ray leaves the pixelized screen and enters a cell, the path length through the cell is computed and the eight bounding nodes are used to compute the average temperature, pressure, and species concentration of the cell. An infrared band model is then invoked to compute the transmissivity, $\tau_{\Delta\lambda}$, of the cell. The transmissivity of the ray is the product of the transmissivity of each cell traversed by the ray

$$\tau_{\Delta\lambda,ray} = \prod_{i=0}^{J} \tau_{\Delta\lambda,i} \tag{20}$$

The ray continues to the next cell if the transmissivity of the ray is greater than some small value, say 0.001; i.e.,

$$\tau_{\Delta\lambda,ray} > 0.001 \tag{21}$$

In the LOS method, the ray continues to be traced through the solution domain until the total transmissivity of the ray is less than some small value, say 0.001; i.e.,

$$\tau_{\Delta\lambda,ray} \leq 0.001 \tag{22}$$

The energy contributed by the ray to the computed infrared image is given by

$$dE_{ray,o}(\lambda) = \sum_{i=1}^{n} \tau_{\lambda,i-1}\, \varepsilon_{\lambda,b}\, i'_{\lambda,i}(\lambda, T_i)\, A_o \cos\Theta\, d\lambda\, d\omega_{ray} \tag{23}$$

where the sum is over the number of cells traversed by the ray, the emissivity and the ray transmissivity is defined in equation 21. In equation 23 the differential solid angle subtended by the ray can be written

$$d\omega_{ray} = \frac{1}{N} \frac{dA_{pixel}}{r^2} \tag{24}$$

In equation 24, dA is the projected differential area of a pixel to the observer, N is the total number of rays traced, and r is the distance between the observer and the pixel on the virtual screen.

It is important to note that in the LOS method the contribution of each cell encountered by the ray is included in the equation used to compute the energy arriving at the observer location. The Monte Carlo technique is different from the LOS method in that only the contribution of the terminating cell is included in the Monte Carlo analysis, as indicated in equation 19. Because the contribution of each cell is included in the LOS analysis, fewer rays are required to adequately sample the solution domain. Consequently, the LOS method requires fewer rays to achieve convergence.

4.5 Increasing the Number of Rays Per Pixel Improves the Quality of the Predicted Images

The ultimate goal of the reduction of the three-dimensional CFD solution domain to a two-dimensional infrared image is a pixel-by-pixel comparison of the predicted image with measured experimental results. Such a comparison would not only serve as a validation technique for the CFD solution, but would also suggest, although not prove, that the solution domain was adequately sampled by the ray-trace method. It is intuitive that increasing the number of rays used to sample the solution domain would increase the probability of achieving a converged and accurate image, within the limits of the CFD solution. However, due to the long run times required to achieve such a solution the majority of the images presented in this section are less-than-converged solutions.

Figure 55 shows a comparison of three predicted infrared images. Each of the images is predicted using the LOS method and is computed across the 4.1 μm to 4.8 μm wavelength interval. The appropriate system response function, shown in figure 18(b), has been incorporated in the analysis. Each of the images has 50 × 100 pixels and the same arbitrary color scale. The difference between these images is the number of rays per pixel used in their generation. Figure 55(a) took two rays per pixel to create. Figure 55(b) and figure 55(c) took twenty and forty rays per pixel to create, respectively. The visually apparent difference between figure 55(a) and figure 55(b) is greater than the rather subtle visual difference between figure 55(b) and figure 55(c). The images appear smoother as the number of rays per pixel increases because the variability of the current pixel value from the converged pixel value decreases. These three images illustrate that the quality of the predicted image improves as the number of rays per pixel increases.

The image shown in figure 55(a) took approximately two hours of CPU time to create using a Cray C-90 with 128 megawords of main memory. The computation was completed on one of the eight processors, where each

processor has a peak operational speed of one gigaflop. The image shown in figure 55(b) is the result of averaging together ten images like the one shown in figure 55(a). Similarly to create the image shown in figure 55(c), twenty images like figure 55(a) were averaged together.

4.6 Effect of Exhaust Plume Constituents on the Predicted Infrared Image

As mentioned in Section 3.11 the attempts to measure the exhaust plume constituents with the Midac spectrometer were unsuccessful. In an effort to use reasonable values for the exhaust plume constituents, concentrations for water vapor, carbon dioxide and carbon monoxide were extracted from reference 62. The concentration of water vapor at the core was assumed to be 0.03 percent by volume. The concentration of carbon dioxide at the core was assume to be 0.031 percent by volume. Finally, the concentration for carbon monoxide was assumed to be 0.0 percent. These values are likely to be inaccurate to a certain degree. However, the predicted infrared images that are shown in subsequent figures show acceptable agreement with the experimental data. While we know that the concentrations of these constituents are inaccurate to some extent, we think their values are at least close to the actual values based on the agreement between the predicted and measured data.

4.6.1 Species Concentration Mapped to Total Temperatures– The core species concentrations, mentioned above, were mapped throughout the exhaust plume and into the surrounding atmosphere using Crocco's similarity relationship (ref. 63). The analogy maps the spread of the core concentrations according to the total temperature. The concentration of a species at a point, C_{pt}, is given by

$$C_{pt} = \frac{C_{core} - C_{amb}}{T_{o_{core}} - T_{o_{amb}}} \left(T_{o_{pt}} - T_{o_{amb}} \right) + C_{amb} \quad (25)$$

where the subscript *amb* is an abbreviation for *ambient* and denotes ambient conditions, and the subscript *o* denotes a total value, i.e., total temperature. An assumption that the turbulent Lewis number of the exhaust plume is equal to one limits the applicability of equation 25.

4.6.2 Carbon Dioxide Variance and Its effect on the Predicted Infrared Image– Figure 56 shows four infrared images that were predicted using the LOS method. Each of the three infrared images have 50 × 100 pixels and were predicted at 4.175 μm (2395 cm^{-1}). The wavelength was selected in a region of the spectrum where carbon dioxide is the predominant emitter. Figure 56(a) shows an infrared image predicted using the baseline constituents described above. Figure 56(b), figure 56(c), and figure 56(d) show images where the concentrations of water vapor and carbon dioxide in the core have been increased by ten, twenty, and thirty percent, respectively. Each of these images are shown with the same arbitrary color scale. The intensities of the predicted infrared images increase as the concentrations of water vapor and carbon dioxide increase. However, the visual difference between the baseline image, figure 56(a), and the image where the concentrations of carbon dioxide and water vapor were increased by thirty percent, figure 56(d), is barely perceptible.

Because images can often be misleading, it is useful to look at a plot of intensity change versus change in carbon dioxide concentration. Figure 57 shows a plot that compares the change of baseline peak intensity as the baseline level of carbon dioxide is varied. This plot illustrates nicely the effect on the predicted infrared image obtained by varying the level of carbon dioxide in the core of the exhaust. The baseline intensity was computed for an observer looking at the core of the exhaust at 4.175 μm (2395 cm^{-1}) using the LOS method.

4.7 The LOS Image Compared to Filtered Experimental Data

Figure 58 shows a comparison of a measured filtered infrared image with an infrared image predicted using the LOS method. The measured infrared image has been optically filtered to include data only within the 4.1 to 4.8 μm wavelength interval. The predicted infrared image is computed across the same interval, where the infrared band model has been invoked to provide a 5 cm^{-1} resolution across the interval. A similar color scale has been used on both images so that a direct comparison between the two images can be made.

The primary difference between the experimental image, shown in figure 58(a), and the predicted image, shown in figure 58(b), can be seen downstream of the nozzle exit. Here, the predicted infrared image is cooler than the experimental infrared image. The most likely explanation for this discrepancy is an improper accounting for the exhaust plume species concentrations in the core. Also, by mapping the concentrations according to the total temperature, an additional degree of uncertainty has been added to the computation. Even though these images appear slightly different downstream of the nozzle exit, the favorable comparison between these two images represents the current state-of-the-art in infrared image prediction technology.

4.8 Monte Carlo Ray-Trace Image Compared to Experimental Data

Figure 59 shows a comparison between an infrared image predicted using the Monte Carlo ray-trace method and an experimental filtered-MWB infrared image. Figure 59(a) shows an infrared image predicted at 4.175 μm (2395 cm^{-1}). The predicted image has 25 × 50 pixels and five thousand rays were traced per pixel. The predicted image took approximately seven days to run on a Silicon Graphics Indigo (SGI) 2 Extreme® Computer that utilizes a 150 MHz IP2 processor and sixty-four megabytes of main memory (ref. 64). The experimental infrared image shown in figure 59(b) is a filtered-MWB image that has 140 × 70 pixels and represents one field of data.

At first glance the predicted and measured images shown in figure 59 look quite dissimilar. However, the predicted image shown in figure 59(a) is not a converged image. If the Monte Carlo ray-trace code had been run sufficiently long to predict a converged solution the image would resemble the image predicted by the LOS analysis shown in figure 58. To this date a converged solution has not been obtained by the Monte Carlo code using this data set due to the excessive CPU time required for such an analysis.

5. Conclusion and Recommendations

The goal of the body of work presented in this report is to provide to the user community a data base for infrared analysis of jet engine exhaust plumes. To meet this goal, the temperature and pressure profiles of an APU exhaust plume were surveyed. Corresponding MWB, filtered-MWB and LWB infrared images were obtained. These data have been published in a variety of conferences (refs. 23 and 24), as well as this NASA TM. Information on how users may obtain electronic versions of these data are given in this section.

5.1 The Goal

Infrared imaging has been shown to be a valuable tool for heated flow field visualization. The ability of an infrared imaging system to resolve both large- and small-scale flow structures makes it a useful tool for validating CFD codes. The validation technique consists of the direct comparison between experimentally obtained infrared images and images predicted from the CFD solution. Predicting infrared images from CFD solutions requires reducing the three-dimensional CFD solution to a two-dimensional infrared image. A reverse Monte Carlo algorithm has been developed to accomplish this. The data base described in the preceding sections has served to help validate this algorithm.

The temperature and pressure profiles obtained from the APU experiment were assembled into a CFD-like solution. The reverse Monte Carlo computer program was utilized to predict an infrared image using the CFD-like solution as input. The predicted infrared images were compared with experimental data in Section 4. The favorable comparison between the two images lends credibility to the computer program.

5.2 The Experiment

The APU experiment described in Section 2 was successful in meeting the goals discussed out in Section 5.1. Temperature and pressure surveys of the APU exhaust plume were made from the exit plane to ten diameters downstream. Much effort went into ensuring the accuracy and repeatability of the data. This effort included calibration of instrumentation, a thorough check out of the data acquisition system during the preliminary experiment, and duplicate temperature and pressure surveys.

The work presented in this report is unique and different from other temperature and pressure surveys of exhaust plumes in that a corresponding set of MWB, MWB-filtered, and LWB infrared data were obtained. An aluminized Mylar backdrop was utilized to create a relatively cold and uniform backdrop for the infrared data. The scanning infrared cameras were recalibrated prior to the APU experiment. The infrared cameras were treated with the utmost care during the experiment to ensure the integrity and repeatability of their response. The result of these efforts is a data base of infrared images that complement the temperature and pressure data base.

5.3 Publication of Results

Different portions of the research presented in this report have been published in a variety of locations. Nelson's Master of Science thesis describes the selection of an infrared band model for predicting infrared images (ref. 22). The work described in that thesis was presented at an SPIE conference by the author (ref. 23). Birckelbaw and Nelson show in an AIAA paper the utility of a scanning infrared imaging system to resolve the flow field about several V/STOL aircraft (ref. 19). A subsequent SPIE conference paper (ref. 24) and a paper given recently at a JANNAF conference at Lockheed Missiles and Space Company (ref. 60) describe the body of work shown in this report. The publication of this research in a

variety of forums and at different conferences subjects the work to a review by professionals that are familiar with this technology. The data described here have been well received by the infrared analysis community.

5.4 Public Access to Data

This report, originally published as a doctoral dissertation, is currently being published as a NASA Technical Memorandum (NASA TM) (ref. 65) to make its access more readily available to the public. Also, data collected during the rectangular nozzle survey (not presented here) will subsequently be published as a NASA TM (ref. 66). Electronic versions of the temperature, pressure, and infrared data may be obtained by contacting:

Larry D. Birckelbaw
Mail Stop 327-7
NASA Ames Research Center
Moffett Field, CA 94035-1000

5.5 Recommendations for Future Work

The most important contribution that could be made to the body of work presented in this report would be to accurately measure the exhaust plume constituents issuing from the APU nozzle. Currently the levels of the exhaust plume constituents are estimated and the proximity to the actual values is hypothesized to be close enough when the predicted infrared images compare favorably to measured results. Quantitatively measuring the APU exhaust plume constituents would be an important contribution to this data base.

Finally, as discussed in Section 3.11, the Agema 880 Dual Band scanning infrared camera system was a state-of-the-art infrared imaging system in 1990. If an experiment similar to this one were to be conducted in the future, a more modern imaging system would likely yield higher-grade data than that which could be attained with the Agema 880 system. For this reason, it is recommended that for future tests, other options for infrared imaging such as focal plane array systems be investigated.

Appendix A

Temperature and Pressure Data

Table A1. Y-axis pressure data measured at the exit plane; see figure 24(a)

run 1		run 2		prelim. run 1		prelim. run 2	
y-axis position (in.)	pressure (psig)	y-axis position (in.)	pressure (psig)	y-axis position (in.)	pressure (psig)	y-axis position (in.)	pressure (psig)
-3.27	0.014	-4.66	0.006	-4.75	0.028	-4.75	0.000
-2.80	0.015	-4.50	0.008	-4.50	0.025	-4.50	0.000
-2.72	0.014	-4.41	0.008	-4.25	0.000	-4.25	0.000
-2.56	0.014	-4.25	0.008	-3.75	0.002	-3.75	0.000
-2.33	0.662	-3.91	0.008	-3.25	0.002	-3.25	0.000
-2.09	0.802	-3.75	0.007	-2.75	0.000	-2.75	0.000
-2.02	0.844	-3.42	0.006	-2.55	0.004	-2.55	0.000
-1.94	0.899	-3.27	0.008	-2.45	0.000	-2.45	0.000
-1.86	0.949	-3.11	0.007	-2.35	0.000	-2.35	0.000
-1.78	0.999	-2.95	0.007	-2.25	0.084	-2.25	0.283
-1.70	1.030	-2.80	0.007	-2.15	0.596	-2.15	0.604
-1.55	1.057	-2.64	0.007	-2.05	0.697	-2.05	0.676
-1.39	1.039	-2.48	0.008	-1.95	0.773	-1.95	0.763
-1.23	1.020	-2.33	0.565	-1.75	0.926	-1.75	0.909
-1.08	1.005	-2.17	0.698	-1.25	0.978	-1.25	0.956
-0.84	0.980	-2.02	0.776	-0.75	0.958	-0.75	0.924
-0.69	0.972	-1.86	0.903	-0.25	0.941	-0.25	0.909
-0.53	0.978	-1.70	1.015			0.00	0.923
-0.41	0.966	-1.55	1.044			0.25	0.922
-0.25	0.942	-1.39	1.036				
-0.09	0.954	-1.23	1.028				
0.00	0.964	-1.08	1.018				
0.16	0.971	-0.84	0.999				
		-0.69	0.981				
		-0.41	0.995				
		-0.25	0.978				
		-0.09	0.968				
		0.00	0.977				
		0.16	0.997				

Table A2. Y-axis temperature data measured at the exit plane; see figure 24(b)

run 1		run 2		prelim. run 1		prelim. run 2	
y-axis position (in.)	temp. (°F)	y-axis position (in.)	temp. (°F)	y-axis position (in.)	temp. (°F)	y-axis position (in.)	temp. (°F)
-4.61	82.63	-4.81	78.27	-4.91	71.71	-4.91	80.96
-4.41	83.23	-4.66	64.74	-4.66	63.93	-4.66	90.66
-3.91	81.26	-4.56	64.09	-4.41	62.25	-4.41	82.74
-3.42	76.32	-4.41	65.46	-3.91	61.88	-3.91	93.08
-2.95	76.82	-4.06	65.45	-3.41	62.16	-3.41	80.36
-2.88	83.40	-3.91	66.35	-2.91	63.94	-2.91	80.65
-2.72	90.44	-3.58	73.28	-2.71	62.21	-2.71	77.87
-2.48	491.97	-3.42	68.75	-2.61	66.26	-2.61	75.40
-2.25	724.20	-3.27	72.18	-2.51	64.38	-2.51	85.10
-2.17	735.50	-3.11	72.25	-2.41	93.93	-2.41	144.74
-2.09	745.70	-2.95	76.89	-2.31	345.50	-2.31	412.34
-2.02	752.70	-2.80	83.80	-2.21	628.32	-2.21	610.99
-1.94	755.90	-2.64	84.76	-2.11	687.17	-2.11	682.26
-1.86	754.60	-2.48	296.09	-1.91	716.26	-1.91	720.38
-1.70	764.00	-2.33	679.10	-1.41	740.70	-1.41	743.05
-1.55	770.94	-2.17	733.93	-0.91	744.00	-0.91	750.70
-1.39	776.53	-2.02	755.65	-0.41	739.86	-0.41	746.22
-1.23	778.60	-1.86	767.19			-0.16	744.77
-1.00	777.47	-1.70	779.42			0.09	742.96
-0.84	778.24	-1.55	787.11				
-0.69	775.99	-1.39	792.81				
-0.56	775.06	-1.23	790.59				
-0.41	776.77	-1.00	790.52				
-0.25	777.44	-0.84	789.38				
-0.16	780.58	-0.56	793.54				
0.00	780.55	-0.41	794.01				
		-0.25	791.91				
		-0.16	793.44				
		0.00	794.37				

Table A3. X-axis pressure data measured at the exit plane; see figure 24(c)

run 3		run 4		run 4 (cont.)	
x-axis position (in.)	pressure (psig)	x-axis position (in.)	pressure (psig)	x-axis position (in.)	pressure (psig)
0.00	1.007	-4.50	0.004	0.00	0.988
0.16	0.992	-4.00	0.004	0.16	0.987
0.31	0.996	-3.59	0.004	0.31	0.977
0.47	1.004	-3.44	0.004	0.47	0.973
0.63	1.010	-3.28	0.004	0.63	0.984
0.78	0.989	-3.13	0.005	0.78	0.978
0.94	0.990	-2.97	0.004	0.94	0.961
1.09	0.979	-2.81	0.004	1.09	0.953
1.25	0.962	-2.66	0.005	1.25	0.937
1.41	0.955	-2.50	0.006	1.41	0.929
1.56	0.992	-2.42	0.004	1.56	0.948
1.72	1.030	-2.34	0.005	1.72	0.985
1.88	1.022	-2.27	0.534	1.88	0.981
2.03	0.943	-2.19	0.657	1.95	0.941
2.19	0.779	-2.11	0.720	2.03	0.888
2.34	0.004	-2.03	0.766	2.11	0.818
2.50	0.005	-1.95	0.812	2.19	0.718
2.66	0.005	-1.88	0.860	2.27	0.346
2.81	0.005	-1.72	0.925	2.34	0.006
2.97	0.005	-1.56	0.964	2.42	0.006
3.13	0.005	-1.41	0.976	2.50	0.006
		-1.25	0.986	2.66	0.006
		-1.09	0.980	2.81	0.006
		-0.94	0.966	2.97	0.006
		-0.78	0.978	3.13	0.006
		-0.63	0.985	3.28	0.006
		-0.47	0.980	3.59	0.006
		-0.31	0.985		
		-0.16	0.975		

Table A4. X-axis temperature data measured at the exit plane; see figure 24(d)

run 3		run 4		run 4 (cont.)	
x-axis position (in.)	temp. (°F)	x-axis position (in.)	temp. (°F)	x-axis position (in.)	temp. (°F)
0.00	792.44	-4.50	86.74	0.00	801.95
0.16	795.12	-4.00	79.18	0.16	801.25
0.31	794.75	-3.59	85.21	0.31	800.94
0.47	795.69	-3.44	85.77	0.47	800.47
0.63	792.39	-3.28	87.29	0.63	800.59
0.78	792.41	-3.13	81.60	0.78	801.29
0.94	791.93	-2.97	88.00	0.94	800.56
1.09	793.55	-2.81	90.49	1.09	800.11
1.25	795.07	-2.66	86.27	1.25	803.22
1.41	796.79	-2.50	86.21	1.41	804.66
1.56	796.92	-2.42	88.28	1.56	806.56
1.72	795.20	-2.34	160.02	1.72	805.00
1.88	794.72	-2.27	726.78	1.88	801.50
2.03	789.82	-2.19	770.63	1.95	799.83
2.19	782.74	-2.11	775.84	2.03	796.88
2.34	247.56	-2.03	778.11	2.11	791.63
2.50	78.42	-1.95	781.29	2.19	786.99
2.66	67.76	-1.88	779.90	2.27	753.11
2.81	66.24	-1.72	786.24	2.34	210.54
2.97	64.99	-1.56	789.56	2.42	125.95
3.13	64.80	-1.41	797.79	2.50	91.23
		-1.25	797.58	2.66	92.79
		-1.09	798.62	2.81	86.10
		-0.94	801.15	2.97	87.89
		-0.78	801.33	3.13	86.18
		-0.63	804.16	3.28	90.02
		-0.47	802.06	3.59	80.03
		-0.31	801.58		
		-0.16	804.46		

Table A5. Y-axis pressure data measured one-half diameter downstream; see figure 25(a)

run 5		run 6		prelim. run 3		prelim. run 4	
y-axis position (in.)	pressure (psig)	y-axis position (in.)	pressure (psig)	y-axis position (in.)	pressure (psig)	y-axis position (in.)	pressure (psig)
-5.00	0.000	-5.00	0.008	-4.50	0.023	-4.75	0.000
-4.84	0.000	-4.84	0.007	-4.25	0.017	-4.50	0.000
-4.25	0.000	-4.25	0.009	-3.75	0.016	-4.25	0.001
-4.09	0.000	-4.09	0.008	-3.25	0.013	-3.75	0.000
-3.75	0.000	-3.75	0.008	-2.75	0.011	-3.25	0.000
-3.59	0.000	-3.59	0.007	-2.55	0.008	-2.75	0.000
-3.42	0.000	-3.42	0.008	-2.45	0.004	-2.55	0.000
-3.27	0.000	-3.27	0.007	-2.35	0.010	-2.45	0.000
-3.07	0.000	-3.07	0.007	-2.25	0.029	-2.35	0.001
-3.00	0.000	-2.92	0.005	-2.15	0.071	-2.25	0.017
-2.92	0.000	-2.76	0.017	-2.05	0.155	-2.15	0.057
-2.84	0.001	-2.60	0.080	-1.95	0.285	-2.05	0.133
-2.76	0.016	-2.45	0.248	-1.75	0.603	-1.95	0.240
-2.68	0.052	-2.29	0.506	-1.25	0.950	-1.75	0.532
-2.60	0.106	-2.14	0.771	-0.75	0.942	-1.25	0.936
-2.53	0.185	-1.98	0.901	-0.25	0.916	-0.75	0.940
-2.45	0.283	-1.88	0.961	0.00	0.910	-0.25	0.899
-2.37	0.404	-1.72	1.019	0.25	0.916	0.00	0.887
-2.29	0.527	-1.50	1.030			0.25	0.883
-2.21	0.624	-1.25	1.005				
-2.14	0.714	-0.88	0.983	Run 5 (cont.)			
-2.06	0.772	-0.72	0.975	-0.88	0.942		
-1.98	0.819	-0.47	0.984	-0.72	0.933		
-1.88	0.876	-0.25	0.963	-0.63	0.927		
-1.72	0.969	-0.09	0.953	-0.47	0.917		
-1.50	1.017	0.00	0.960	-0.25	0.905		
-1.34	0.993	0.16	0.968	-0.09	0.923		
-1.25	0.978			0.00	0.927		
-1.09	0.972			0.16	0.932		

Table A6. Y-axis temperature data measured one-half diameter downstream; see figure 25(b)

run 5		run 6		prelim. run 3		prelim. run 4	
y-axis position (in.)	temp. (°F)	y-axis position (in.)	temp. (°F)	y-axis position (in.)	temp. (°F)	y-axis position (in.)	temp. (°F)
-5.16	77.97	-5.16	86.53	-4.66	80.52	-4.91	75.64
-5.00	78.43	-5.00	82.03	-4.41	81.45	-4.66	76.28
-4.41	72.25	-4.41	67.69	-3.91	81.65	-4.41	78.06
-4.25	79.72	-4.25	78.23	-3.41	80.30	-3.91	78.30
-3.91	78.83	-3.91	76.81	-2.91	80.72	-3.41	76.63
-3.75	83.95	-3.75	85.54	-2.71	85.48	-2.91	78.91
-3.58	86.77	-3.58	70.99	-2.61	84.96	-2.71	77.31
-3.42	88.37	-3.42	73.32	-2.51	106.48	-2.61	83.47
-3.23	90.47	-3.23	86.17	-2.41	136.34	-2.51	98.00
-3.15	89.60	-3.07	96.76	-2.31	195.61	-2.41	126.42
-3.07	92.22	-2.92	117.73	-2.21	264.21	-2.31	183.15
-3.00	86.99	-2.76	202.52	-2.11	330.22	-2.21	247.33
-2.92	100.94	-2.60	313.87	-1.91	457.36	-2.11	308.95
-2.84	107.20	-2.45	430.28	-1.41	719.84	-1.91	420.78
-2.76	122.69	-2.29	525.25	-0.91	751.60	-1.41	707.20
-2.68	181.29	-2.14	635.86	-0.41	748.41	-0.91	742.64
-2.60	230.04	-2.03	694.78	-0.16	749.50	-0.41	745.13
-2.53	263.09	-1.88	746.91	0.09	745.03	-0.16	752.09
-2.45	318.82	-1.66	777.41			0.09	753.85
-2.37	358.36	-1.41	786.01				
-2.29	414.22	-1.03	790.28	run 5 (cont.)			
-2.21	456.02	-0.88	789.56	-1.03	751.26		
-2.14	508.31	-0.63	790.12	-0.88	753.44		
-2.03	574.35	-0.41	789.25	-0.78	752.21		
-1.88	664.94	-0.25	785.69	-0.63	754.74		
-1.66	725.36	-0.16	785.39	-0.41	749.00		
-1.50	740.11	0.00	784.25	-0.25	749.24		
-1.41	743.66			-0.16	751.68		
-1.25	751.49			0.00	753.69		

Table A7. X-axis pressure data measured one-half diameter downstream; see figure 25(c)

run 7		run 8		run 8 (cont.)	
x-axis position (in.)	pressure (psig)	x-axis position (in.)	pressure (psig)	x-axis position (in.)	pressure (psig)
0.00	0.990	-4.50	0.006	0.00	0.977
0.16	0.978	-4.00	0.006	0.16	0.981
0.31	0.975	-3.75	0.005	0.31	0.957
0.47	0.981	-3.44	0.006	0.47	0.957
0.63	0.978	-3.28	0.004	0.63	0.947
0.78	0.961	-3.13	0.004	0.78	0.959
0.94	0.956	-2.97	0.003	0.94	0.932
1.09	0.952	-2.81	0.001	1.09	0.917
1.25	0.943	-2.66	0.011	1.25	0.920
1.41	0.934	-2.50	0.073	1.41	0.913
1.56	0.949	-2.42	0.137	1.56	0.932
1.72	0.989	-2.34	0.225	1.72	0.955
1.88	0.977	-2.27	0.335	1.88	0.969
1.95	0.963	-2.19	0.452	1.95	0.939
2.03	0.927	-2.11	0.580	2.03	0.886
2.11	0.835	-2.03	0.667	2.11	0.767
2.19	0.657	-1.95	0.736	2.19	0.597
2.27	0.469	-1.88	0.780	2.27	0.411
2.34	0.284	-1.72	0.852	2.34	0.251
2.42	0.157	-1.56	0.902	2.42	0.138
2.50	0.073	-1.41	0.936	2.50	0.062
2.66	0.002	-1.25	0.962	2.66	0.008
2.81	-0.003	-1.09	0.952	2.81	0.002
2.97	-0.003	-0.94	0.953	2.97	0.004
3.13	-0.002	-0.78	0.959	3.13	0.005
3.28	-0.001	-0.63	0.979	3.28	0.005
3.59	-0.001	-0.47	0.966	3.59	0.005
		-0.31	0.974		
		-0.16	0.967		

Table A8. X-axis temperature data measured one-half diameter downstream; see figure 25(d)

run 7		run 8		run 8 (cont.)	
x-axis position (in.)	temp. (°F)	x-axis position (in.)	temp. (°F)	x-axis position (in.)	temp. (°F)
0.00	790.76	-4.50	99.89	0.00	795.84
0.16	788.76	-4.00	84.25	0.16	796.53
0.31	786.88	-3.75	92.06	0.31	798.80
0.47	787.10	-3.44	88.85	0.47	798.99
0.63	788.35	-3.28	78.50	0.63	798.76
0.78	786.39	-3.13	87.10	0.78	794.47
0.94	783.41	-2.97	81.40	0.94	795.67
1.09	784.64	-2.81	129.23	1.09	796.67
1.25	785.51	-2.66	224.50	1.25	793.36
1.41	793.19	-2.50	358.48	1.41	795.83
1.56	792.54	-2.42	412.86	1.56	800.67
1.72	792.70	-2.34	463.04	1.72	802.86
1.88	792.12	-2.27	520.88	1.88	795.54
1.95	783.24	-2.19	579.31	1.95	786.96
2.03	754.72	-2.11	642.14	2.03	756.46
2.11	695.01	-2.03	692.39	2.11	693.02
2.19	616.08	-1.95	748.83	2.19	612.90
2.27	543.39	-1.88	772.00	2.27	547.81
2.34	474.10	-1.72	783.88	2.34	475.59
2.42	410.23	-1.56	787.75	2.42	407.21
2.50	341.75	-1.41	787.07	2.50	336.77
2.66	198.24	-1.25	786.71	2.66	194.32
2.81	93.82	-1.09	792.89	2.81	94.80
2.97	70.78	-0.94	794.46	2.97	74.70
3.13	68.17	-0.78	797.18	3.13	70.27
3.28	67.55	-0.63	795.08	3.28	73.90
3.59	67.54	-0.47	794.76	3.59	68.62
		-0.31	789.73		
		-0.16	797.58		

Table A9. Y-axis pressure data measured one diameter downstream; see figure 26(a)

run 9		run 10		prelim. run 8	
y-axis position (in.)	pressure (psig)	y-axis position (in.)	pressure (psig)	y-axis position (in.)	pressure (psig)
-5.25	0.000	-5.25	0.008	-4.50	0.002
-5.09	0.000	-5.09	0.008	-3.50	0.004
-4.75	0.000	-4.75	0.007	-3.05	0.001
-4.59	0.000	-4.59	0.007	-2.80	0.000
-4.25	0.000	-4.25	0.007	-2.55	0.024
-4.09	0.000	-4.09	0.007	-2.25	0.122
-3.75	0.000	-3.75	0.006	-1.75	0.555
-3.59	0.000	-3.59	0.005	-1.25	0.953
-3.35	0.000	-3.35	0.005	-1.25	0.941
-3.27	0.000	-3.19	0.007	-0.75	0.937
-3.19	0.000	-3.04	0.021	-0.25	0.927
-3.12	0.002	-2.88	0.049	0.00	0.914
-3.04	0.015	-2.72	0.113	0.25	0.914
-2.96	0.028	-2.57	0.211		
-2.88	0.049	-2.41	0.358		
-2.80	0.077	-2.26	0.538		
-2.72	0.110	-2.09	0.757		
-2.65	0.151	-1.75	1.031		
-2.57	0.196	-1.59	1.040	run 9 (cont.)	
-2.49	0.259	-1.23	1.009	-1.08	0.945
-2.41	0.325	-0.84	0.981	-0.84	0.928
-2.33	0.398	-0.53	0.983	-0.69	0.927
-2.26	0.486	-0.41	0.969	-0.53	0.908
-2.25	0.493	-0.25	0.958	-0.41	0.897
-2.09	0.654	0.00	0.955	-0.25	0.905
-1.75	0.923	0.16	0.992	-0.09	0.915
-1.59	0.979			0.00	0.922
-1.23	0.963			0.16	0.933

Table A10. Y-axis temperature data measured one diameter downstream; see figure 26(b)

run 9		run 10		prelim. run 8	
y-axis position (in.)	temp. (°F)	y-axis position (in.)	temp. (°F)	y-axis position (in.)	temp. (°F)
-5.41	63.06	-5.41	72.94	-4.66	85.34
-5.25	63.44	-5.25	73.21	-3.66	80.75
-4.91	63.44	-4.91	71.13	-3.21	86.47
-4.75	63.45	-4.75	70.50	-2.96	96.35
-4.41	64.13	-4.41	68.09	-2.71	160.46
-4.25	63.97	-4.25	72.69	-2.41	264.33
-3.91	64.00	-3.91	72.07	-1.91	472.51
-3.75	66.10	-3.75	71.63	-1.41	676.77
-3.51	80.16	-3.51	79.73	-1.41	685.34
-3.43	93.29	-3.35	91.57	-0.91	750.10
-3.35	107.59	-3.19	131.28	-0.41	740.64
-3.27	127.02	-3.04	177.20	-0.16	740.69
-3.19	153.84	-2.88	245.91	0.09	742.59
-3.12	178.55	-2.72	361.08		
-3.04	204.42	-2.57	381.05		
-2.96	237.02	-2.41	447.89		
-2.88	266.70	-2.25	513.43		
-2.80	299.76	-1.91	672.99		
-2.72	329.67	-1.75	733.09	run 9 (cont.)	
-2.65	362.31	-1.39	773.57	-1.23	774.34
-2.57	394.46	-1.00	778.28	-1.00	778.58
-2.49	426.42	-0.69	780.91	-0.84	777.22
-2.41	462.40	-0.56	781.89	-0.69	776.83
-2.41	463.05	-0.41	779.54	-0.56	779.11
-2.25	530.81	-0.16	780.63	-0.41	777.31
-1.91	677.25	0.00	776.69	-0.25	777.41
-1.75	726.79			-0.16	775.96
-1.39	771.97			0.00	778.51

Table A11. X-axis pressure data measured one diameter downstream; see figure 26(c)

run 11		run 12		prelim. run 9	
x-axis position (in.)	pressure (psig)	x-axis position (in.)	pressure (psig)	x-axis position (in.)	pressure (psig)
0.00	0.986	-4.06	0.006	0.00	0.913
0.16	0.971	-3.75	0.007	0.25	0.918
0.31	0.962	-3.44	0.006	0.75	0.925
0.47	0.967	-3.13	0.007	1.25	0.935
0.63	0.957	-2.81	0.040	1.75	0.827
0.78	0.940	-2.50	0.161	2.25	0.320
0.94	0.921	-2.19	0.407	2.65	0.061
1.09	0.906	-1.88	0.892	2.75	0.036
1.25	0.919	-1.56	0.891	2.85	0.016
1.41	0.919	-1.25	0.962	2.95	0.003
1.56	0.934	-0.94	0.963	3.05	0.000
1.72	0.939	-0.63	0.979	3.25	0.000
1.88	0.903	-0.31	0.971	3.75	0.000
1.95	0.858	0.00	0.986		
2.03	0.772	0.31	0.985		
2.11	0.671	0.63	0.947		
2.19	0.566	0.94	0.938		
2.27	0.451	1.25	0.931		
2.34	0.345	1.56	0.943		
2.42	0.256	1.88	0.929		
2.50	0.179	2.19	0.575		
2.66	0.072	2.50	0.198		
2.81	0.017	2.81	0.034		
2.97	0.000	3.13	0.005		
3.13	0.000	3.44	0.005		
3.28	0.000	3.75	0.007		
3.59	0.000	4.06	0.008		
3.91	0.000				
4.22	0.000				

Table A12. X-axis temperature data measured one diameter downstream; see figure 26(d)

run 11		run 12		prelim. run 9	
x-axis position (in.)	temp. (°F)	x-axis position (in.)	temp. (°F)	x-axis position (in.)	temp. (°F)
0.00	789.10	-4.06	73.07	0.00	743.78
0.16	788.31	-3.75	88.07	0.25	742.48
0.31	789.20	-3.44	89.91	0.75	749.50
0.47	790.86	-3.13	147.00	1.25	744.97
0.63	788.75	-2.81	289.09	1.75	670.24
0.78	788.79	-2.50	406.11	2.25	448.91
0.94	787.26	-2.19	559.10	2.65	287.48
1.09	785.91	-1.88	776.12	2.75	245.46
1.25	784.50	-1.56	773.72	2.85	207.55
1.41	788.51	-1.25	784.31	2.95	172.30
1.56	790.34	-0.94	789.53	3.05	137.88
1.72	772.62	-0.63	787.77	3.25	102.50
1.88	723.32	-0.31	792.44	3.75	85.54
1.95	681.61	0.00	791.60		
2.03	637.28	0.31	787.76		
2.11	592.00	0.63	793.48		
2.19	549.62	0.94	786.39		
2.27	509.14	1.25	785.44		
2.34	472.21	1.56	789.31		
2.42	434.21	1.88	727.08		
2.50	396.64	2.19	557.32		
2.66	324.79	2.50	409.57		
2.81	251.65	2.81	250.71		
2.97	178.31	3.13	121.99		
3.13	117.49	3.44	71.53		
3.28	84.84	3.75	65.46		
3.59	67.46	4.06	64.96		
3.91	67.17				
4.22	66.69				

Table A13. Y-axis pressure data measured two diameters downstream; see figure 27(a)

run 13		run 13 (cont.)		run 14		prelim. run 10	
y-axis position (in.)	pressure (psig)	y-axis position (in.)	pressure (psig)	y-axis position (in.)	pressure (psig)	y-axis position (in.)	pressure (psig)
-5.25	0.000	-2.25	0.387	-5.25	0.005	-4.75	0.011
-5.09	0.000	-2.09	0.486	-5.09	0.005	-3.60	0.003
-4.25	0.000	-1.94	0.625	-4.25	0.004	-3.35	0.003
-4.09	0.000	-1.75	0.764	-4.09	0.002	-3.10	0.024
-4.06	0.000	-1.59	0.872	-4.06	0.003	-2.75	0.054
-3.98	0.000	-1.25	0.970	-3.90	0.004	-2.25	0.181
-3.90	0.000	-1.09	0.977	-3.75	0.009	-1.75	0.434
-3.82	0.002	-0.75	0.946	-3.59	0.013	-1.25	0.779
-3.75	0.004	-0.59	0.926	-3.43	0.034	-0.75	0.932
-3.67	0.005	-0.25	0.917	-3.28	0.052	-0.25	0.917
-3.59	0.010	-0.09	0.926	-3.12	0.083	0.00	0.931
-3.51	0.015	0.00	0.930	-2.96	0.122	0.25	0.929
-3.43	0.017	0.16	0.936	-2.73	0.221		
-3.36	0.023			-2.56	0.300		
-3.28	0.033			-2.41	0.407		
-3.20	0.043			-2.25	0.524		
-3.12	0.053			-1.94	0.768		
-3.04	0.065			-1.75	0.884		
-2.96	0.083			-1.25	1.008		
-2.89	0.100			-0.75	0.975		
-2.73	0.143			-0.25	0.945		
-2.65	0.165			-0.09	0.957		
-2.56	0.205			0.00	0.961		
-2.41	0.287			0.16	0.976		

Table A14. Y-axis temperature data measured two diameters downstream; see figure 27(b)

run 13		run 13 (cont.)		run 14		prelim. run 16	
y-axis position (in.)	temp. (°F)	y-axis position (in.)	temp. (°F)	y-axis position (in.)	temp. (°F)	y-axis position (in.)	temp. (°F)
-5.41	62.87	-2.41	427.20	-5.41	65.09	-4.91	74.68
-5.25	62.87	-2.25	461.44	-5.25	62.95	-3.76	86.45
-4.41	69.44	-2.09	513.09	-4.41	69.80	-3.51	107.91
-4.25	76.01	-1.91	561.61	-4.25	75.26	-3.26	145.52
-4.21	84.97	-1.75	615.91	-4.21	80.31	-2.91	211.46
-4.14	87.28	-1.41	707.20	-4.06	93.10	-2.41	315.50
-4.06	98.30	-1.25	740.89	-3.90	117.92	-1.91	440.94
-3.98	106.50	-0.91	772.58	-3.75	134.40	-1.41	561.24
-3.90	111.13	-0.75	777.92	-3.59	169.35	-0.91	692.47
-3.82	118.33	-0.41	779.00	-3.43	201.03	-0.41	742.85
-3.75	137.72	-0.25	779.32	-3.28	229.07	-0.16	738.77
-3.67	148.57	-0.16	779.68	-3.12	262.25	0.09	733.79
-3.59	156.44	0.00	779.74	-2.89	322.39		
-3.51	173.20			-2.72	368.28		
-3.43	187.07			-2.56	415.19		
-3.36	200.99			-2.41	461.86		
-3.28	216.07			-2.09	542.06		
-3.20	229.76			-1.91	596.86		
-3.12	247.64			-1.41	731.83		
-3.04	268.09			-0.91	780.67		
-2.89	302.55			-0.41	782.58		
-2.81	317.98			-0.25	781.74		
-2.72	343.37			-0.16	785.33		
-2.56	385.30			0.00	778.01		

Table A15. X-axis pressure data measured two diameters downstream; see figure 27(c)

run 15		run 15 (cont.)		run 16		run 16 (cont.)	
x-axis position (in.)	pressure (psig)	x-axis position (in.)	pressure (psig)	x-axis position (in.)	pressure (psig)	x-axis position (in.)	pressure (psig)
0.00	0.968	2.19	0.488	-4.56	0.008	0.63	0.919
0.16	0.956	2.27	0.424	-4.06	0.008	0.94	0.903
0.31	0.946	2.34	0.372	-3.75	0.011	1.25	0.858
0.47	0.936	2.42	0.318	-3.44	0.023	1.56	0.786
0.63	0.925	2.50	0.283	-3.13	0.068	1.88	0.714
0.78	0.911	2.66	0.204	-2.81	0.127	2.19	0.501
0.94	0.895	2.81	0.133	-2.50	0.246	2.50	0.308
1.09	0.881	2.97	0.081	-2.19	0.407	2.81	0.163
1.25	0.872	3.13	0.046	-1.88	0.617	3.13	0.074
1.41	0.859	3.28	0.017	-1.56	0.814	3.44	0.029
1.56	0.831	3.59	0.000	-1.25	0.936	3.75	0.010
1.72	0.767	3.91	0.000	-0.94	0.962	4.06	0.004
1.88	0.685	4.22	0.000	-0.63	0.956		
1.95	0.636	4.53	0.000	-0.31	0.967		
2.03	0.616	4.84	0.000	0.00	0.987		
2.11	0.580	5.16	0.000	0.31	0.945		

Table A16. X-axis temperature data measured two diameters downstream; see figure 27(d)

run 15		run 15 (cont.)		run 16		run 16 (cont.)	
x-axis position (in.)	temp. (°F)	x-axis position (in.)	temp. (°F)	x-axis position (in.)	temp. (°F)	x-axis position (in.)	temp. (°F)
0.00	792.12	2.19	513.36	-4.56	73.02	0.63	783.47
0.16	794.34	2.27	492.39	-4.06	96.62	0.94	755.61
0.31	793.58	2.34	473.96	-3.75	148.28	1.25	698.71
0.47	794.44	2.42	449.24	-3.44	204.41	1.88	605.21
0.63	786.38	2.50	433.71	-3.13	291.73	2.19	520.22
0.78	785.97	2.66	394.50	-2.81	351.60	2.50	440.59
0.94	781.42	2.81	354.33	-2.50	434.67	2.81	380.79
1.09	770.99	2.97	312.76	-2.19	519.23	3.13	285.83
1.25	753.73	3.13	278.87	-1.88	604.95	3.44	213.81
1.41	727.61	3.28	240.88	-1.56	697.30	3.75	150.19
1.56	689.02	3.59	177.52	-1.25	762.09	4.06	104.26
1.72	642.05	3.91	112.06	-0.94	789.30		
1.88	597.25	4.22	80.53	-0.63	792.10		
1.95	578.61	4.53	69.40	-0.31	790.46		
2.03	565.95	4.84	66.69	0.00	784.68		
2.11	541.73	5.16	65.45	0.31	792.03		

Table A17. Y-axis pressure data measured three diameters downstream; see figure 28(a)

run 17		run 17 (cont.)		run 18		prelim. run 11	
y-axis position (in.)	pressure (psig)	y-axis position (in.)	pressure (psig)	y-axis position (in.)	pressure (psig)	y-axis position (in.)	pressure (psig)
-5.39	0.000	-3.20	0.077	-4.92	0.000	-5.25	0.000
-5.24	0.000	-3.05	0.104	-4.77	0.000	-4.15	0.000
-5.08	0.000	-2.75	0.195	-4.45	0.003	-3.90	0.006
-4.92	0.001	-2.50	0.281	-4.30	0.009	-3.65	0.010
-4.77	0.001	-2.25	0.368	-4.14	0.020	-3.25	0.035
-4.61	0.003	-2.09	0.459	-3.99	0.029	-2.25	0.153
-4.45	0.003	-1.75	0.681	-3.83	0.047	-1.75	0.314
-4.38	0.004	-1.59	0.758	-3.67	0.048	-1.25	0.527
-4.30	0.003	-1.25	0.894	-3.52	0.087	-0.75	0.712
-4.22	0.002	-1.09	0.932	-3.36	0.126	-0.25	0.852
-4.14	0.003	-0.75	0.936	-3.05	0.212	0.00	0.880
-4.06	0.010	-0.59	0.927	-2.75	0.324		
-3.99	0.007	-0.25	0.933	-2.50	0.435		
-3.91	0.012	-0.09	0.936	-2.25	0.526		
-3.83	0.017	0.00	0.940	-1.75	0.773		
-3.75	0.019	0.16	0.940	-1.25	0.933		
-3.67	0.026	0.31	0.942	-0.75	0.969		
-3.60	0.027	0.47	0.937	-0.25	0.935		
-3.52	0.037			-0.09	0.939		
-3.44	0.043			0.00	0.945		
-3.36	0.057			0.16	0.947		

Table A18. Y-axis temperature data measured three diameters downstream; see figure 28(b)

run 17		run 17 (cont.)		run 18		prelim. run 11	
y-axis position (in.)	temp. (°F)	y-axis position (in.)	temp. (°F)	y-axis position (in.)	temp. (°F)	y-axis position (in.)	temp. (°F)
-5.55	68.58	-3.36	247.01	-5.08	84.00	-5.41	72.60
-5.39	73.41	-3.20	267.33	-4.92	103.62	-4.31	97.02
-5.24	77.79	-2.91	335.64	-4.61	120.85	-4.06	121.46
-5.08	78.45	-2.66	368.15	-4.45	130.49	-3.81	137.00
-4.92	86.21	-2.41	417.48	-4.30	159.81	-3.41	182.78
-4.77	102.86	-2.25	451.10	-4.14	179.55	-2.41	316.32
-4.61	109.23	-1.91	527.20	-3.99	206.04	-1.91	403.93
-4.53	108.78	-1.75	558.00	-3.83	206.84	-1.41	486.86
-4.45	112.71	-1.41	631.77	-3.67	247.09	-0.91	548.86
-4.38	106.82	-1.25	669.45	-3.52	283.65	-0.41	626.12
-4.30	110.83	-0.91	729.07	-3.20	342.10	-0.16	652.43
-4.22	137.99	-0.75	748.52	-2.91	396.53		
-4.14	132.88	-0.41	769.86	-2.66	441.27		
-4.06	140.30	-0.25	776.54	-2.41	477.89		
-3.99	154.40	-0.16	775.83	-1.91	564.61		
-3.9[illegible]	159.83	0.00	774.08	-1.41	673.82		
-3.83	172.16	0.16	772.48	-0.91	750.28		
-3.75	182.31	0.31	765.36	-0.41	782.88		
-3.67	198.24			-0.25	785.73		
-3.60	205.49			-0.16	786.43		
-3.52	226.38			0.00	782.54		

Table A19. X-axis pressure data measured three diameters downstream; see figure 28(c)

run 19		run 19 (cont.)	
x-axis position (in.)	pressure (psig)	x-axis position (in.)	pressure (psig)
-5.00	0.006	0.00	0.960
-4.56	0.007	0.31	0.959
-4.06	0.021	0.63	0.936
-3.75	0.039	0.94	0.873
-3.44	0.079	1.25	0.806
-3.13	0.129	1.56	0.718
-2.81	0.203	1.88	0.588
-2.50	0.294	2.19	0.467
-2.19	0.429	2.50	0.343
-1.88	0.571	2.81	0.236
-1.56	0.728	3.13	0.147
-1.25	0.861	3.44	0.091
-0.94	0.939	3.75	0.048
-0.63	0.966	4.06	0.022
-0.31	0.959	4.56	0.006
		5.00	0.008

Table A20. X-axis temperature data measured three diameters downstream; see figure 28(d)

run 19		run 19 (cont.)	
x-axis position (in.)	temp. (°F)	x-axis position (in.)	temp. (°F)
-5.00	87.91	0.00	784.75
-4.56	122.31	0.31	779.26
-4.06	177.47	0.63	759.73
-3.75	216.12	0.94	724.91
-3.44	266.24	1.25	664.27
-3.13	321.11	1.56	599.57
-2.81	375.16	1.88	547.32
-2.50	432.52	2.19	489.53
-2.19	494.81	2.50	440.93
-1.88	550.93	2.81	388.93
-1.56	619.45	3.13	325.59
-1.25	684.87	3.44	277.76
-0.94	742.01	3.75	228.59
-0.63	773.10	4.06	181.44
-0.31	781.53	4.56	124.76
		5.00	92.32

Table A21. Y-axis pressure data measured four diameters downstream; see figure 29(a)

run 20		run 20 (cont.)		run 21		prelim. run 12	
y-axis position (in.)	pressure (psig)	y-axis position (in.)	pressure (psig)	y-axis position (in.)	pressure (psig)	y-axis position (in.)	pressure (psig)
-5.75	0.002	-1.75	0.610	-5.75	0.000	-5.25	0.000
-5.59	0.001	-1.59	0.688	-5.59	0.001	-4.75	0.000
-5.25	0.003	-1.50	0.704	-5.25	0.001	-4.50	0.000
-5.09	0.001	-1.34	0.772	-5.09	0.003	-4.25	0.006
-4.77	0.006	-1.25	0.794	-4.77	0.011	-3.25	0.049
-4.69	0.010	-1.09	0.850	-4.62	0.016	-2.25	0.160
-4.62	0.012	-0.75	0.902	-4.46	0.024	-1.25	0.403
-4.54	0.013	-0.59	0.918	-4.30	0.035	-0.75	0.564
-4.46	0.028	-0.25	0.937	-4.15	0.043	-0.25	0.694
-4.38	0.022	-0.09	0.934	-3.75	0.087	0.00	0.746
-4.30	0.022	0.00	0.915	-3.25	0.171	0.25	0.802
-4.23	0.019	0.16	0.916	-2.75	0.306		
-4.15	0.036			-2.59	0.354		
-3.75	0.058			-2.25	0.480		
-3.59	0.077			-2.00	0.581		
-3.25	0.138			-1.75	0.687		
-3.09	0.142			-1.50	0.796		
-2.75	0.239			-1.25	0.884		
-2.59	0.292			-1.09	0.910		
-2.41	0.342			-0.75	0.943		
-2.25	0.457			-0.59	0.940		
-2.09	0.490			-0.25	0.937		
-2.00	0.517			-0.09	0.930		
-1.84	0.565			0.00	0.927		
-1.80	0.615			0.16	0.908		

Table A22. Y-axis temperature data measured four diameters downstream; see figure 29(b)

run 20		run 20 (cont.)		run 21		prelim. run 12	
y-axis position (in.)	temp. (°F)	y-axis position (in.)	temp. (°F)	y-axis position (in.)	temp. (°F)	y-axis position (in.)	temp. (°F)
-5.91	71.14	-1.91	498.99	-5.91	71.97	-5.41	85.00
-5.75	75.74	-1.75	530.24	-5.75	77.28	-4.91	93.30
-5.41	88.07	-1.66	534.24	-5.41	93.90	-4.66	112.25
-5.25	94.39	-1.50	564.33	-5.25	106.61	-4.41	136.95
-4.93	111.85	-1.41	582.29	-4.93	132.61	-3.41	214.60
-4.85	128.27	-1.25	605.46	-4.77	149.90	-2.41	322.28
-4.77	133.13	-0.91	661.14	-4.62	164.26	-1.41	432.62
-4.69	138.79	-0.75	685.84	-4.46	181.21	-0.91	492.10
-4.62	171.52	-0.41	723.82	-4.30	197.33	-0.41	535.50
-4.54	154.25	-0.25	734.22	-3.91	243.79	-0.16	565.47
-4.46	164.89	-0.16	726.02	-3.41	308.44	0.09	581.85
-4.38	153.22	0.00	730.48	-2.91	381.99		
-4.30	190.26			-2.75	403.69		
-3.91	221.55			-2.41	446.18		
-3.75	239.37			-2.16	483.92		
-3.41	290.83			-1.91	515.04		
-3.25	292.19			-1.66	555.19		
-2.91	354.20			-1.41	609.25		
-2.75	380.00			-1.25	630.89		
-2.56	399.78			-0.91	684.36		
-2.41	449.74			-0.75	707.46		
-2.25	461.24			-0.41	736.68		
-2.16	465.74			-0.25	742.62		
-2.00	484.74			-0.16	735.70		
-1.96	500.57			0.00	726.75		

Table A23. X-axis pressure data measured four diameters downstream; see figure 29(c)

run 22		run 22 (cont.)	
x-axis position (in.)	pressure (psig)	x-axis position (in.)	pressure (psig)
-6.00	0.007	0.00	0.921
-5.50	0.006	0.31	0.894
-5.00	0.008	0.63	0.838
-4.56	0.015	0.94	0.745
-4.06	0.037	1.25	0.669
-3.75	0.066	1.56	0.593
-3.44	0.110	1.88	0.485
-3.13	0.150	2.19	0.403
-2.81	0.208	2.50	0.326
-2.50	0.301	2.81	0.257
-2.19	0.409	3.13	0.196
-1.88	0.520	3.44	0.138
-1.56	0.653	3.75	0.096
-1.25	0.772	4.06	0.053
-0.94	0.861	4.56	0.023
-0.63	0.923	5.00	0.012
-0.31	0.928	5.50	0.006
		6.00	0.007

Table A24. X-axis temperature data measured four diameters downstream; see figure 29(d)

run 22		run 22 (cont.)	
x-axis position (in.)	temp. (°F)	x-axis position (in.)	temp. (°F)
-6.00	70.68	0.00	747.47
-5.50	86.91	0.31	724.10
-5.00	120.86	0.63	687.89
-4.56	161.61	0.94	633.08
-4.06	208.32	1.25	592.78
-3.75	251.89	1.56	548.16
-3.44	291.62	1.88	499.85
-3.13	331.27	2.19	461.55
-2.81	373.84	2.50	422.25
-2.50	425.43	2.81	381.52
-2.19	476.09	3.13	346.35
-1.88	520.24	3.44	305.11
-1.56	574.78	3.75	268.09
-1.25	634.23	4.06	223.22
-0.94	680.64	4.56	176.05
-0.63	724.84	5.00	144.34
-0.31	751.06	5.50	113.80
		6.00	84.57

Table A25. Y-axis pressure data measured five diameters downstream; see figure 30(a)

run 23		run 23 (cont.)		run 24		prelim. run 13	
y-axis position (in.)	pressure (psig)	y-axis position (in.)	pressure (psig)	y-axis position (in.)	pressure (psig)	y-axis position (in.)	pressure (psig)
-7.25	0.004	-3.13	0.177	-7.25	0.001	-6.75	0.000
-6.75	0.003	-2.97	0.189	-6.75	0.000	-5.25	0.006
-6.25	0.003	-2.81	0.219	-6.25	0.000	-5.00	0.004
-6.09	0.002	-2.66	0.248	-5.94	0.002	-4.75	0.003
-5.94	0.001	-2.50	0.304	-5.63	0.003	-4.25	0.020
-5.78	0.000	-2.34	0.348	-5.31	0.006	-3.25	0.072
-5.63	0.005	-2.19	0.418	-5.00	0.015	-2.25	0.186
-5.47	0.006	-2.03	0.433	-4.69	0.030	-1.75	0.260
-5.31	0.010	-1.88	0.484	-4.38	0.051	-1.25	0.343
-5.16	0.014	-1.25	0.700	-4.06	0.078	-0.75	0.451
-5.00	0.014	-1.09	0.748	-3.75	0.114	-0.25	0.563
-4.84	0.013	-0.75	0.821	-3.44	0.162	0.00	0.612
-4.69	0.029	-0.59	0.858	-3.13	0.219	0.25	0.622
-4.53	0.026	-0.25	0.875	-2.81	0.282		
-4.38	0.034	-0.09	0.869	-2.50	0.369		
-4.22	0.060	0.00	0.850	-2.19	0.462		
-4.06	0.064	0.16	0.841	-1.88	0.556		
-3.91	0.075			-1.25	0.737		
-3.75	0.075			-0.75	0.846		
-3.59	0.095			-0.25	0.864		
-3.44	0.131			0.00	0.840		
-3.28	0.139			0.16	0.801		

Table A26. Y-axis temperature data measured five diameters downstream; see figure 30(b)

run 23		run 23 (cont.)		run 24		prelim. run 13	
y-axis position (in.)	temp. (°F)	y-axis position (in.)	temp. (°F)	y-axis position (in.)	temp. (°F)	y-axis position (in.)	temp. (°F)
-7.41	63.60	-3.28	294.36	-7.41	68.23	-6.91	75.21
-6.91	66.38	-3.13	308.15	-6.91	70.92	-5.41	110.95
-6.41	69.82	-2.97	320.48	-6.41	80.15	-5.16	112.40
-6.25	79.42	-2.81	336.48	-6.09	95.75	-4.91	119.51
-6.09	75.76	-2.66	371.83	-5.78	109.32	-4.41	156.74
-5.94	82.17	-2.50	376.27	-5.47	123.78	-3.41	232.00
-5.78	91.91	-2.34	421.46	-5.16	146.70	-2.41	318.18
-5.63	107.06	-2.19	426.47	-4.84	171.97	-1.91	365.72
-5.47	116.86	-2.03	444.56	-4.53	199.08	-1.41	406.30
-5.31	138.87	-1.41	534.90	-4.22	225.77	-0.91	451.89
-5.16	140.83	-1.25	563.29	-3.91	258.55	-0.41	497.27
-5.00	145.84	-0.91	592.96	-3.59	292.95	-0.16	509.68
-4.84	164.56	-0.75	613.05	-3.28	324.21	0.09	521.38
-4.69	166.28	-0.41	644.50	-2.97	358.82		
-4.53	176.25	-0.25	650.91	-2.66	397.17		
-4.38	203.01	-0.16	640.85	-2.34	438.93		
-4.22	218.90	0.00	650.85	-2.03	473.19		
-4.06	232.50			-1.41	555.61		
-3.91	222.93			-0.91	611.84		
-3.75	242.38			-0.41	653.93		
-3.59	268.51			-0.16	657.08		
-3.44	273.98			0.00	656.31		

Table A27. X-axis pressure data measured five diameters downstream; see figure 30(c)

run 25		run 25 (cont.)	
x-axis position (in.)	pressure (psig)	x-axis position (in.)	pressure (psig)
-6.00	0.009	0.00	0.850
-5.50	0.013	0.31	0.804
-5.00	0.025	0.63	0.737
-4.56	0.037	0.94	0.665
-4.06	0.064	1.25	0.592
-3.75	0.097	1.56	0.504
-3.44	0.132	1.88	0.437
-3.13	0.175	2.19	0.367
-2.81	0.233	2.50	0.307
-2.50	0.302	2.81	0.249
-2.19	0.377	3.13	0.199
-1.88	0.462	3.44	0.149
-1.56	0.577	3.75	0.119
-1.25	0.682	4.06	0.084
-0.94	0.774	4.56	0.049
-0.63	0.837	5.00	0.027
-0.31	0.859	5.50	0.013
		6.00	0.008
		6.50	0.006
		7.00	0.006

Table A28. X-axis temperature data measured five diameters downstream; see figure 30(d)

run 25		run 25 (cont.)	
x-axis position (in.)	temp. (°F)	x-axis position (in.)	temp. (°F)
-6.00	96.81	0.00	668.83
-5.50	131.63	0.31	649.73
-5.00	167.75	0.63	618.80
-4.56	197.31	0.94	581.69
-4.06	237.81	1.25	549.95
-3.75	273.09	1.56	503.96
-3.44	305.53	1.88	475.69
-3.13	337.29	2.19	438.71
-2.81	378.89	2.50	407.82
-2.50	419.22	2.81	376.84
-2.19	453.62	3.13	338.04
-1.88	495.53	3.44	314.61
-1.56	529.36	3.75	282.01
-1.25	576.24	4.06	252.43
-0.94	618.29	4.56	209.59
-0.63	651.79	5.00	174.37
-0.31	669.65	5.50	143.80
		6.00	113.63
		6.50	93.37
		7.00	76.35

Table A29. Y-axis pressure data measured six diameters downstream; see figure 31(a)

run 26		run 26 (cont.)		run 27	
y-axis position (in.)	pressure (psig)	y-axis position (in.)	pressure (psig)	y-axis position (in.)	pressure (psig)
-7.25	0.006	-3.13	0.191	-8.25	0.001
-6.75	0.003	-2.97	0.238	-7.25	0.000
-6.25	0.006	-2.81	0.232	-6.25	0.002
-6.09	0.007	-2.66	0.295	-5.94	0.006
-5.94	0.006	-2.50	0.306	-5.63	0.014
-5.78	0.010	-2.34	0.346	-5.31	0.018
-5.63	0.013	-2.19	0.368	-5.00	0.030
-5.47	0.011	-2.03	0.422	-4.69	0.049
-5.31	0.016	-1.88	0.443	-4.38	0.075
-5.16	0.016	-1.25	0.609	-4.06	0.110
-5.00	0.023	-1.09	0.647	-3.75	0.149
-4.84	0.030	-0.75	0.710	-3.44	0.190
-4.69	0.031	-0.59	0.739	-3.13	0.234
-4.53	0.052	-0.25	0.763	-2.81	0.298
-4.38	0.059	-0.09	0.770	-2.50	0.362
-4.22	0.067	0.00	0.756	-2.19	0.429
-4.06	0.094	0.16	0.748	-1.88	0.500
-3.91	0.089			-1.25	0.627
-3.75	0.114			-0.75	0.723
-3.59	0.130			-0.25	0.756
-3.44	0.160			0.00	0.736
-3.28	0.192			0.16	0.720

Table A30. Y-axis temperature data measured six diameters downstream; see figure 31(b)

run 26		run 26 (cont.)		run 27	
y-axis position (in.)	temp. (°F)	y-axis position (in.)	temp. (°F)	y-axis position (in.)	temp. (°F)
-7.41	74.60	-3.28	309.68	-8.41	85.14
-6.91	73.26	-3.13	332.93	-7.41	89.89
-6.41	97.93	-2.97	333.60	-6.41	98.87
-6.25	109.50	-2.81	371.11	-6.09	117.26
-6.09	101.86	-2.66	371.91	-5.78	135.99
-5.94	116.85	-2.50	385.64	-5.47	151.71
-5.78	133.56	-2.34	395.94	-5.16	170.04
-5.63	128.59	-2.19	422.23	-4.84	194.63
-5.47	143.16	-2.03	430.04	-4.53	216.15
-5.31	145.72	-1.41	494.47	-4.22	240.16
-5.16	158.51	-1.25	502.85	-3.91	268.42
-5.00	171.56	-0.91	534.40	-3.59	296.74
-4.84	169.74	-0.75	548.46	-3.28	322.44
-4.69	202.34	-0.41	556.17	-2.97	353.36
-4.53	201.83	-0.25	572.80	-2.66	380.40
-4.38	211.28	-0.16	574.45	-2.34	410.45
-4.22	240.29	0.00	575.44	-2.03	438.00
-4.06	235.66			-1.41	491.84
-3.91	252.99			-0.91	533.06
-3.75	272.27			-0.41	558.89
-3.59	293.49			-0.16	568.53
-3.44	314.75			0.00	567.21

Table A31. X-axis pressure data measured six diameters downstream; see figure 31(c)

run 28		run 28 (cont.)	
x-axis position (in.)	pressure (psig)	x-axis position (in.)	pressure (psig)
-7.00	0.005	0.00	0.702
-6.50	0.005	0.31	0.668
-6.00	0.007	0.63	0.623
-5.50	0.013	0.94	0.564
-5.00	0.032	1.25	0.470
-4.56	0.045	1.56	0.419
-4.06	0.077	1.88	0.358
-3.75	0.113	2.19	0.304
-3.44	0.141	2.50	0.260
-3.13	0.187	2.81	0.205
-2.81	0.237	3.13	0.176
-2.50	0.293	3.44	0.147
-2.19	0.359	3.75	0.113
-1.88	0.449	4.06	0.087
-1.56	0.522	4.56	0.048
-1.25	0.607	5.00	0.027
-0.94	0.664	5.50	0.010
-0.63	0.708	6.00	0.002
-0.31	0.723	6.50	0.000
		7.00	0.000

Table A32. X-axis temperature data measured six diameters downstream; see figure 31(d)

run 28		run 28 (cont.)	
x-axis position (in.)	temp. (°F)	x-axis position (in.)	temp. (°F)
-7.00	90.48	0.00	583.56
-6.50	105.18	0.31	569.72
-6.00	128.40	0.63	545.77
-5.50	156.16	0.94	522.32
-5.00	192.47	1.25	495.55
-4.56	215.69	1.56	466.29
-4.06	257.30	1.88	439.63
-3.75	293.02	2.19	414.41
-3.44	310.90	2.50	388.22
-3.13	342.40	2.81	356.72
-2.81	378.51	3.13	337.83
-2.50	412.15	3.44	312.15
-2.19	441.19	3.75	282.44
-1.88	476.16	4.06	255.58
-1.56	505.86	4.56	216.03
-1.25	534.85	5.00	186.24
-0.94	559.22	5.50	159.04
-0.63	575.52	6.00	134.62
-0.31	583.47	6.50	110.44
		7.00	95.02

Table A33. Y-axis pressure data measured seven diameters downstream; see figure 32(a)

run 29		run 29 (cont.)	
y-axis position (in.)	pressure (psig)	y-axis position (in.)	pressure (psig)
-8.25	0.005	-2.81	0.282
-7.25	0.005	-2.50	0.331
-6.25	0.011	-2.19	0.387
-5.94	0.016	-1.88	0.434
-5.63	0.026	-1.25	0.553
-5.31	0.039	-0.75	0.624
-5.00	0.054	-0.25	0.627
-4.69	0.073	0.00	0.607
-4.38	0.096	0.16	0.576
-4.06	0.122	0.25	0.560
-3.75	0.151	0.50	0.533
-3.44	0.186	0.75	0.504
-3.13	0.229		

Table A34. Y-axis temperature data measured seven diameters downstream; see figure 32(b)

run 29		run 29 (cont.)	
y-axis position (in.)	temp. (°F)	y-axis position (in.)	temp. (°F)
-8.41	67.10	-2.97	341.59
-7.41	79.38	-2.66	363.16
-6.41	121.56	-2.34	387.96
-6.09	136.42	-2.03	410.10
-5.78	153.45	-1.41	460.17
-5.47	168.66	-0.91	494.57
-5.16	191.63	-0.41	503.67
-4.84	212.27	-0.16	505.53
-4.53	230.63	0.00	497.92
-4.22	251.36	0.09	497.26
-3.91	269.99	0.34	494.89
-3.59	290.70	0.59	483.60
-3.28	314.42		

Table A35. Y-axis pressure data measured eight diameters downstream; see figure 33(a)

run 30		run 30 (cont.)	
y-axis position (in.)	pressure (psig)	y-axis position (in.)	pressure (psig)
-8.25	0.002	-3.56	0.170
-7.94	0.002	-3.25	0.199
-7.63	0.003	-2.94	0.231
-7.31	0.004	-2.63	0.281
-7.00	0.008	-2.31	0.313
-6.69	0.008	-2.00	0.346
-6.38	0.014	-1.69	0.400
-6.06	0.019	-1.38	0.435
-5.75	0.029	-1.06	0.464
-5.44	0.041	-0.75	0.501
-5.13	0.059	-0.44	0.514
-4.81	0.070	-0.13	0.515
-4.50	0.085	0.19	0.499
-4.19	0.115	0.50	0.471
-3.88	0.127	0.75	0.445

Table A36. Y-axis temperature data measured eight diameters downstream; see figure 33(b)

run 30		run 30 (cont.)	
y-axis position (in.)	temp. (°F)	y-axis position (in.)	temp. (°F)
-8.41	78.65	-3.72	277.56
-8.09	82.06	-3.41	295.77
-7.78	89.26	-3.09	313.73
-7.47	98.25	-2.78	340.26
-7.16	113.57	-2.47	351.88
-6.84	116.39	-2.16	363.61
-6.53	130.34	-1.84	383.75
-6.22	141.71	-1.53	402.31
-5.91	158.73	-1.22	411.90
-5.59	179.83	-0.91	424.79
-5.28	193.99	-0.59	439.33
-4.97	206.93	-0.28	439.55
-4.66	218.51	0.03	444.59
-4.34	240.76	0.34	440.65
-4.03	249.64	0.59	434.21

Table A37. Y-axis pressure data measured nine diameters downstream; see figure 34(a)

run 31		run 31 (cont.)	
y-axis position (in.)	pressure (psig)	y-axis position (in.)	pressure (psig)
-10.25	0.002	-3.88	0.157
-9.25	0.001	-3.56	0.189
-8.25	0.001	-3.25	0.216
-7.94	0.002	-2.94	0.245
-7.63	0.003	-2.63	0.280
-7.31	0.005	-2.31	0.309
-7.00	0.015	-2.00	0.349
-6.69	0.014	-1.69	0.373
-6.38	0.025	-1.38	0.404
-6.06	0.041	-1.06	0.424
-5.75	0.045	-0.75	0.438
-5.44	0.062	-0.44	0.427
-5.13	0.071	-0.13	0.413
-4.81	0.091	0.19	0.397
-4.50	0.106	0.50	0.329
-4.19	0.129	0.75	0.313

Table A38. Y-axis temperature data measured nine diameters downstream; see figure 34(b)

run 31		run 31 (cont.)	
y-axis position (in.)	temp. (°F)	y-axis position (in.)	temp. (°F)
-10.41	64.66	-4.03	273.68
-9.41	66.85	-3.72	295.22
-8.41	82.95	-3.41	305.59
-8.09	96.03	-3.09	322.34
-7.78	105.98	-2.78	336.88
-7.47	116.72	-2.47	351.90
-7.16	132.65	-2.16	368.37
-6.84	137.19	-1.84	379.34
-6.53	153.68	-1.53	392.78
-6.22	183.28	-1.22	403.48
-5.91	187.80	-0.91	410.20
-5.59	202.13	-0.59	406.99
-5.28	216.60	-0.28	405.84
-4.97	227.65	0.03	403.56
-4.66	239.01	0.34	379.36
-4.34	254.33	0.59	379.30

Table A39. Y-axis pressure data measured ten diameters downstream; see figure 35(a)

run 32		run 32 (cont.)	
y-axis position (in.)	pressure (psig)	y-axis position (in.)	pressure (psig)
-11.25	0.005	-4.19	0.149
-10.25	0.006	-3.88	0.168
-9.25	0.009	-3.56	0.191
-8.75	0.011	-3.25	0.211
-8.25	0.017	-2.94	0.235
-7.94	0.018	-2.63	0.263
-7.63	0.025	-2.31	0.286
-7.31	0.028	-2.00	0.311
-7.00	0.033	-1.69	0.329
-6.69	0.037	-1.38	0.334
-6.38	0.049	-1.06	0.335
-6.06	0.060	-0.75	0.342
-5.75	0.067	-0.44	0.342
-5.44	0.079	-0.13	0.321
-5.13	0.088	0.19	0.305
-4.81	0.096	0.50	0.278
-4.50	0.120		

Table A40. Y-axis temperature data measured ten diameters downstream; see figure 35(b)

run 32		run 32 (cont.)	
y-axis position (in.)	temp. (°F)	y-axis position (in.)	temp. (°F)
-11.41	91.90	-4.34	273.55
-10.41	103.72	-4.03	283.97
-9.41	114.98	-3.72	297.21
-8.91	126.69	-3.41	303.34
-8.41	140.06	-3.09	313.52
-8.09	145.51	-2.78	328.45
-7.78	155.88	-2.47	337.51
-7.47	161.62	-2.16	347.30
-7.16	171.38	-1.84	352.01
-6.84	179.74	-1.53	356.13
-6.53	191.68	-1.22	356.44
-6.22	204.20	-0.91	357.62
-5.91	212.26	-0.59	360.91
-5.59	223.42	-0.28	354.64
-5.28	233.49	0.03	353.60
-4.97	237.80	0.34	343.43
-4.66	258.92		

Appendix B

Weather Data

Table B1. Weather data for July 12, 1993

Time	Wind Speed mi/hr	Wind Direction deg	Temp. °F	Relative Humidity %	Atmospheric Pressure $lb_f/in.^2$
04:30	1.55	80	59.3	96.1	14.652
05:00	4.25	10	59.1	96.1	14.651
05:30	6.05	68	58	93.9	14.654
06:00	6.05	125	57.2	96.1	14.655
06:30	4.05	120	57.1	96.1	14.656
07:15	4.05	120	57.8	96.1	14.656
Time-Averaged Values	4.59	88	57.9	95.7	14.654

Table B2. Weather data for July 13, 1993

Time	Wind Speed mi/hr	Wind Direction deg	Temp. °F	Relative Humidity %	Atmospheric Pressure $lb_f/in.^2$
11:50	4.50	15	61.1	86.0	14.641
12:45	5.30	101	61.1	86.9	14.639
02:00	3.30	45	60.3	86.4	14.637
02:21	4.25	97	59.7	84.3	14.637
02:40	4.15	91	59.6	84.4	14.637
03:15	4.65	90	58.3	86.7	14.635
03:43	5.35	95	57.9	87.9	14.638
04:30	4.10	91	57.0	89.0	14.638
05:07	4.90	91	56.7	88.7	14.640
05:55	6.25	96	55.9	90.0	14.648
06:08	4.80	93	55.8	90.5	14.650
06:41	5.15	83	55.3	91.5	14.653
07:22	5.10	84	56.0	91.3	14.658
Time-Averaged Values	4.75	83	58.3	87.9	14.642

Table B3. Weather data for July 14, 1993

Time	Wind Speed mi/hr	Wind Direction deg	Temp. °F	Relative Humidity %	Atmospheric Pressure $lb_f/in.^2$
11:20	7.90	20	61.5	74.8	14.686
12:30	4.70	63	60.1	84.0	14.686
01:18	6.65	91	59.1	84.1	14.684
01:46	8.30	91	57.8	87.2	14.684
02:00	8.65	110	57.5	88.1	14.683
02:38	7.65	108	56.8	90.4	14.681
03:35	5.30	108	56.1	91.4	14.684
04:17	4.50	116	55.7	90.5	14.685
04:45	5.40	101	55.4	91.4	14.689
05:23	5.40	105	55.2	91.9	14.695
06:19	4.50	118	55.0	91.1	14.703
07:10	8.90	90	55.6	90.3	14.709
Time-Averaged Values	6.15	94	57.2	88.1	14.689

Table B4. Weather data for July 15, 1993

Time	Wind Speed mi/hr	Wind Direction deg	Temp. °F	Relative Humidity %	Atmospheric Pressure $lb_f/in.^2$
11:54	7.50	245	60.3	75.0	14.703
12:54	5.45	244	61.4	69.5	14.697
02:04	5.45	219	59.2	72.6	14.694
02:33	0.75	201	58.1	75.7	14.693
02:59	4.20	212	58.6	75.3	14.688
03:26	3.75	170	57.3	81.0	14.688
03:56	2.95	144	57.5	85.2	14.689
04:26	4.40	123	57.4	86.1	14.688
05:00	8.75	33	57.1	87.4	14.690
05:29	3.30	75	56.7	89.0	14.692
06:28	3.35	100	57.2	86.3	14.697
07:02	2.85	96	57.5	83.5	14.700
07:30	2.45	76	58.3	81.8	14.705
07:54	0.0		58.7	79.5	14.708
Time-Averaged Values	4.26	154	58.4	80.0	14.695

Table B5. Weather data for July 16, 1993

Time	Wind Speed mi/hr	Wind Direction deg	Temp. °F	Relative Humidity %	Atmospheric Pressure $lb_f/in.^2$
11:05	3.95	32	60.9	83.7	14.692
11:30	5.45	12	60.5	80.9	14.691
12:00	6.30	74	60.2	84.8	14.692
12:30	5.30	13	59.8	87.5	14.689
01:00	3.15	22	59.3	87.9	14.688
01:30	3.25	24	59.3	90.1	14.686
02:00	4.35	39	59.0	90.0	14.683
02:30	2.95	31	59.1	90.3	14.680
03:00	3.80	30	58.7	92.0	14.680
03:30	3.20	36	58.6	92.2	14.676
04:00	4.55	27	58.5	93.4	14.678
04:30	2.95	15	58.2	94.5	14.679
05:00	4.05	22	57.8	96.1	14.679
05:30	4.50	24	57.8	94.6	14.682
06:00	4.90	22	57.3	95.4	14.686
06:30	1.55	18	57.7	92.7	14.688
07:00	0.45	83	57.9	93.2	14.688
07:45	5.35	96	58.7	81.7	14.690
Time-Averaged Values	3.81	34	58.8	90.5	14.685

Appendix C

Infrared Image Data File List

Table C1. Infrared data obtained July 12, 1993

Data Filename	File Size	Description	Time
run0b.swb run0b.lwb	10 frames	Plume against Mylar backdrop	3:40
run0e.swb run0e.lwb	5 frames	Plume against Mylar backdrop	4:13
run1b.swb run1b.lwb	10 frames	Plume against Mylar backdrop	4:51
run1e.swb run1e.lwb	8 frames	Plume against Mylar backdrop	5:24
run2b.swb run2b.lwb	10 frames	Plume against Mylar backdrop	5:29
run2e.swb run2e.lwb	10 frames	Plume against Mylar backdrop	6:04
run3b.swb run3b.lwb	10 frames	Plume against Mylar backdrop	6:05
run3m.swb run3m.lwb	10 frames	Probe shown in the flow	6:38
run3e.swb run3e.lwb	7 frames	Plume against Mylar backdrop	6:48

Table C2. Infrared data obtained July 13, 1993

Data Filename	File Size	Description	Time
clear.swb clear.lwb	5 frames	Mylar backdrop without plume	2:20 a.m.
spect1.swb spect1.lwb	6 frames	Plume against Mylar backdrop	2:06 a.m.
spect2.swb spect2.lwb	6 frames	Plume against Mylar backdrop	2:12 a.m.
spect3.swb spect3.lwb	6 frames	Plume against Mylar backdrop	2:38 a.m.
clear0.swb clear0.lwb	6 frames	Mylar backdrop without plume	2:56 a.m.
spect4.swb spect4.lwb	6 frames	Plume against Mylar backdrop	3:12 a.m.
clear3.swb clear3.lwb	6 frames	Mylar backdrop without plume	3:32 a.m.
spect5.swb spect5.lwb	6 frames	Plume against Mylar backdrop	3:40 a.m.
clear4.swb clear4.lwb	6 frames	Mylar backdrop without plume	4:01 a.m.
spect6.swb spect6.lwb	6 frames	Plume against Mylar backdrop	4:11 a.m.
spect7.swb spect7.lwb	6 frames	Plume against Mylar backdrop	4:27 a.m.
clear5.swb clear5.lwb	6 frames	Mylar backdrop without plume	4:34 a.m.
spect8.swb spect8.lwb	6 frames	Plume against Mylar backdrop	4:52 a.m.
clear6.swb clear6.lwb	6 frames	Mylar backdrop without plume	5:06 a.m.
spect9.swb spect9.lwb	6 frames	Plume against Mylar backdrop	5:10 a.m.
clear7.swb clear7.lwb	6 frames	Mylar backdrop without plume	5:17 a.m.

Table C3. Infrared data obtained July 14, 1993

Data Filename	File Size	Description	Time
clear0.swb clear0.lwb	6 frames	Mylar backdrop without plume	12:45 a.m.
run4.swb run4.lwb	6 frames	Plume against Mylar backdrop	1:18 a.m.
run5.swb run5.lwb	6 frames	Plume against Mylar backdrop	1:47 a.m.
run6.swb run6.lwb	6 frames	Plume against Mylar backdrop	2:17 a.m.
run7.swb run7.lwb	6 frames	Plume against Mylar backdrop	2:51 a.m.
run7m.swb run7m.lwb	6 frames	Plume against Mylar backdrop	3:25 a.m.
run8.swb run8.lwb	6 frames	Plume against Mylar backdrop	3:27 a.m.
run9.swb run9.lwb	6 frames	Plume against Mylar backdrop	4:06 a.m.
run9b.swb run9b.lwb	6 frames	Plume against Mylar backdrop	4:19 a.m.
run10.swb run10.lwb	6 frames	Plume against Mylar backdrop	5:00 a.m.
run11.swb run11.lwb	6 frames	Plume against Mylar backdrop	5:31 a.m.
run11b.swb run11b.lwb	6 frames	Plume against Mylar backdrop	5:48 a.m.
run11m.swb run11m.lwb	6 frames	Plume and Survey Probe	6:12 a.m.
run12.swb run12.lwb	6 frames	Plume against Mylar backdrop	6:14 a.m.
run13.swb run13.lwb	6 frames	Plume against Mylar backdrop	6:41 a.m.

Table C4. Infrared data obtained July 15, 1993

Data Filename	File Size	Description	Time
clear0.swb clear0.lwb	6 frames	Mylar backdrop without plume	1:06 a.m.
run14.swb run14.lwb	6 frames	Plume against Mylar backdrop	2:02 a.m.
run15.swb run15.lwb	6 frames	Plume against Mylar backdrop	2:35 a.m.
run16.swb run16.lwb	6 frames	Plume against Mylar backdrop	2:57 a.m.
run22.swb run22.lwb	5 frames	Plume against Mylar backdrop	3:28 a.m.
run 22h.swb run22h.lwb	6 frames	Plume above Mylar backdrop	3:29 a.m.
run23.swb run23.lwb	5 frames	Plume against Mylar backdrop	3:57 a.m.
run23h.swb run23h.lwb	6 frames	Plume against Mylar backdrop	3:58 a.m.
run24.swb run24.lwb	6 frames	Plume against Mylar backdrop	4:26 a.m.
run25.swb run25.lwb	6 frames	Plume against Mylar backdrop	4:59 a.m.
run25h.swb run25h.lwb	6 frames	Plume above Mylar backdrop	4:59 a.m.
run17.swb run17.lwb	6 frames	Plume against Mylar backdrop	5:39 a.m.
run18.swb run18.lwb	6 frames	Plume against Mylar backdrop	6:09 a.m.
run19.swb run19.lwb	6 frames	Plume against Mylar backdrop	6:44 a.m.

Table C5. Infrared data obtained July 16, 1993

Data Filename	File Size	Description	Time
clear0.swb clear0.lwb	6 frames	Mylar backdrop without plume	12:59 a.m.
noshield.swb noshield.lwb	6 frames	Plume with no foreground shield	1:02 a.m.
shield.swb shield.lwb	6 frames	Plume with foreground shield	1:31 a.m.
run26.swb run26.lwb	6 frames	Plume against Mylar backdrop	1:38 a.m.
run27.swb run27.lwb	6 frames	Plume against Mylar backdrop	2:23 a.m.
run28.swb run28.lwb	6 frames	Plume against Mylar backdrop	3:29 a.m.
run29.swb run29.lwb	6 frames	Plume against Mylar backdrop	4:02 a.m.
run30.swb run30.lwb	6 frames	Plume against Mylar backdrop	4:26 a.m.
run31.swb run31.lwb	6 frames	Plume against Mylar backdrop	5:05 a.m.
run32.swb run32.lwb	6 frames	Plume against Mylar backdrop	5:50 a.m.
run33.swb run33.lwb	6 frames	Plume against Mylar backdrop	6:27 a.m.
clear45.swb clear45.lwb	6 frames	Cameras and Mylar backdrop rotated 45° without plume	7:25 a.m.
set45.swb set45.lwb	6 frames	Cameras and Mylar backdrop rotated 45° with plume	7:29 a.m.

References

1. Buning, P. G.; Chiu, I. T.; Obayshi, S.; Rizk, Y. M.; and Steger, J. L.: Numerical Simulation of the Integrated Space Shuttle Vehicle in Ascent, AIAA Paper 88-4359CP, AIAA Atmospheric Flight Mechanics Conference, Minneapolis, Minnesota, August 15–17, 1988.

2. Atwood, C. A.; and Van Dalsem, W. R.: Flowfield Simulation About the SOFIA Airborne Observatory, AIAA Paper 92-0656, AIAA 30th Aerospace Sciences Meeting and Exhibit, Reno, Nevada, January 6–9, 1992.

3. Smith, M. H.; Van Dalsem, W. R.; Chawla, K.; and Dougherty, F. C.: Numerical Simulation of a Complete STOVL Aircraft in Ground Effect, AIAA Paper 91-3293, AIAA 9th Applied Aerodynamics Conference, Baltimore, Maryland, September 23–25, 1991.

4. Lambert, M.: Editor in Chief, Jane's All the World's Aircraft 1993–94, Jane's Information Group Limited, Coulsdon, Surry, UK.

5. Milford, C. M.: Hot Gas Recirculation in V/STOL, SAE Paper 872036, International Powered Lift Conference and Exposition, Santa Clara, California, December 7–10, 1987.

6. Stewart, V. R.; and Kuhn, R. E.: A Method for Estimating the Propulsion Induced Aerodynamic Characteristics of STOL Aircraft in Ground Effect, NADC-80226-60, August 1983.

7. Kuhn, R. E.: Hover Suckdown and Fountain Effects, SAE Paper 872305, International Powered Lift Conference and Exposition, Santa Clara, California, December 7–10, 1987.

8. Anon.: Triple-Threat Combat Jet, Popular Mechanics, March 1994, p. 24.

9. Wilson, S. B., III: A NASA Study of the Impact of Technology on Future Carrier Based Tactical Aircraft – Overview, AIAA Paper 92-4211, AIAA Aircraft Design Systems Meeting, Hilton Head, South Carolina, August 24–26, 1992.

10. Wardwell, D. A.; and Kuhn, R. E.: Prediction Techniques for Jet-Induced Effects in Hover on STOVL Aircraft, NASA TM-102818, August 1991.

11. Hange, C. E.; and Wardwell, D. A.: Small Scale Jet Effects and Hot Gas Ingestion Investigations at NASA Ames, AIAA Paper 92-4252, AIAA Aircraft Design Systems Meeting, Hilton Head, South Carolina, August 24–26, 1992.

12. Naumowicz, T.; and Smith, B. E.: Hover Performance Validation of an Ejector Configured STOVL Fighter Aircraft, AIAA Paper 92-4255, AIAA Aircraft Design Systems Meeting, Hilton Head, South Carolina, August 24–26, 1992.

13. Chawla, K.; Van Dalsem, W. R.; and Rao, K. V.: Simulation and Analysis of a Delta Planform with Multiple Jets in Ground Effect, AIAA Paper 90-0299, 28th Aerospace Sciences Meeting, Reno, Navada, January 8–11, 1990.

14. Chawla, K.; and Van Dalsem, W. R.: Numerical Simulation of STOL Operations Using Thrust-Vectoring, AIAA Paper 92-4254, AIAA Aircraft Design Systems Meeting, Hilton Head, South Carolina, August 24–26, 1992.

15. Engelland, S. A.; Franklin, J. A.; Stortz, M. W.; and Hardy, G. H.: Piloted Simulation Evaluation of Pitch Control Designs for Highly Augmented STOVL Aircraft, AIAA Paper 92-4234, AIAA Aircraft Design Systems Meeting, Hilton Head, South Carolina, August 24–26, 1992.

16. Birckelbaw, L. G.; and Corliss, L. D.: Piloted Simulation Study of Two Tilt-Wing Control Concepts, AIAA Paper 92-4236, AIAA Aircraft Design Systems Meeting, Hilton Head, South Carolina, August 24–26, 1992.

17. Anon.: Burst Recording Unit, Introduction Manual, Reference Manual, Version 3.1, Agema Infrared Systems, Danderyd, Sweden, September 1990.

18. Martin, B.: Sales Representative, Agema Infrared Systems Inc., 550 County Avenue, Secaucus, NJ 07094-2607.

19. Birckelbaw, L. D.; and Nelson, E. L.: Infrared Flow Visualization of V/STOL Aircraft, AIAA Paper 92-4253, AIAA, Aircraft Design Systems Meeting, Hilton Head, South Carolina, August 24–26, 1992.

20. Hardman, R. R.: Infrared Imaging: A Proposed Validation Technique for Computational Fluid Dynamics Codes Used in STOVL Applications, M.S. Thesis, Department of Mechanical Engineering, Virginia Polytechnic Institute and State University, Blacksburg, Virginia, May 1990.

21. Hardman, R. R.; Smith, M. H.; Gelhausen, P. A.; Van Dalsem, W. R.: and, Mahan, J. R.: Infrared Imaging: A Validation Technique for Computational Fluid Dynamics Codes Used in STOVL Applications, AIAA Paper 91-0675, 29th Aerospace Sciences Meeting, Reno, Nevada, January 7–10, 1991.

22. Nelson, E. L.: Development of an Infrared Gaseous Radiation Band Model Based on NASA SP-3080 for Computational Fluid Dynamic Code Validation Applications, M.S. Thesis, Department of Mechanical Engineering, Virginia Polytechnic Institute and State University, Blacksburg, Virginia, August 1992.

23. Nelson, E. L.; Mahan, J. R.; Turk, J. A.; Hardman, R. R.; Birckelbaw, L. D.; and Gelhausen, P. A.: Infrared Characterization of Jet Engine Exhaust Plumes, Characterization, Propagation, and Simulation of Sources and Backgrounds III, Wendell R. Watkins and Dieter Clement, Eds., Proc. SPIE 1967, 1993, pp. 411–418.

24. Nelson, E. L.; Mahan, J. R.; Turk, J. A.; Birckelbaw, L. D.; Wardwell, D. A.; and Hange, C. H.: Infrared Image Prediction of a Heated Exhaust Flow, Characterization, Propagation, and Simulation of Sources and Backgrounds IV, Wendell R. Watkins and Dieter Clement, Eds., Proc. SPIE 1967, 1994. [Also published in: 3rd JANNAF SPIRITS User Group Meeting, Sunnyvale, California, October 17–21, 1994.]

25. Turk, J. A.: Acceleration Techniques for the Radiative Analysis of General Computational Fluid Dynamic Solutions Using Reverse Monte Carlo Ray Tracing, Ph.D. Dissertation, Department of Aerospace Engineering, Virginia Polytechnic Institute and State University, Blacksburg, Virginia, November 1994.

26. Vanderbilt, D.; and Slack, M.: A Model for Emission and Scattering of Infrared Radiation from Combustion Gases and Particles, Grumman Research Department Memorandum, RM-621, June 1976.

27. Kim, S. J.; and Caldwell, J.: Real Line Strength Distributions for Random Band Models, Journal of Quantitative Spectroscopy and Radiant Transfer, vol 29, no. 2, 1983, pp. 151–156.

28. Pierluissi, J. H.; and Maragaoudakis, C. E.: Molecular Transmittance Band Model for Oxygen in the Infrared, Applied Optics, vol. 25, no. 10, 1986, pp. 1538–1540.

29. Drakes, J.; Hiers, R.; and Reed, R.: Doppler Shift Effects on Infrared Band Model Calculations, AIAA Paper 89-1678, 24th Thermophysics Conference, Buffalo, New York, June 12–14, 1989.

30. Felske, J. D.; and Tien, C. L.: Wide Band Characterization of the Total Band Absorptance of Overlapping Infrared Gas Bands, Combustion Science and Technology, vol. 11, 1975, pp. 111–117.

31. Kneizys, F. X.; Anderson, G. P.; Shettle, E. P.; Gallery, W. O.; Abreu, L. W.; Selby, J. E. A.; Chetwynd, J. H.; and Clough, S. A.: Users Guide to LOWTRAN 7, Air Force Geophysics Laboratory Paper, AFGL-TR-88-0177, August 1988.

32. Baars, J.: NIRATAM Users Manual, Version 2.1, SHAPE Technical Centre, The Hague, The Netherlands, July 23, 1991.

33. Mahan, J. R.; Stern, C. H.; Nelson, E. L.; Turk, J. A.; and Villeneuve, P. V.: LOIR Programmers' Manual, General Electric Aircraft Engines, Aircraft Survivability Technology. The Mechanical Engineering Department, Virginia Polytechnic Institute and State University, Blacksburg, VA, Prepared under NASA Ames Grant NAG 2-664, October 1991.

34. Ludwig, C. B.; Malkmus, W.; Reardon, J. E.; and Thomson, J. A. L.: Handbook of Infrared Radiation from Combustion Gases, Prepared by: Marshall Space Flight Center, National Aeronautics and Space Administration Special Publication, NASA SP-3080, 1973.

35. Naumowicz, Tim, civil servant at NASA Ames Research Center: personal communication, June 1993.

36. Wardwell, Doug, civil servant at NASA Ames Research Center: personal communication, April 1993.

37. Anon.: 8300 Series Stepping Motor Controller/ Driver, 8311,8312, 8313, 8314, User's Guide, Velmex, Inc., East Bloomfield, NY 14443, January 1985.

38. Anon.: LM-HPIB Motor Controller, L-1003, NAS2-11036, Shaw Engineering Martinez, California, April 30, 1982.

39. Anon.: Model Specification, FAA Category II, Class B Gas Turbine Auxiliary Power Unit Airesearch Model GTCG30-142C Part 380946-1, Report No. SC-5899, Airesearch Manufacturing Company of Arizona, April 4, 1969.

40. Anon.: GPU-400/600 Solid State 28.5 Volt DC Ground Power Units, Sales Brochure, Hobart Ground Power Equipment, Troy, Ohio, 1994.

41. Smith, Maxwell: Aviation Fuels, G.T. Foulis and Co. Ltd., Henley-on-Thames, Oxfordshire, Great Britain, 1970.

42. Measurement of Fluid Flow in Pipes Using Orifice, Nozzle, and Venturi, American Society of Mechanical Engineers Standard, ASME MFC-3M-1985.

43. Anon.: Flow Sensor Products, Variations of the Basic Pitot-Static Probe and Special Designs, United Electric Controls Co., Flow Sensor Products, Watertown, Massachusetts, 1994.

44. Anon.: Omega Complete Temperature Measurement Handbook and Encyclopedia, vol. 28, Omega Engineering Inc., Stamford, Connecticut, 1992.

45. Anon.: IEEE 488 and VXIbus Control, Data Acquisition, and Analysis, 1994, National Instruments Corporation, Austin, Texas, 1993.

46. Anon.: Data Acquisition, Quality, Innovation, Performance, Sales Brochure for the PC/XT/AT/EISA, PS/2 Micro Channel, and Mackintosh NuBus, National Instruments Corporation, Austin, Texas, 1993.

47. Anon.: Microsoft Excel, User's Guide 1, Gateway 2000 Edition, Microsoft Corporation, United States of America, 1992.

48. Ahrens, C. Donald: Meteorology Today, an Introduction to Weather, Climate, and the Environment, West Publishing Company, St. Paul, Minnesota, 1991.

49. Wolfe, William, L.; and Zissis, George, J., Eds.: The Infrared Handbook, The Infrared Information and Analysis Center, Environmental Research Institute of Michigan, prepared for: The Office of Naval Research, Department of the Navy, Washington, D.C., 1978.

50. Tap Plastics Inc., 2006 Castro St., Mountain View, CA 94036.

51. Rosato, Dominick, V.: Rosato's Plastics Encyclopedia and Dictionary, Hanser Publishing Co., New York, 1993.

52. Anon.: Midac Air Monitoring System Specifications, Sales Brochure, Midac Corporation, Costa Mesa, California, 1994.

53. Bennett, Charles, scientist employed by Lawrence Livermore National Laboratory: personal communication, June 1993.

54. Birckelbaw, Larry, civil servant at NASA Ames Research Center: personal communication, November 1993.

55. Hossain, M. S.; and Rodi, W.: A Turbulence Model for Buoyant Flows and Its Application to Vertical Buoyant Jets, Journal of Heat and Mass Transfer, The Science and Applications of Heat and Mass Transfer, vol. 6, Pergamon Press Ind., Elmsford, New York, 1982.

56. Chen, J. C.; and Rodi, W.: Turbulent Buoyant Jets – A review of Experimental Data, Journal of Heat and Mass Transfer, The Science and Application of Heat and Mass Transfer, vol. 4, Pergamon Press Inc., Elmsford, New York, 1980.

57. Bejan, A.: Convection Heat Transfer, John Wiley and Sons, 1984.

58. Sideix, M. M.: Infrared Focal Plane Arrays, Application and System Design, Focal Play Arrays: Technology and Application (1987), Jean-Pierre Chatard, Ed., Proc. SPIE 865, 1987, pp. 17–20.

59. Villani, T. S.; Esposito, B. J.; Pletcher, T. J.; Sauer, D. J.; Levine, P. A.; Shallcross, F. V.; Merray, G. M.; and Tower, J. R.: Performance of Generation III 640 x 480 PtSi MOS Array, Infrared Detectors and Focal Plane Arrays III, Eustace L. Dereniak and Robert E. Sampson, Eds., Proc. SPIE 2225, 1994, pp. 2–10.

60. Varney, G. E.; Loftus, T. A.; Crabtree, G.; and Boland, J.: High Fidelity IR Prediction Model, LOIR, for Propulsion Subsystems at GE Aircraft Engines, presented at: 3rd JANNAF SPIRITS User Group Meeting, Lockheed Missiles and Space Company, Sunnyvale, California, October 17–21, 1994.

61. Nielson, G. M.: Scattered Data Modeling, IEEE Computer Graphics and Applications, vol. 13, no. 1, 1993, pp. 60–70.

62. Dinger, A. S.; Dunham, E. W.; Erickson, E. F.; Klotz, D.; and Yee, R.: Evaluation of Jet-Exhaust Scattering for the Aft Telescope Configuration on SOFIA, Internal Report, NASA Ames Research Center, 1992.

63. Stephens, S. E.: Evaluation of Air Injection in a Sudden Expansion Diffuser for Real-Time Afterburning Applications, AEDC TR90-29, 1991.

64. Anon.: Indigo2 Workstation Owner's Guide, Document Number 007-9096010, Silicon Graphics, Inc., Mountain, View, California, 1993.

65. Nelson, E. L.; and Mahan, J. R.: Temperature, Pressure, and Infrared Image Survey of an Axisymmetric Heated Exhaust Plume, to be published as a NASA Technical Memorandum.

66. Nelson, E. L.; and Mahan, J. R.: Temperature, Pressure, and Infrared Image Survey of a Rectangular Heated Exhaust Plume, to be published as a NASA Technical Memorandum.

Table 1. Preliminary experiment data from May 14–15, 1993

Traverse	Data Plane	Data Filename	Comment
Exit Plane Data			
y-axis	x = 0.0, z = 0.15	prelim. run 1	negative y-axis
y-axis	x = 0.0, z = 0.15	prelim. run 2	repeat run
0.5 Diameters Downstream			
y-axis	x = 0.0, z = 2.5	prelim. run 3	negative y-axis
y-axis	x = 0.0, z = 2.5	prelim. run 4	repeat run
y-axis	x = 0.0, z = 2.5	prelim. run 5	repeat run
y-axis	x = 0.0, z = 2.5	prelim. run 6	repeat run
y-axis	x = 0.0, z = 2.5	prelim. run 7	repeat run
1.0 Diameters Downstream			
y-axis	x = 0.0, z = 4.5	prelim. run 8	negative y-axis
y-axis	y = 2.25, z = 4.5	prelim. run 9	positive x-axis
2.0 Diameters Downstream			
x-axis	y = 2.25, z = 4.5	prelim. run 10	negative y-axis
3.0 Diameters Downstream			
y-axis	x = 0.0, z = 13.5	prelim. run 11	negative y-axis
4.0 Diameters Downstream			
y-axis	x = 0.0, z = 18.0	prelim. run 12	negative y-axis
5.0 Diameters Downstream			
y-axis	x = 0.0, z = 22.5	prelim. run 13	negative y-axis
z-axis sweep to 2.2 Diameters			
z-axis	x = 0.0, y = 2.25	prelim. run 14	

Table 2. APU data measured from the exit plane through three diameters downstream (these data obtained July 12–16, 1993)

Traverse	Data Plane	Data Filename	Comment
Exit Plane Data			
y-axis	x = 0.0, z = 0.15	run 1	negative y-axis
y-axis	x = 0.0, z = 0.15	run 2	repeat run
x-axis	y = 0.0, z = 0.15	run 3	complete x-axis
x-axis	y = 0.0, z = 0.15	run 4	positive x-axis
0.5 Diameters Downstream			
y-axis	x = 0.0, z = 2.25	run 5	negative y-axis
y-axis	x = 0.0, z = 2.25	run 6	repeat run
x-axis	y = 0.0, z = 2.25	run 7	complete x-axis
x-axis	y = 0.0, z = 2.25	run 8	positive x-axis
1.0 Diameters Downstream			
y-axis	x = 0.0, z = 4.5	run 9	negative y-axis
y-axis	x = 0.0, z = 4.5	run 10	repeat run
x-axis	x = 0.0, z = 4.5	run 11	complete x-axis
x-axis	x = 0.0, z = 4.5	run 12	positive x-axis
2.0 Diameters Downstream			
y-axis	x = 0.0, z = 9.0	run 13	negative y-axis
y-axis	x = 0.0, z = 9.0	run 14	repeat run
x-axis	x = 0.0, z = 9.0	run 15	complete x-axis
x-axis	x = 0.0, z = 9.0	run 16	positive x-axis
3.0 Diameters Downstream			
y-axis	x = 0.0, z = 13.5	run 17	negative y-axis
y-axis	x = 0.0, z = 13.5	run 18	repeat run

Table 3. APU data measured from three diameters downstream through ten diameters downstream (these data obtained July 12–16, 1993)

Traverse	Data Plane	Data Filename	Comment
3.0 Diameters Downstream (cont.)			
x-axis	x = 0.0, z = 13.5	run 19	complete x-axis
4.0 Diameters Downstream			
y-axis	x = 0.0, z = 18.0	run 20	negative y-axis
y-axis	x = 0.0, z = 18.0	run 21	repeat run
x-axis	x = 0.0, z = 18.0	run 22	complete
5.0 Diameters Downstream			
y-axis	x = 0.0, z = 22.5	run 23	negative y-axis
y-axis	x = 0.0, z = 22.5	run 24	repeat run
x-axis	x = 0.0, z = 22.5	run 25	complete x-axis
6.0 Diameters Downstream			
y-axis	x = 0.0, z = 27.0	run 26	negative y-axis
y-axis	x = 0.0, z = 27.0	run 27	repeat run
x-axis	x = 0.0, z = 27.0	run 28	complete x-axis
7.0 Diameters Downstream			
y-axis	x = 0.0, z = 31.5	run 29	negative y-axis
8.0 Diameters Downstream			
y-axis	x = 0.0, z = 36.0	run 30	negative y-axis
9.0 Diameters Downstream			
y-axis	x = 0.0, z = 40.5	run 31	negative y-axis
10.0 Diameters Downstream			
y-axis	x = 0.0, z = 45.0	run 32	negative y-axis

Table 4. Results from calibration of the Kiel probe

Pressure maintained by the calibration unit (psig)	Pressure measured by the kiel Probe (psig)	Difference between measured data and calibration unit data (%)
0.000	-0.0004	
0.100	0.0986	-1.40
0.199	0.1986	-0.20
0.300	0.2992	-0.27
0.399	0.3985	-0.125
0.500	0.5016	0.320
0.599	0.5994	0.067
0.700	0.7028	0.400
0.800	0.8036	0.450
0.900	0.9074	0.822
1.000	1.0034	0.340
1.100	1.1047	0.427
1.200	1.2049	0.408

Table 5. Results from the Midac Spectrometer

Data Set No.	Probe Temp. °F	Fit Temp °F	Average °F	Stand. dev. °F
1	680	729	725	31
2	680	763	-	-
3	680	719	-	-
4	680	688	-	-
5	669	702	719	24
6	669	736	-	-
7	540	632	637	7
8	550	642	-	-
9	410	bad	-	-
10	410	660	-	-

Note: The "-" indicates that these calculations were not performed.

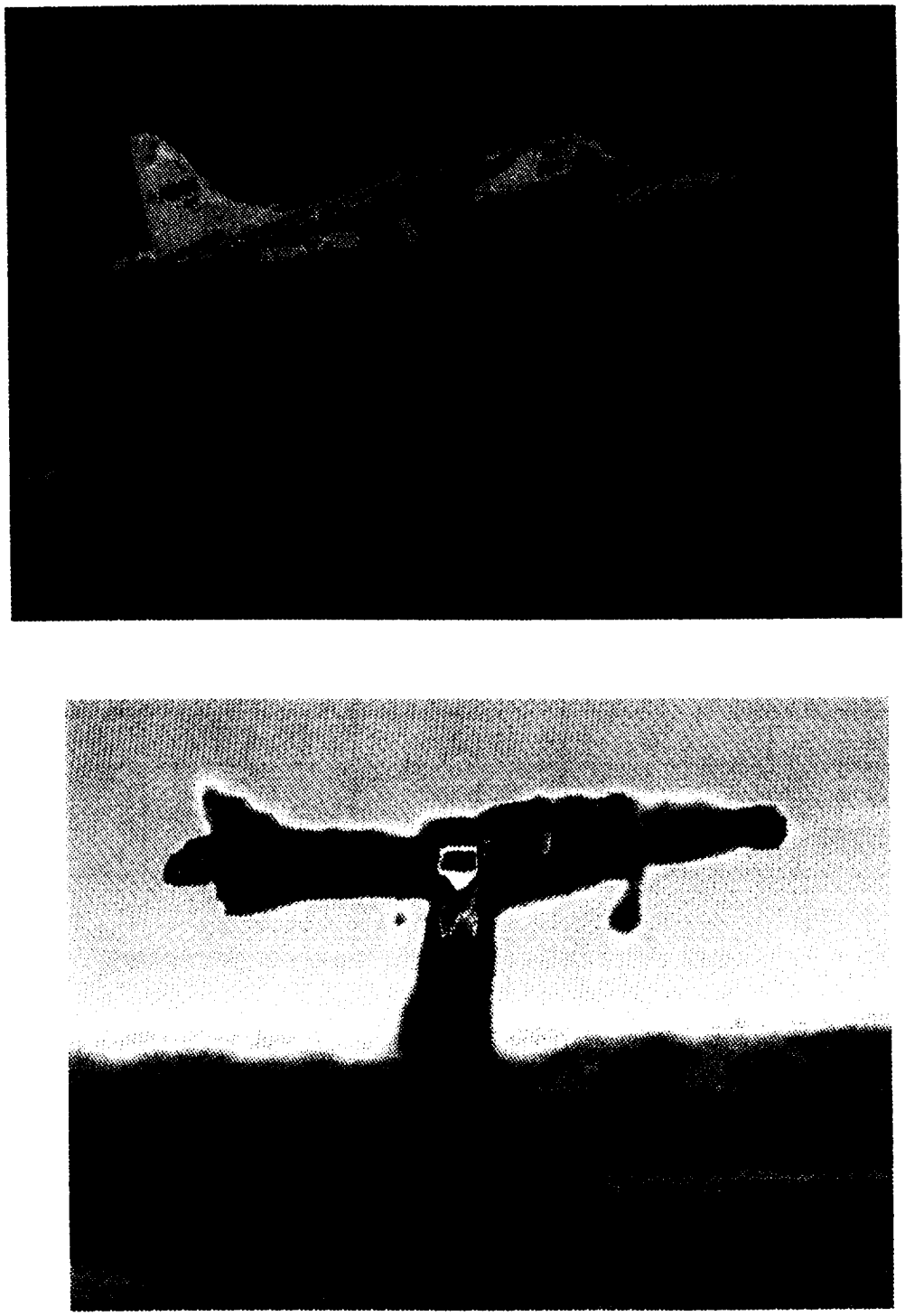

Figure 1. (a) Photograph of the McDonnell Douglas Harrier YAV-8B, and (b) MWB infrared image of the Harrier in a 30-ft (9.14-m) altitude and 30-kt (15.4-m/s) velocity flight condition.

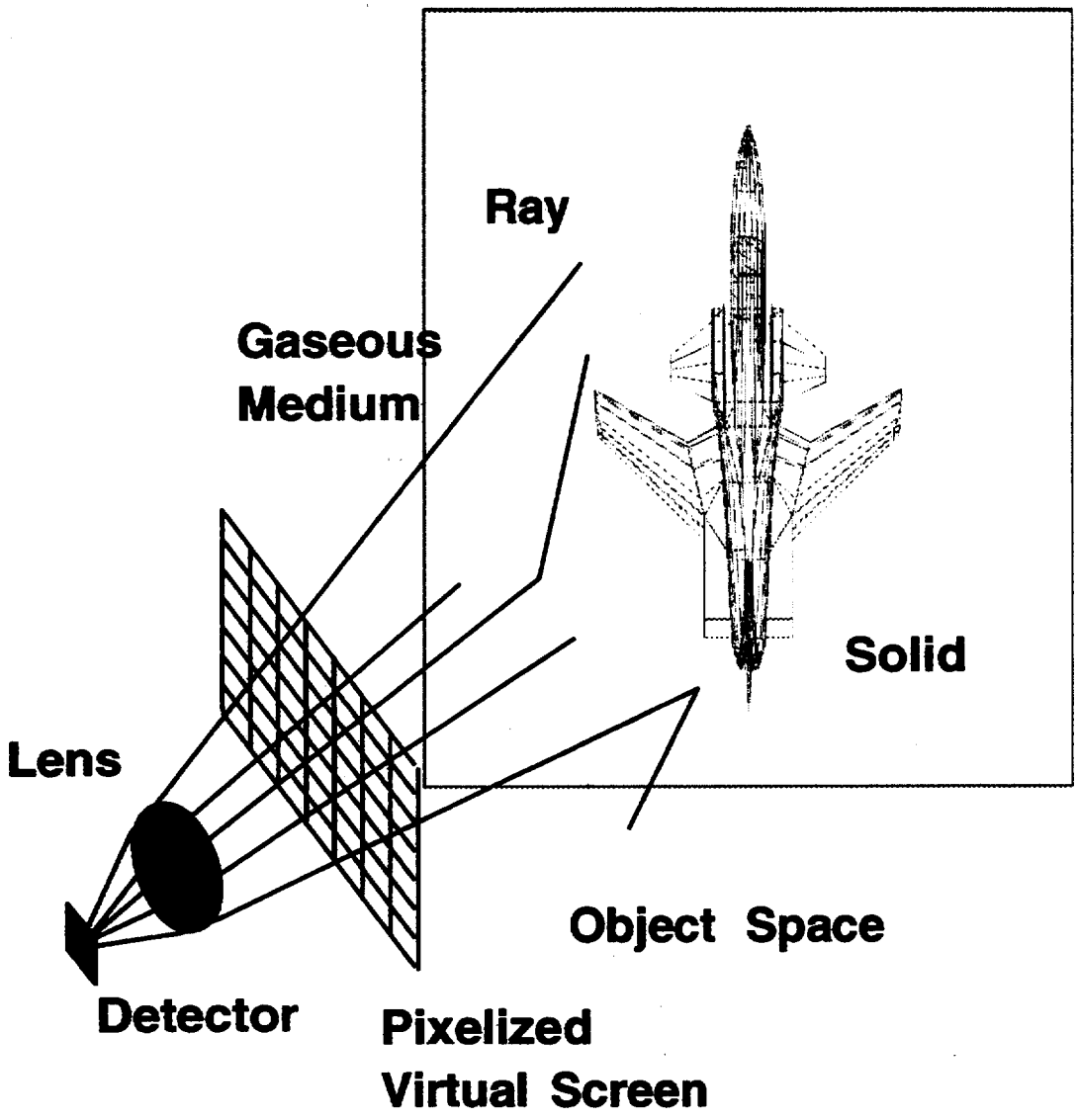

Figure 2. Schematic diagram illustrating how the Monte Carlo ray-trace algorithm works.

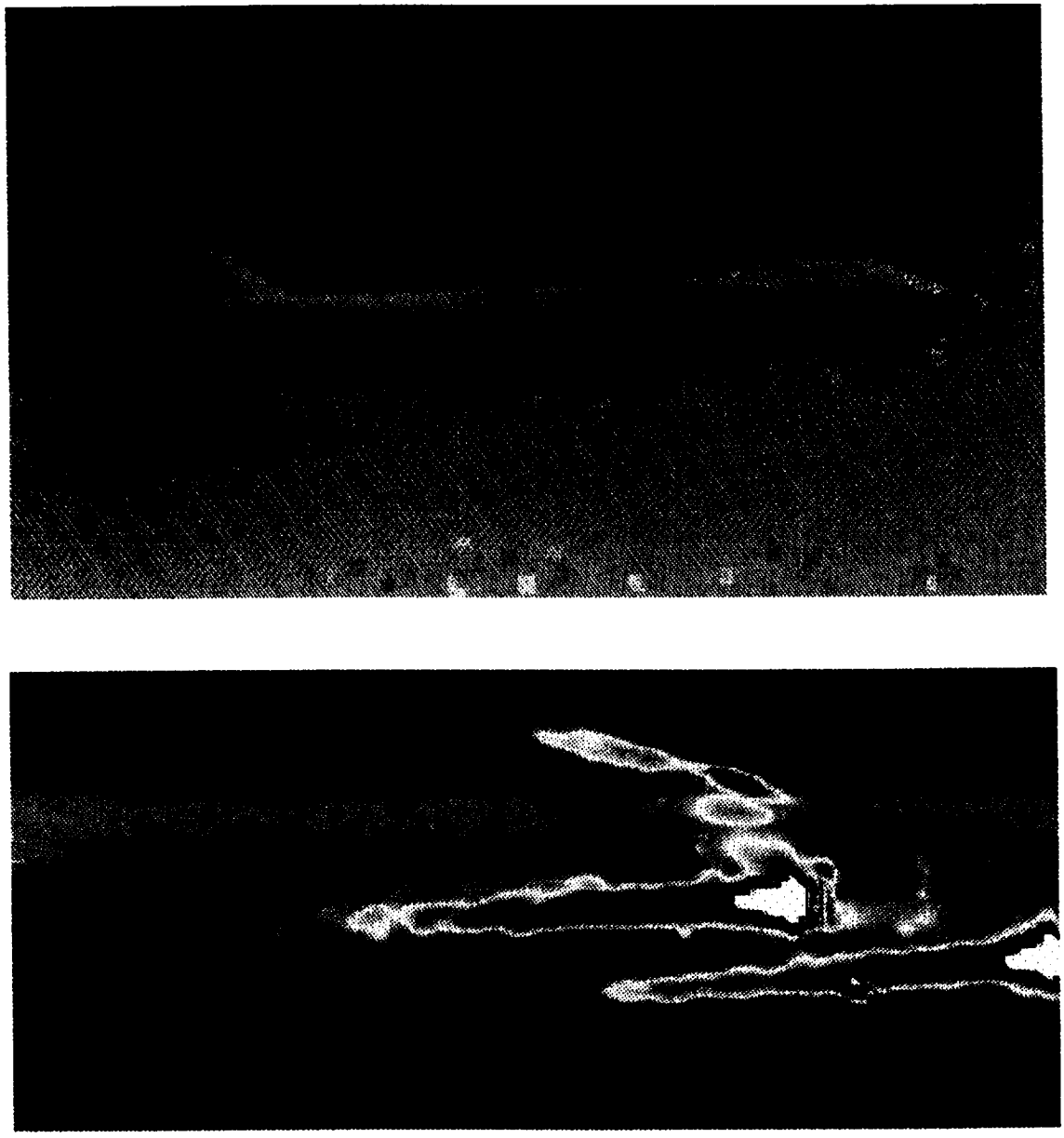

Figure 3. (a) Photograph of the Boeing 747 Space Shuttle Carrier Aircraft, and (b) MWB infrared image of the Boeing 747.

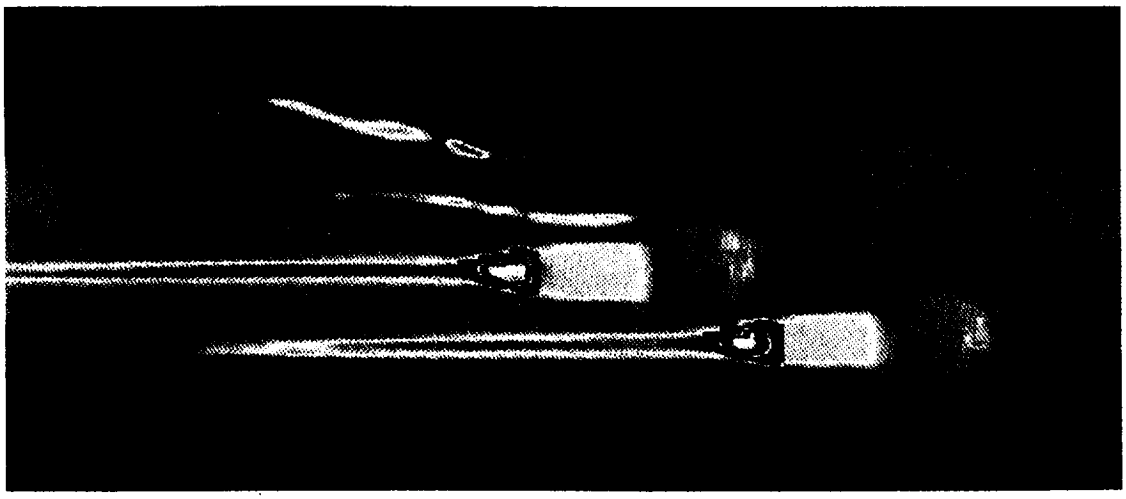

Figure 4. Predicted infrared spectral image at 4.3 μm of the Boeing747 Space Shuttle Carrier Aircraft.

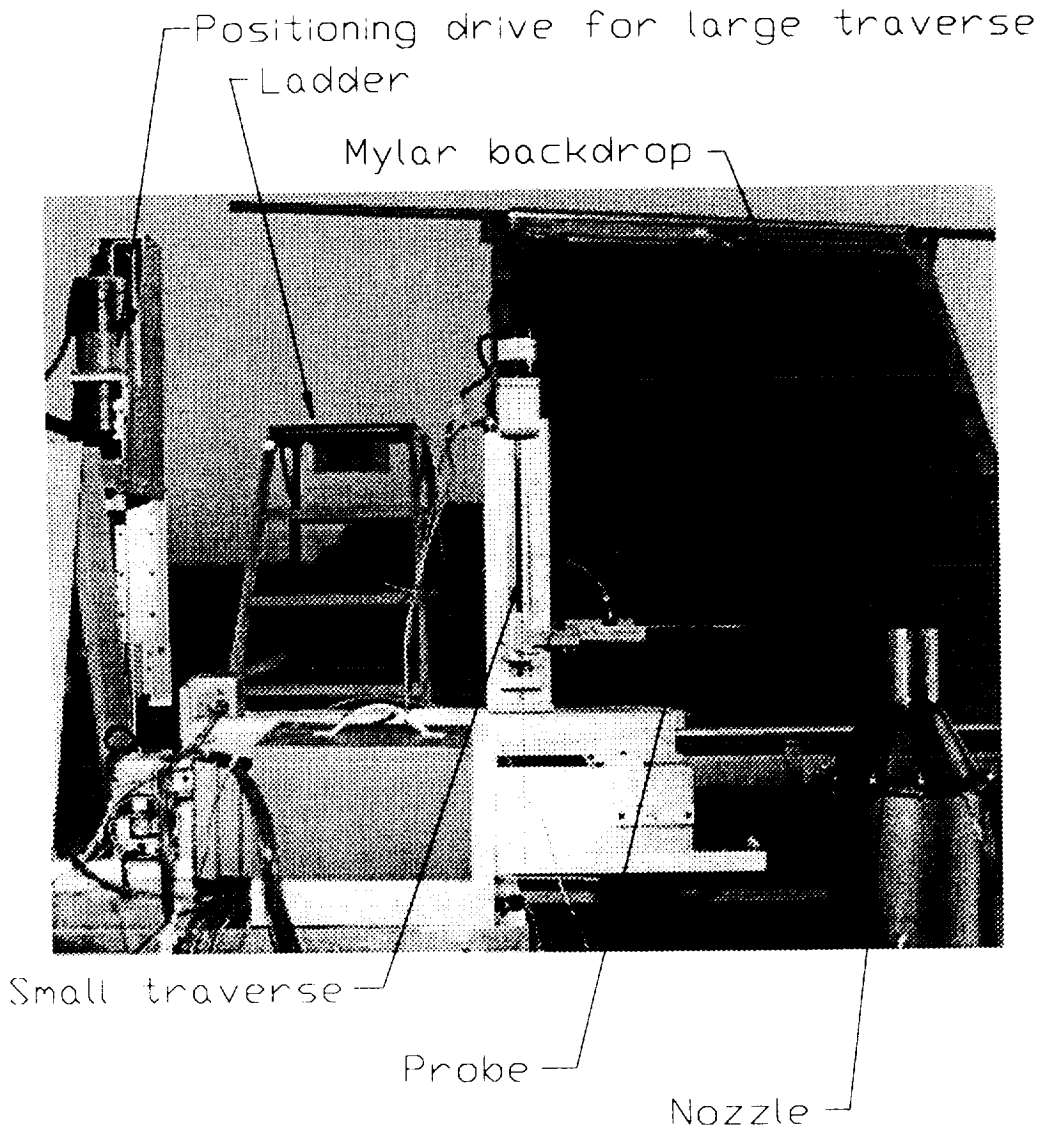

Figure 5. Photograph of the experimental equipment taken during the APU test at the OARF.

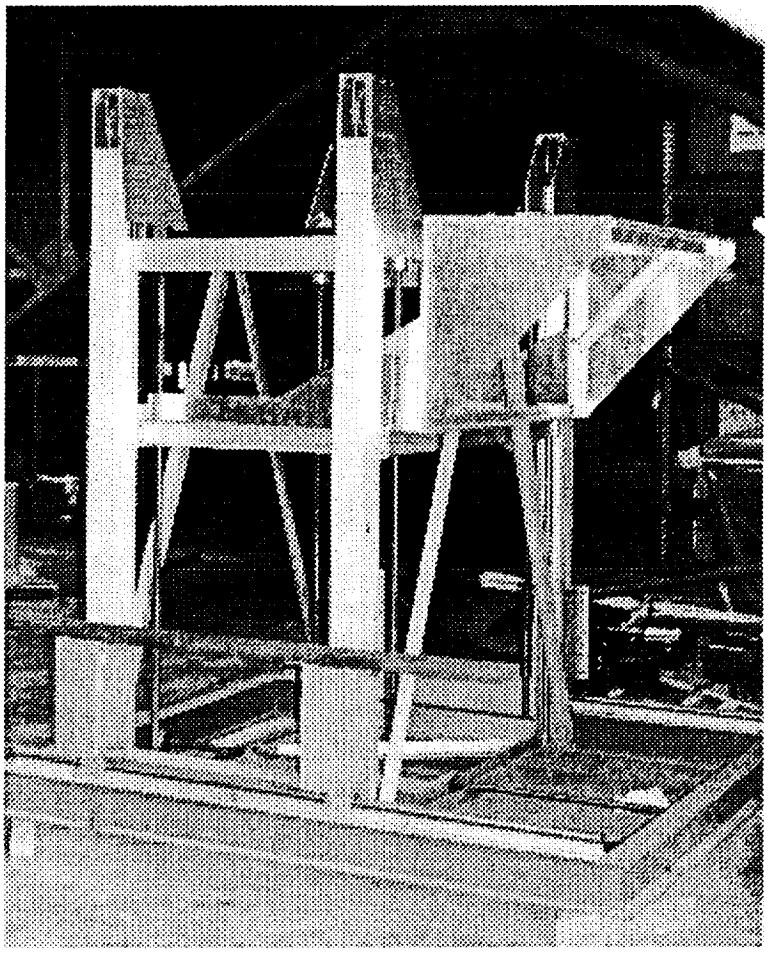

Figure 6. The large two-dimensional traverse used during the APU experiment at the OARF.

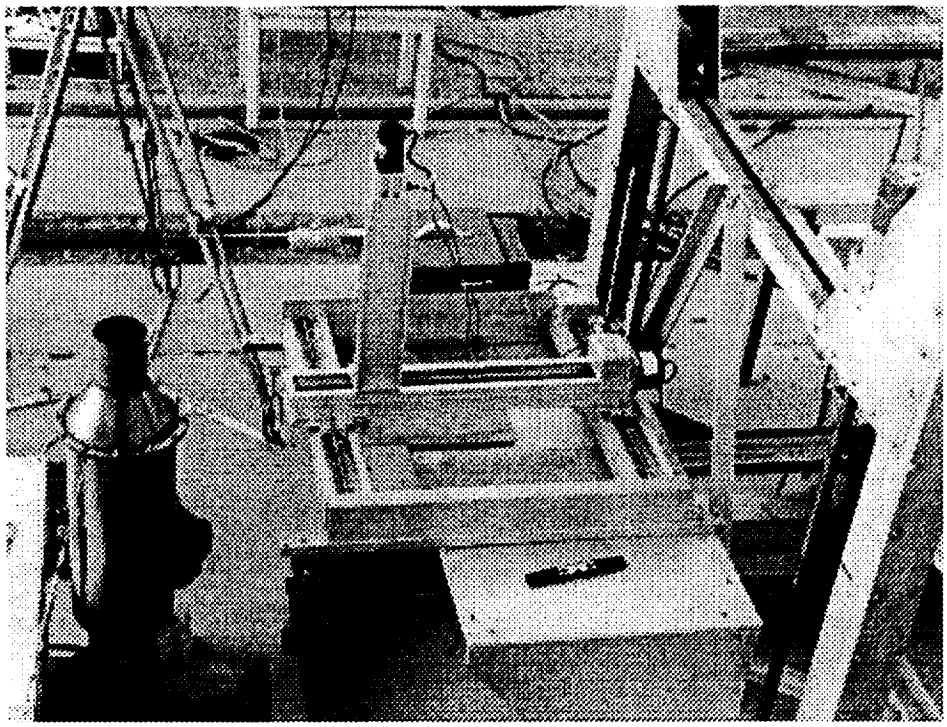

Figure 7. The small three-dimensional traverse rig shown attached to the larger two-dimensional traverse rig.

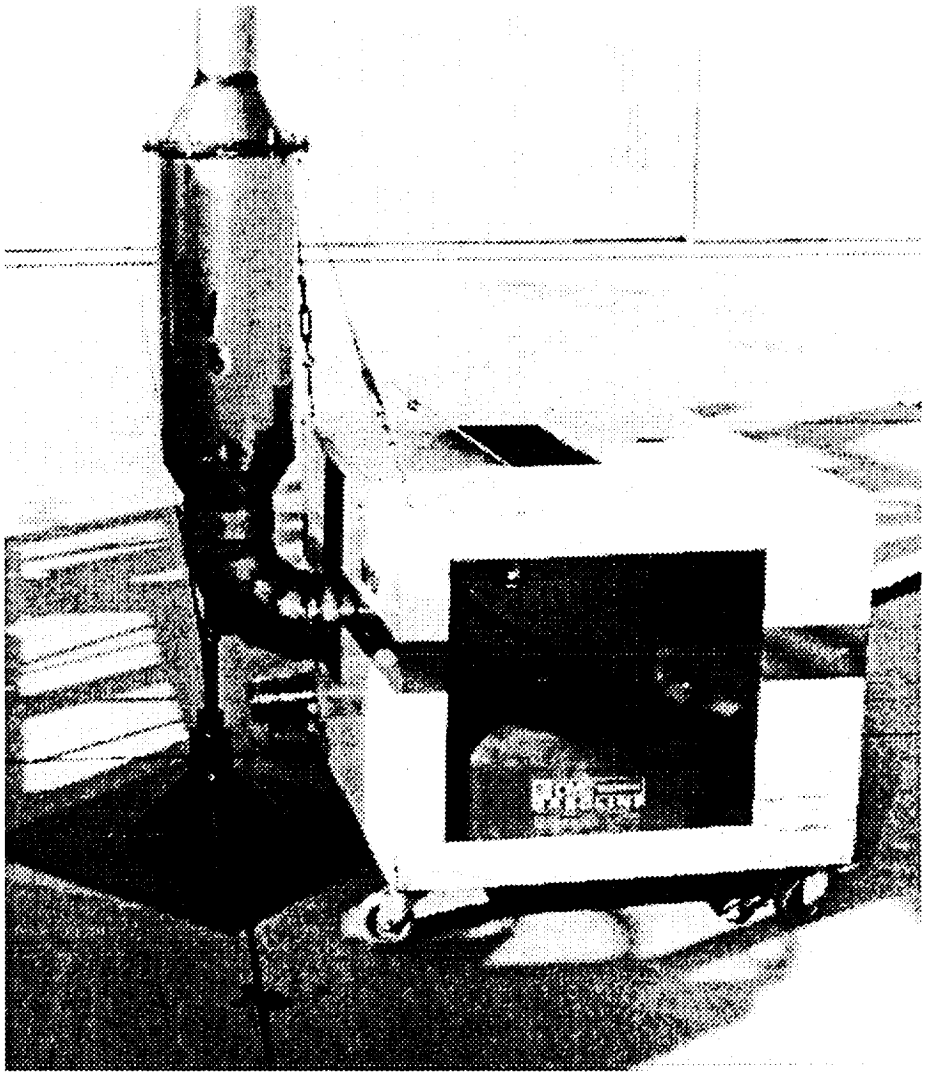

Figure 8. The auxiliary power unit (APU).

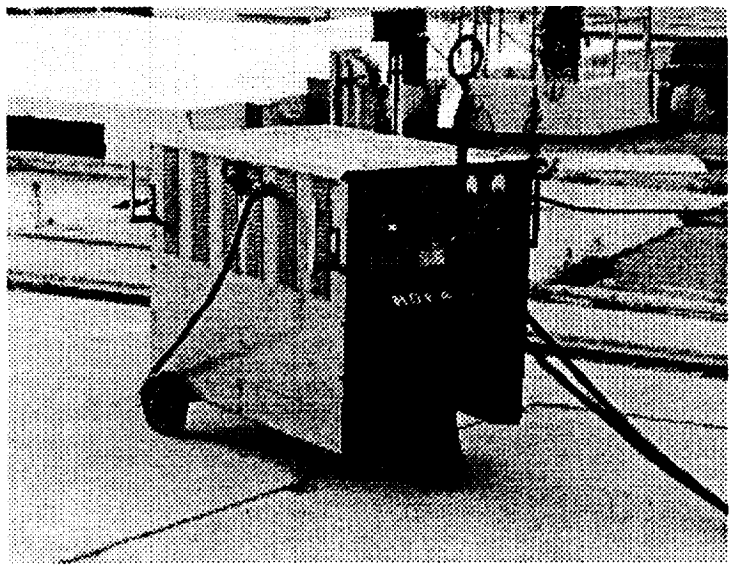

Figure 9. The Hobart 480-to-28-Vdc power supply.

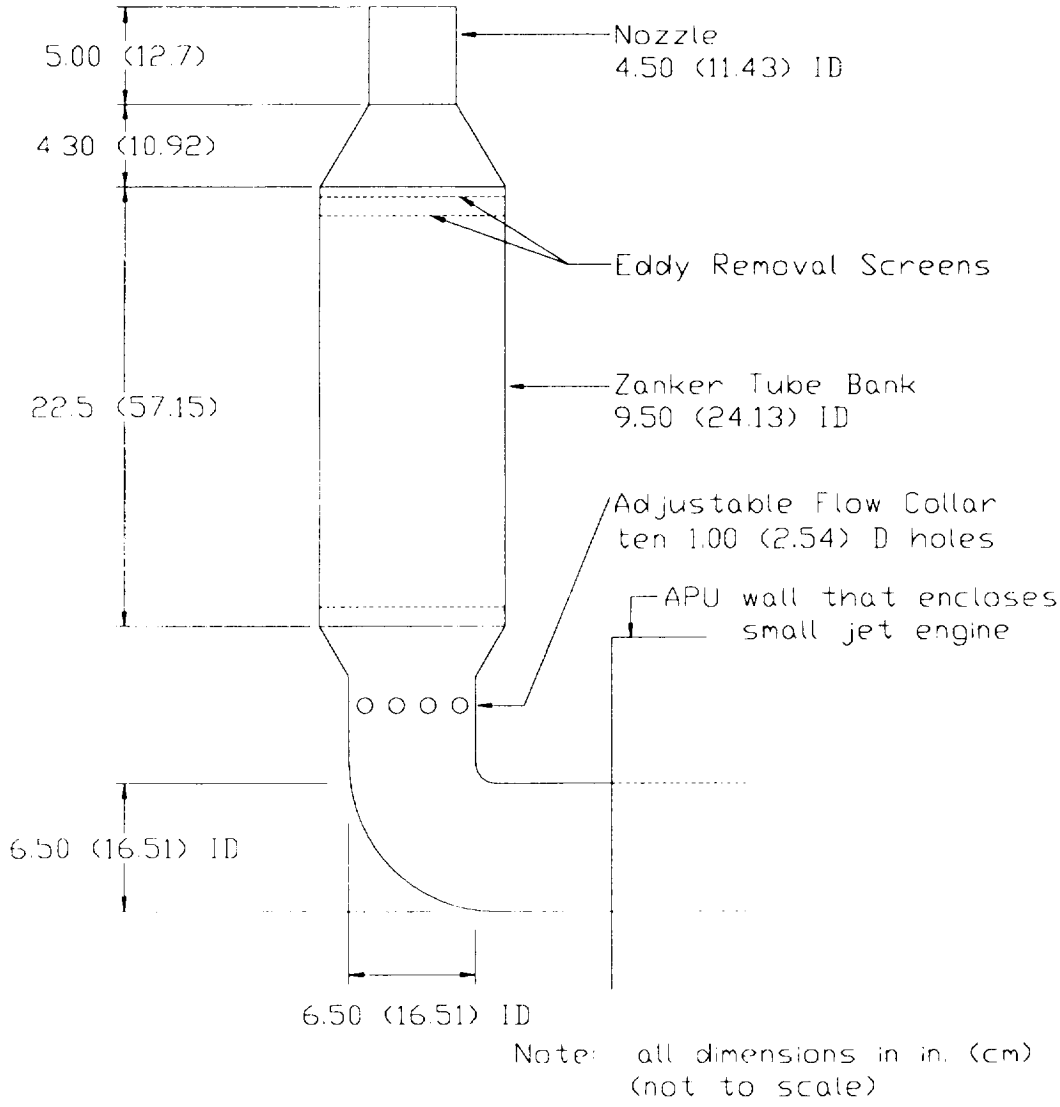

Figure10. The flow straightening assembly (ref. 20).

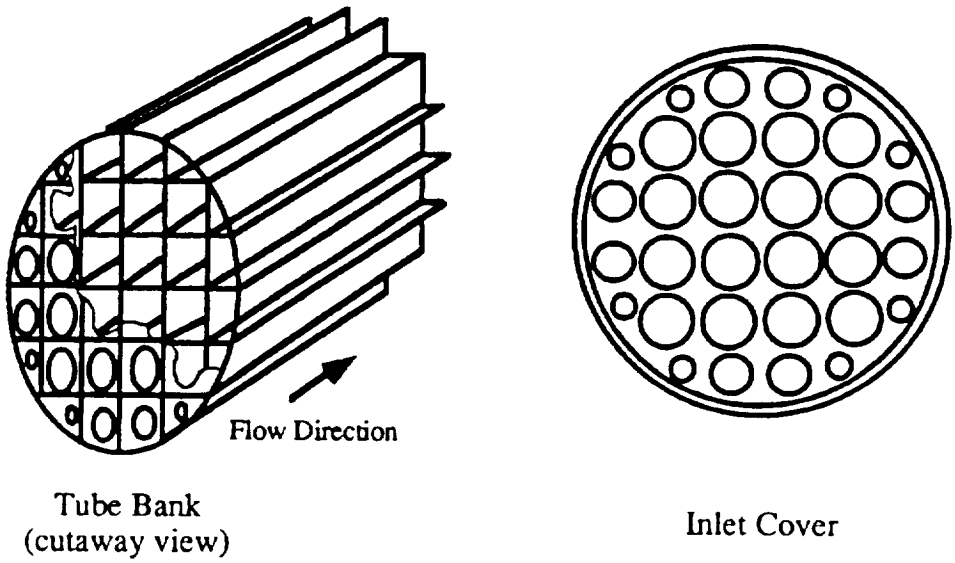

Figure 11. The Zanker flow straightener (ref. 20).

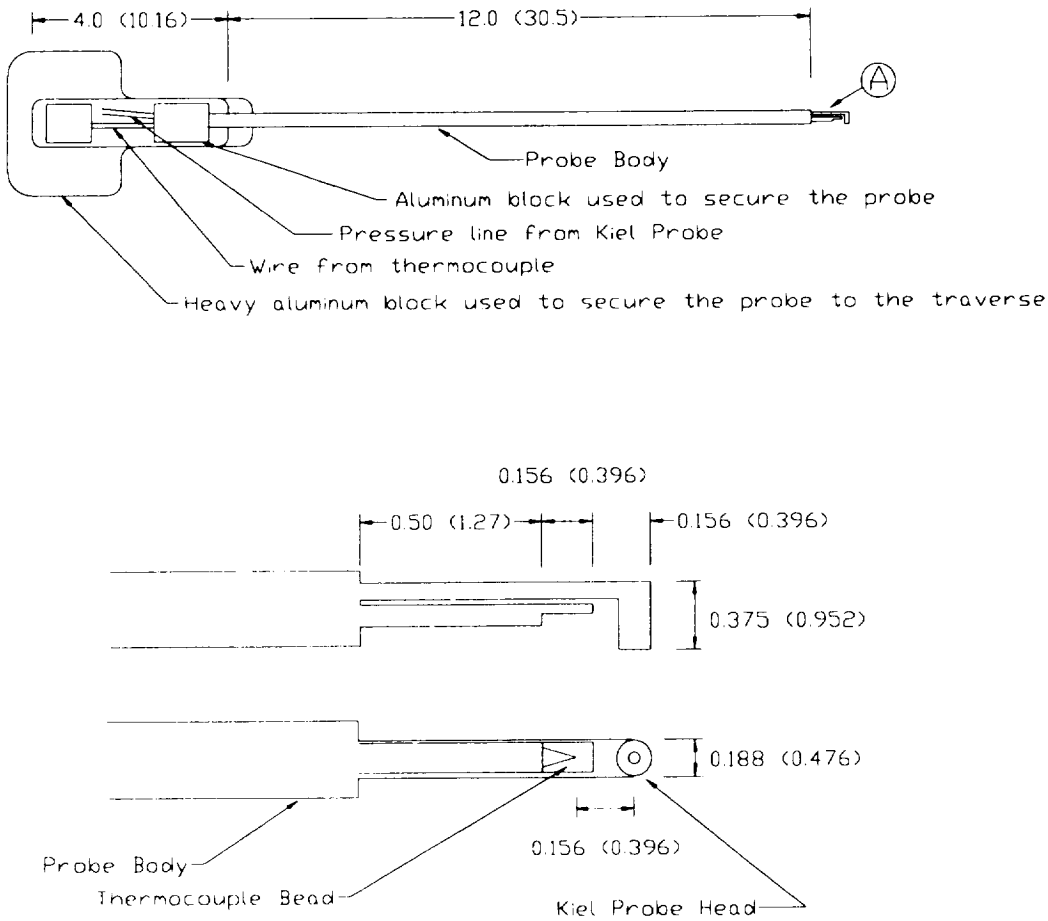

Figure 12. Combination thermocouple and Kiel probe.

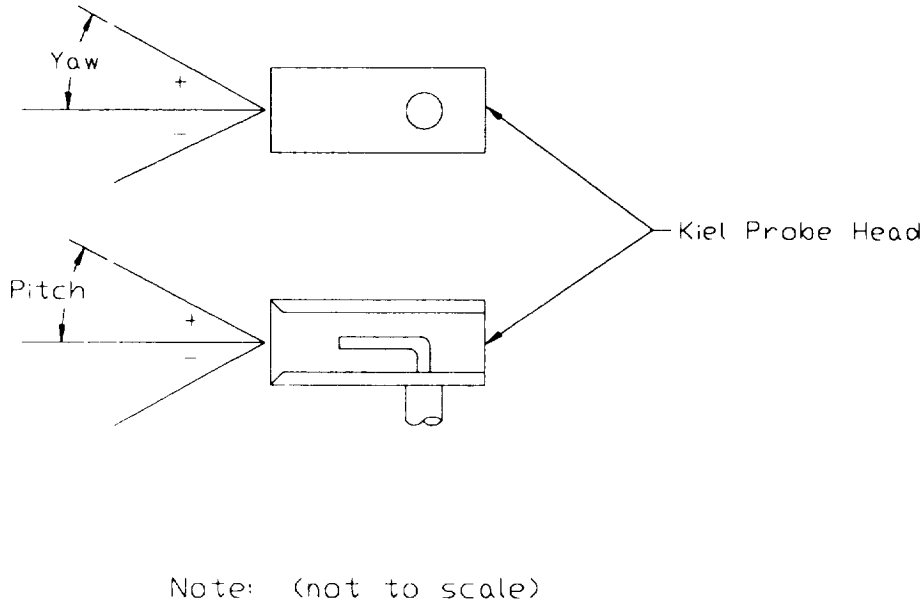

Figure 13. The yaw and pitch angles of the Kiel probe.

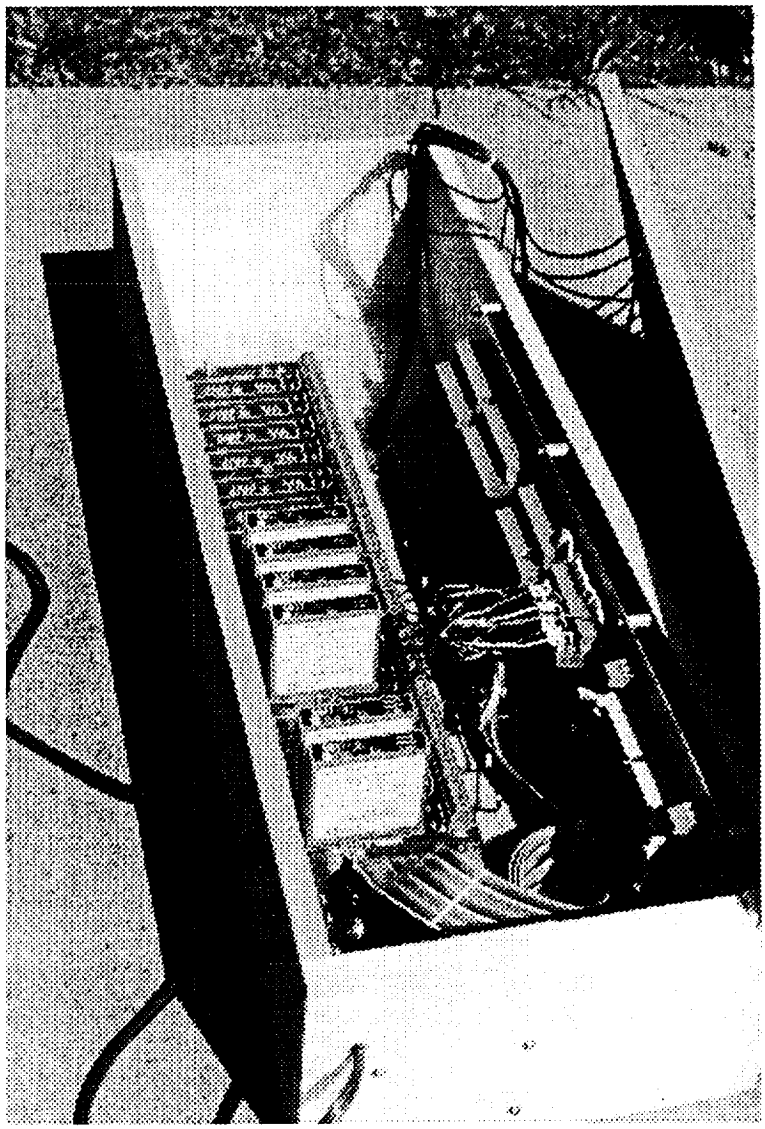

Figure 14. The signal conditioning unit (SCU) with the top removed to show the linear and nonlinear thermocouple modules.

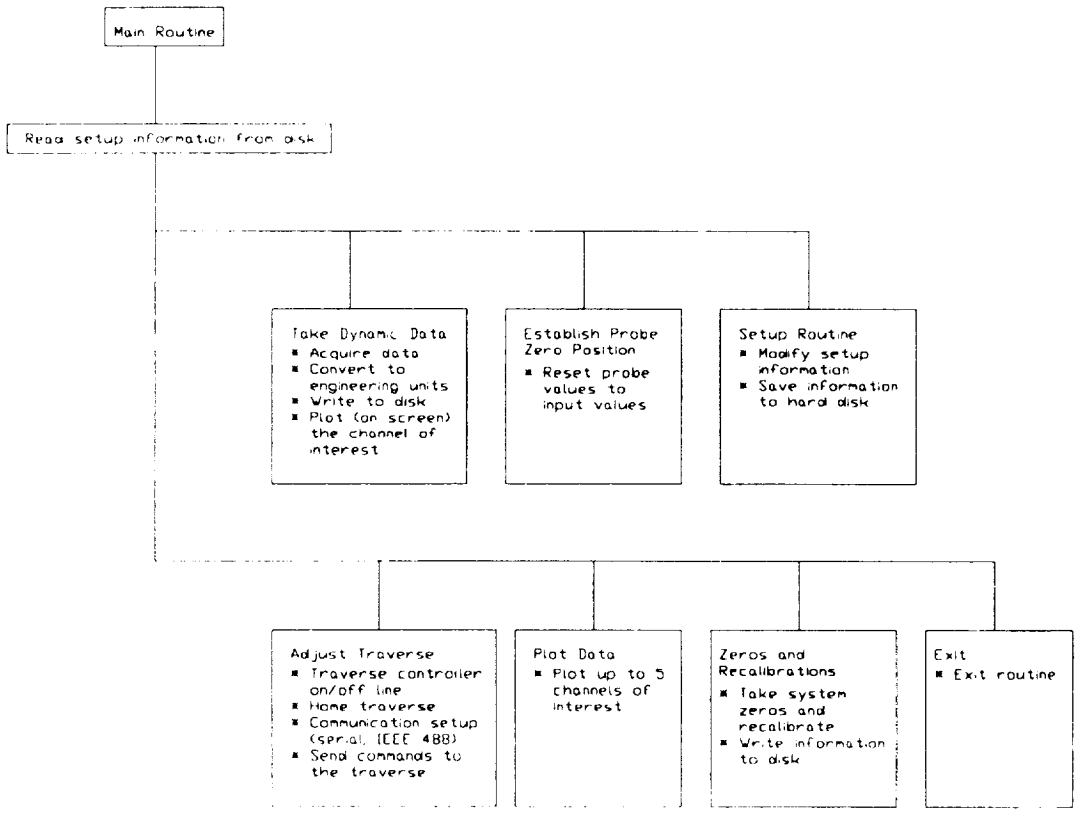

Figure 15. Flow chart of the Labview® data acquisition and analysis routine.

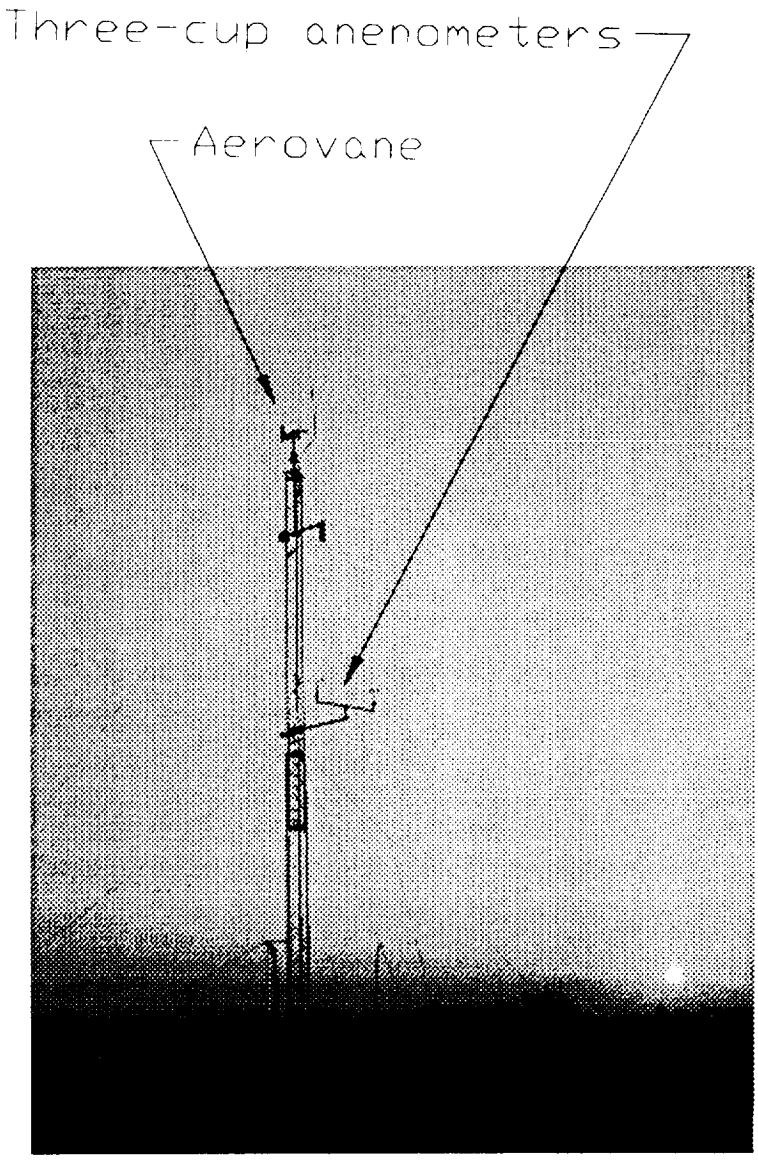

Figure 16. The weather station at the OARF.

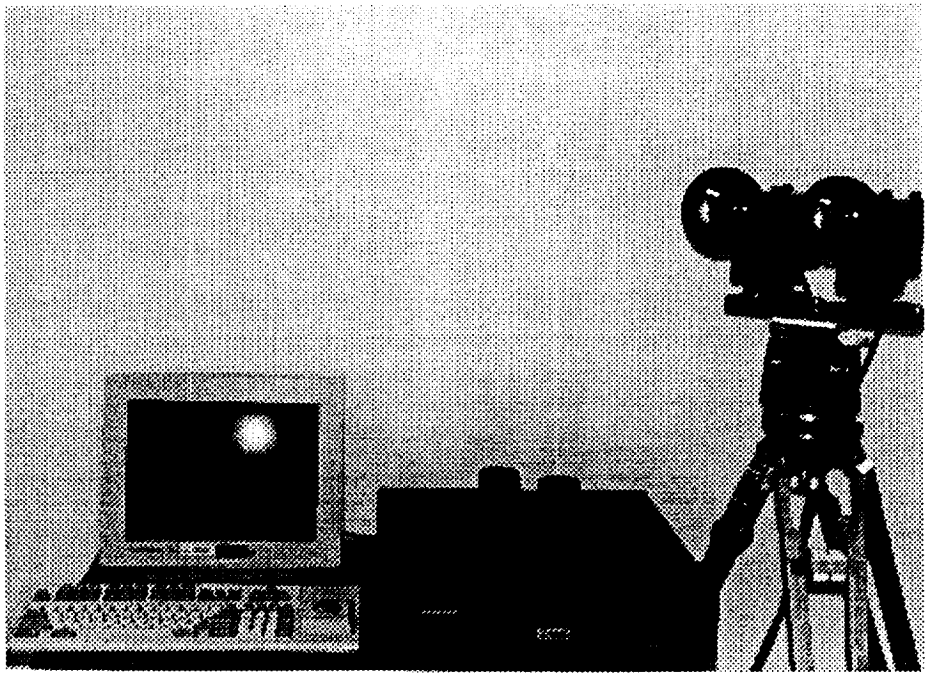

Figure 17. The Agema 880 Dual Waveband Infrared Imaging System.

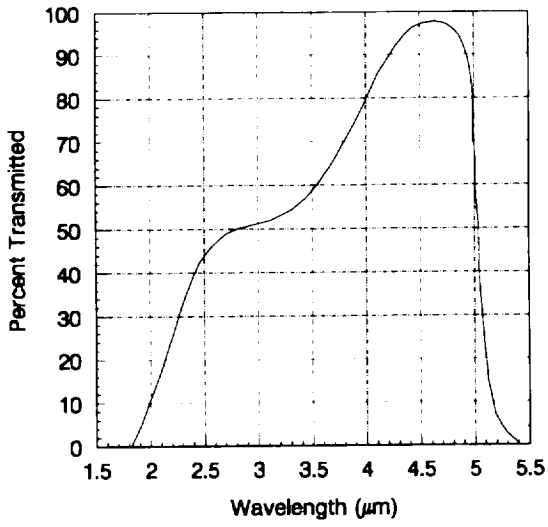

(a)

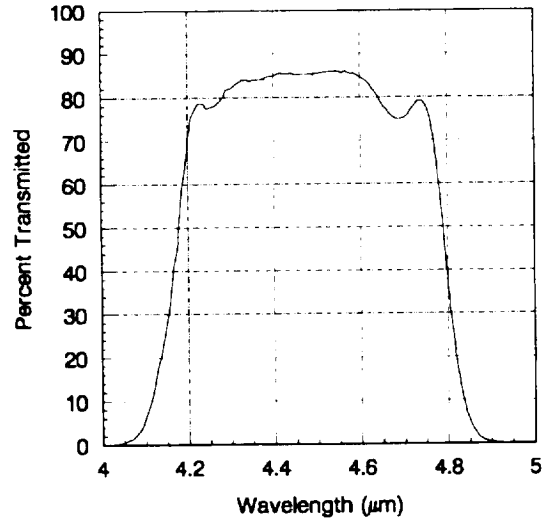

(b)

Figure 18. (a) Spectral response of the Agema 880 MWB camera, and (b) filtered response of the MWB infrared camera.

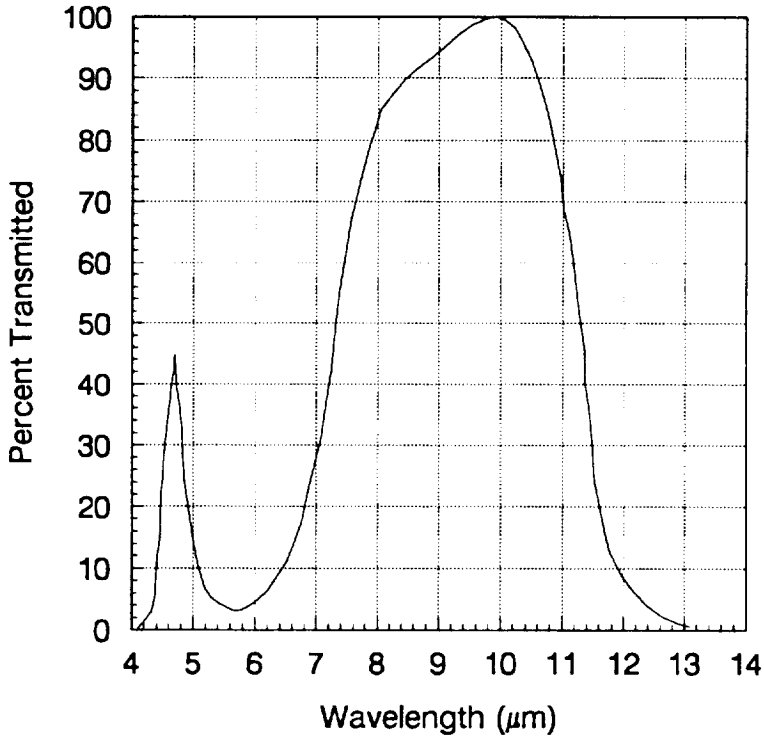

Figure 19. Spectral response of the Agema 880 LWB camera.

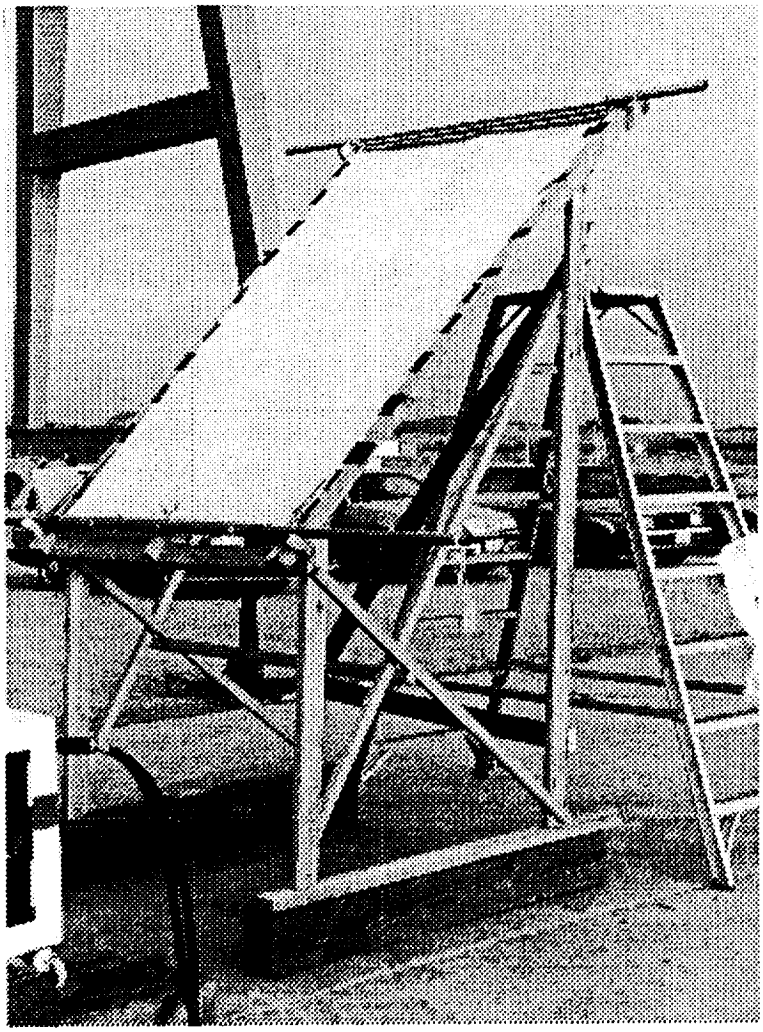

Figure 20. The aluminized Mylar backdrop.

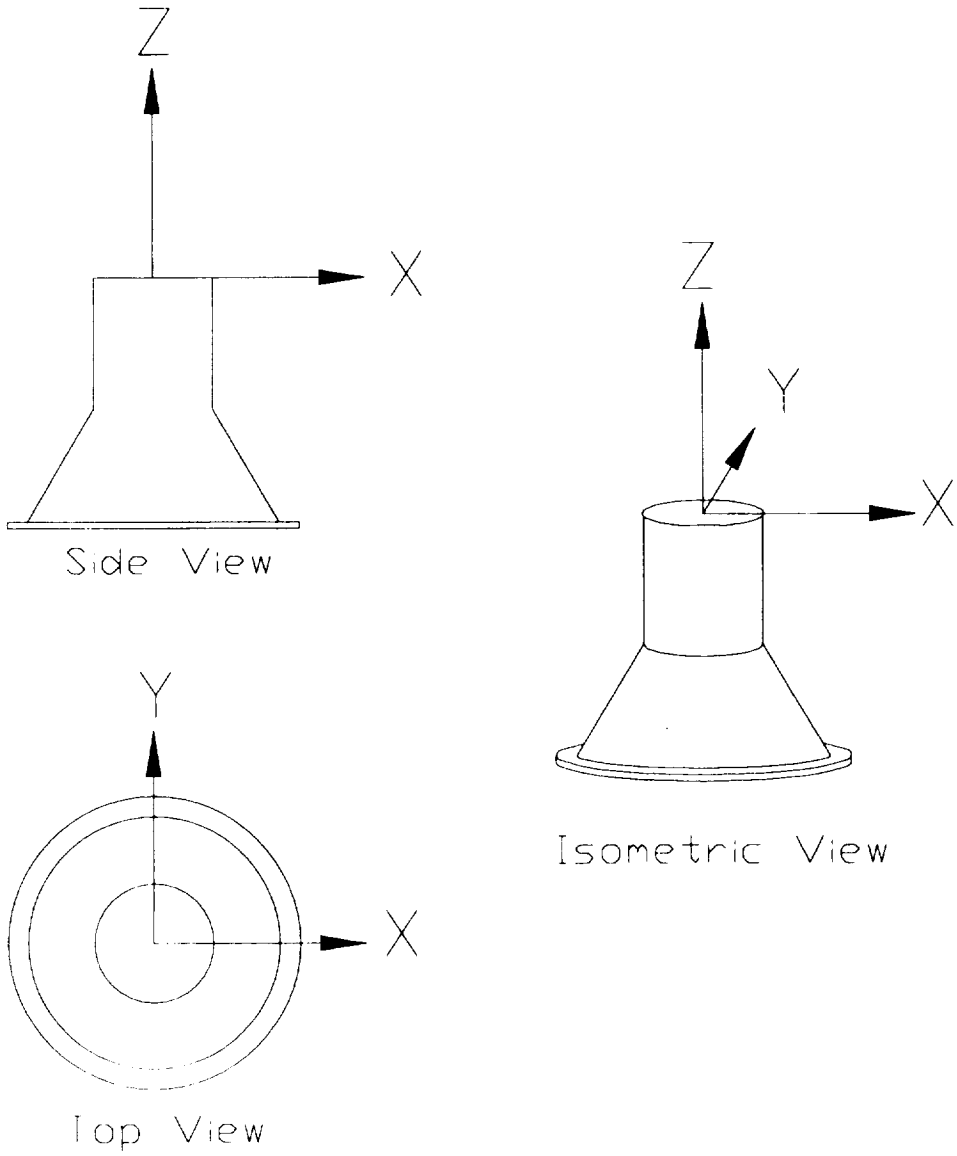

Figure 21. Orientation of x-y-z axes with respect to the axisymmetric nozzle.

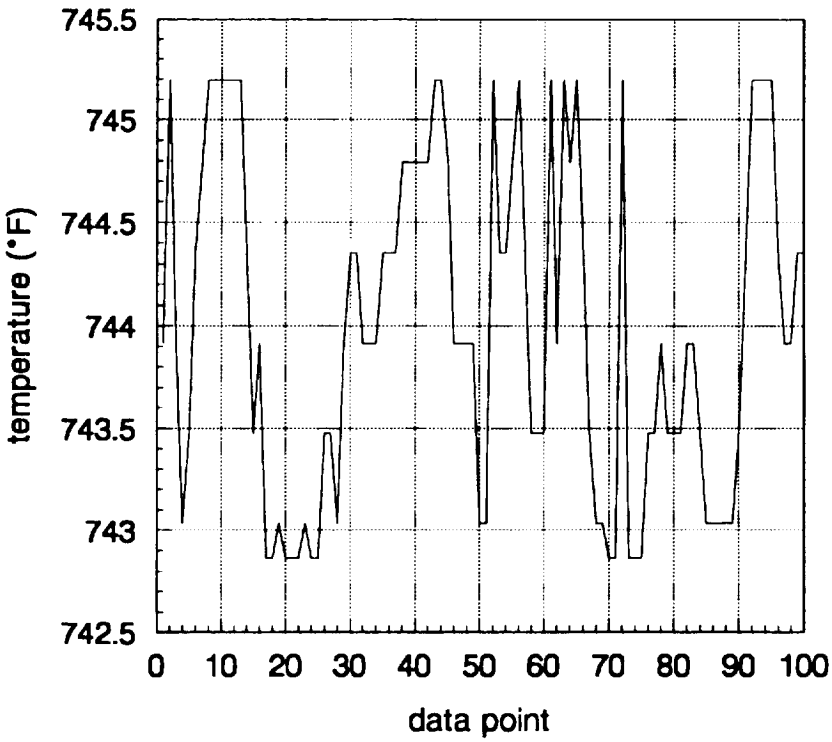

Figure 22. An example of conditioned temperature data showing "clipping."

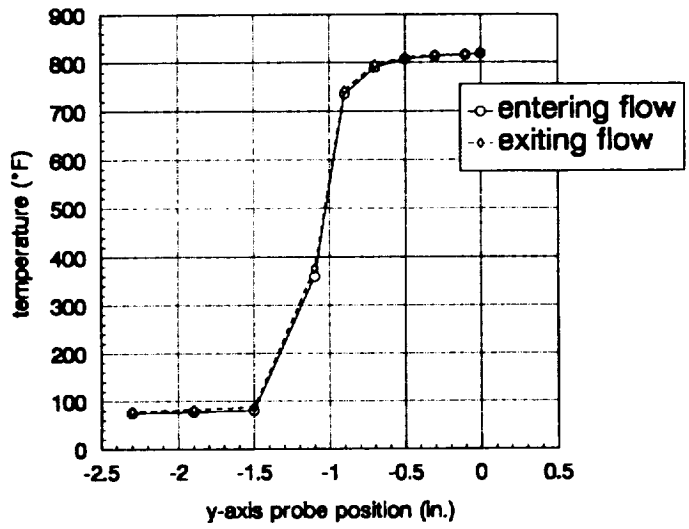

(a)

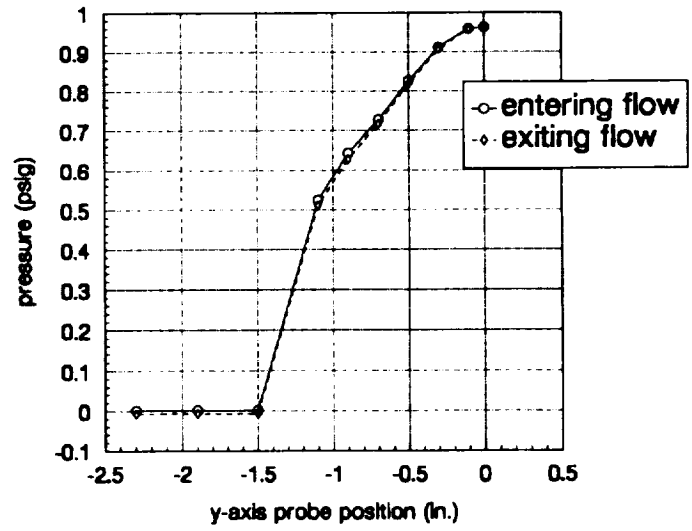

(b)

Figure 23. (a) Temperature and (b) Pressure profile as the probe enters and exits the exhaust flow.

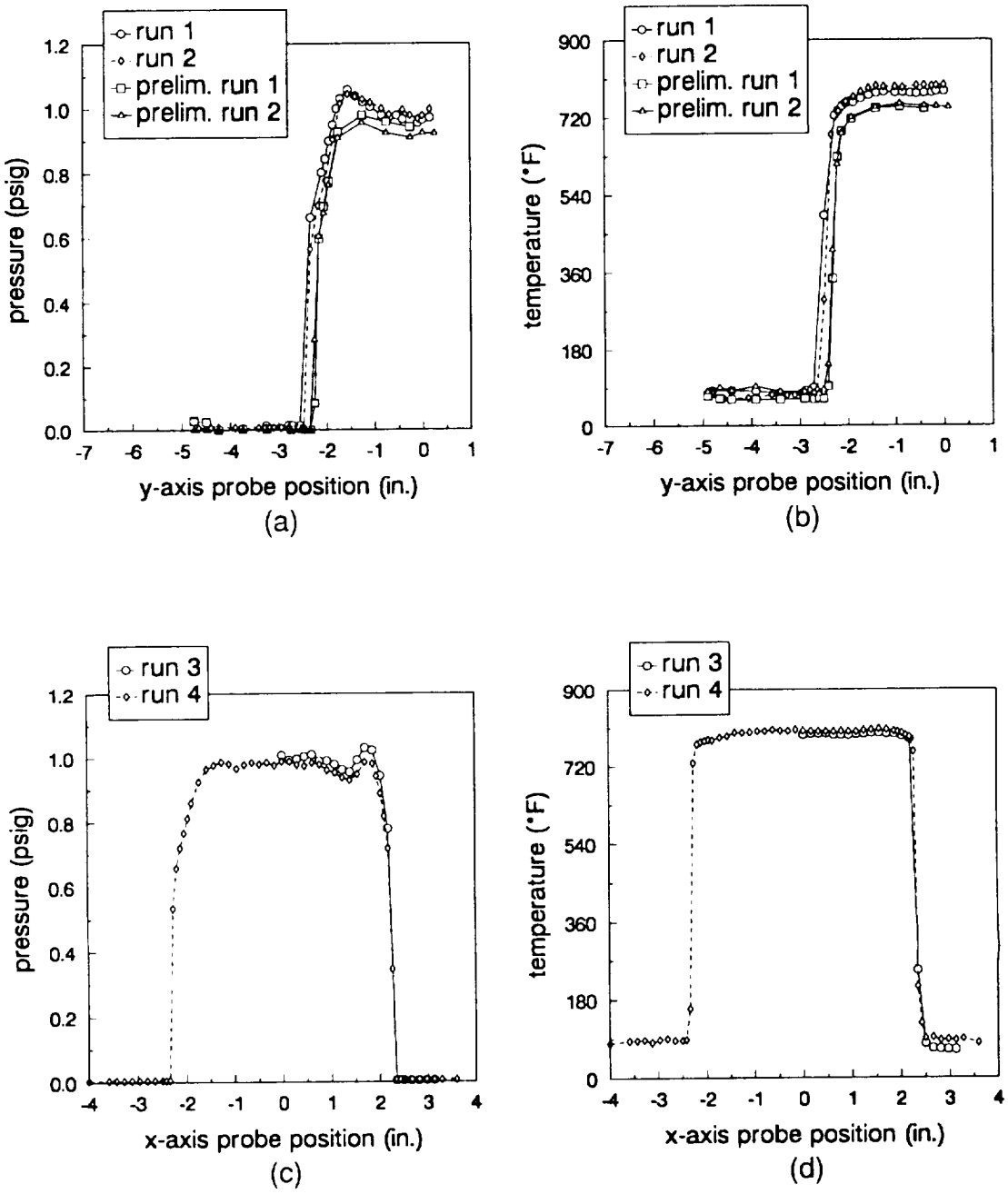

Figure 24. Experimental temperature and pressure measurements obtained at the exit plane, z = 0.0 in.

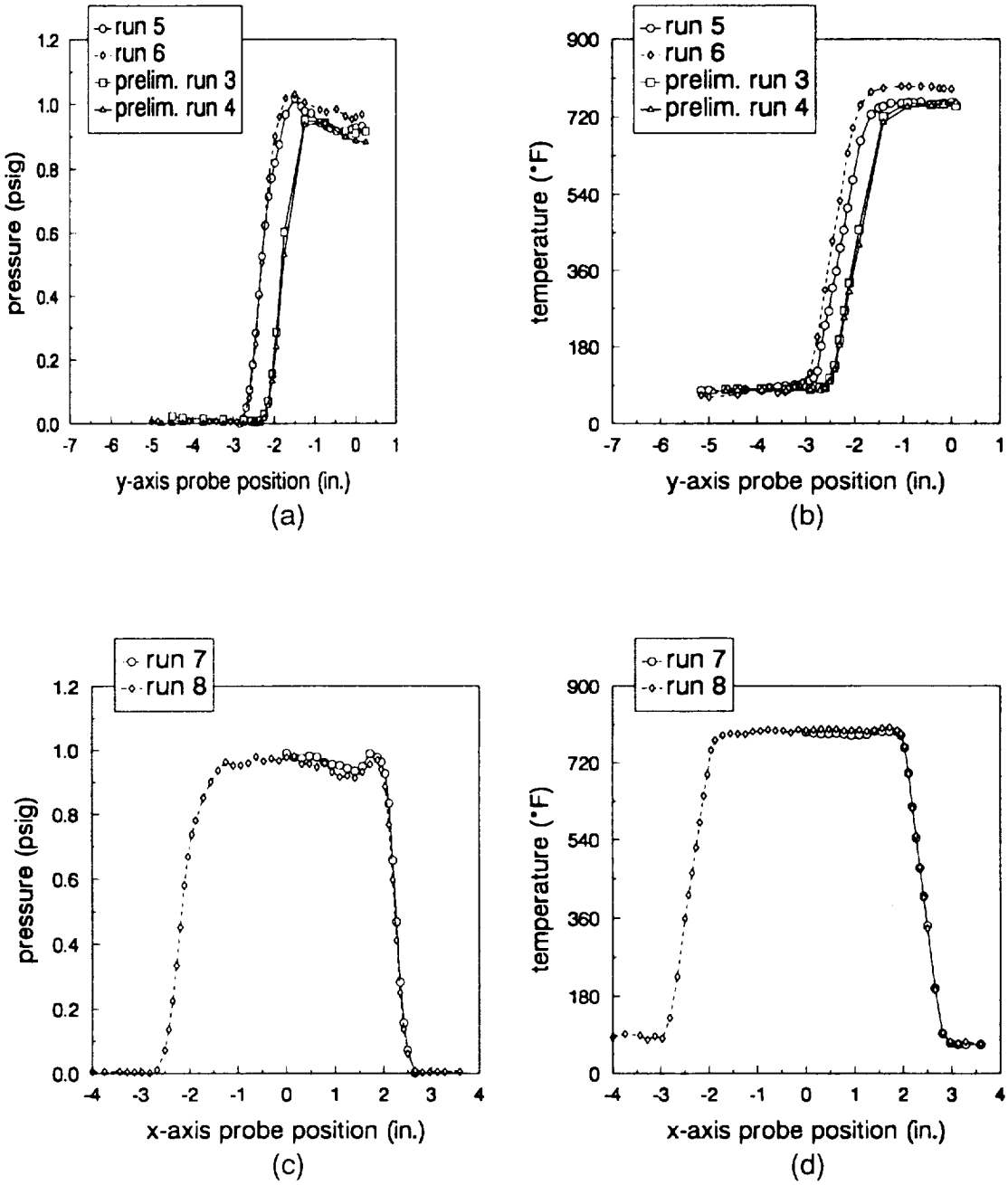

Figure 25. Experimental temperature and pressure measurements obtained one-half diameter downstream, z = 2.25 in.

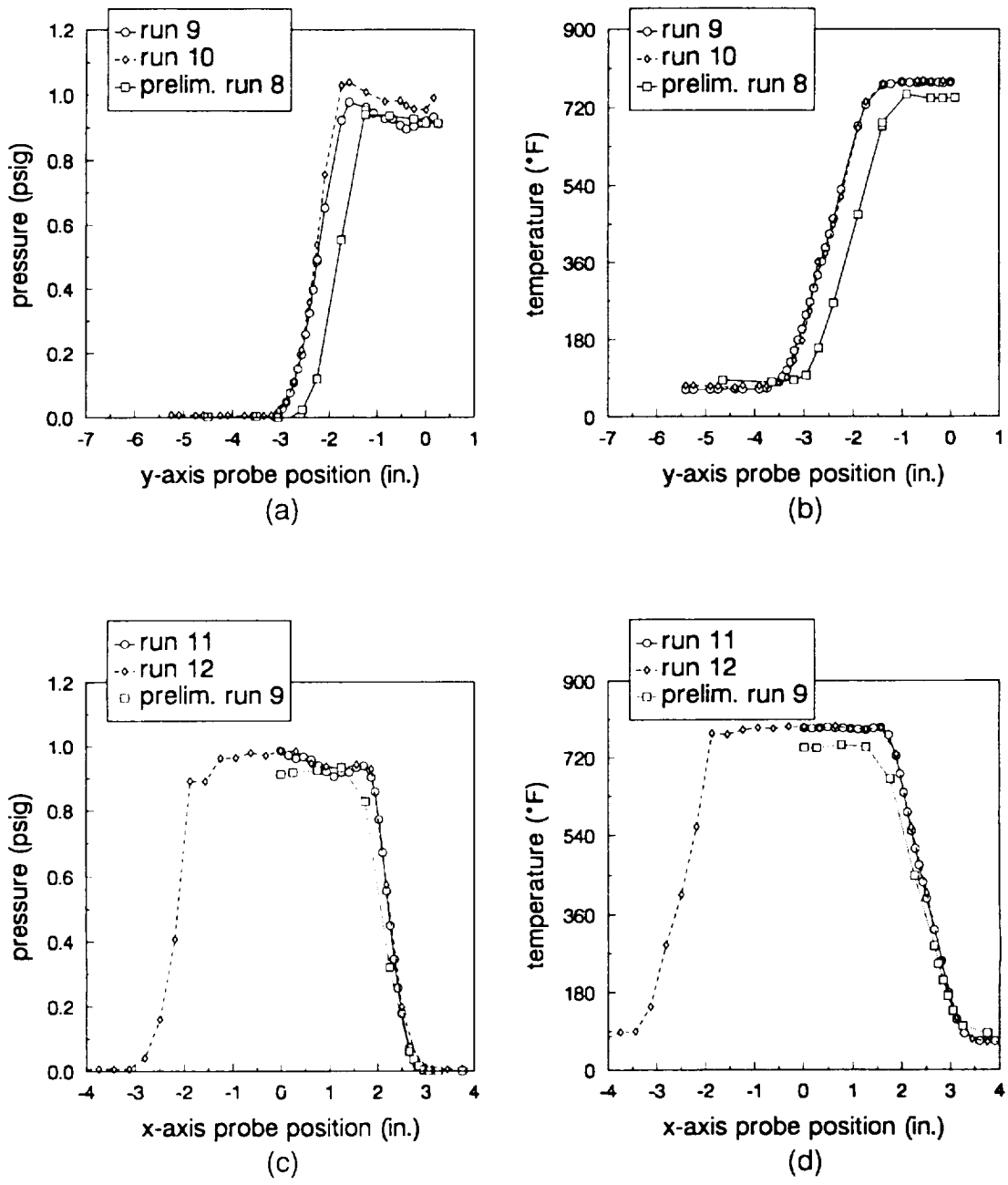

Figure 26. Experimental temperature and pressure measurements obtained one diameter downstream, z = 4.5 in.

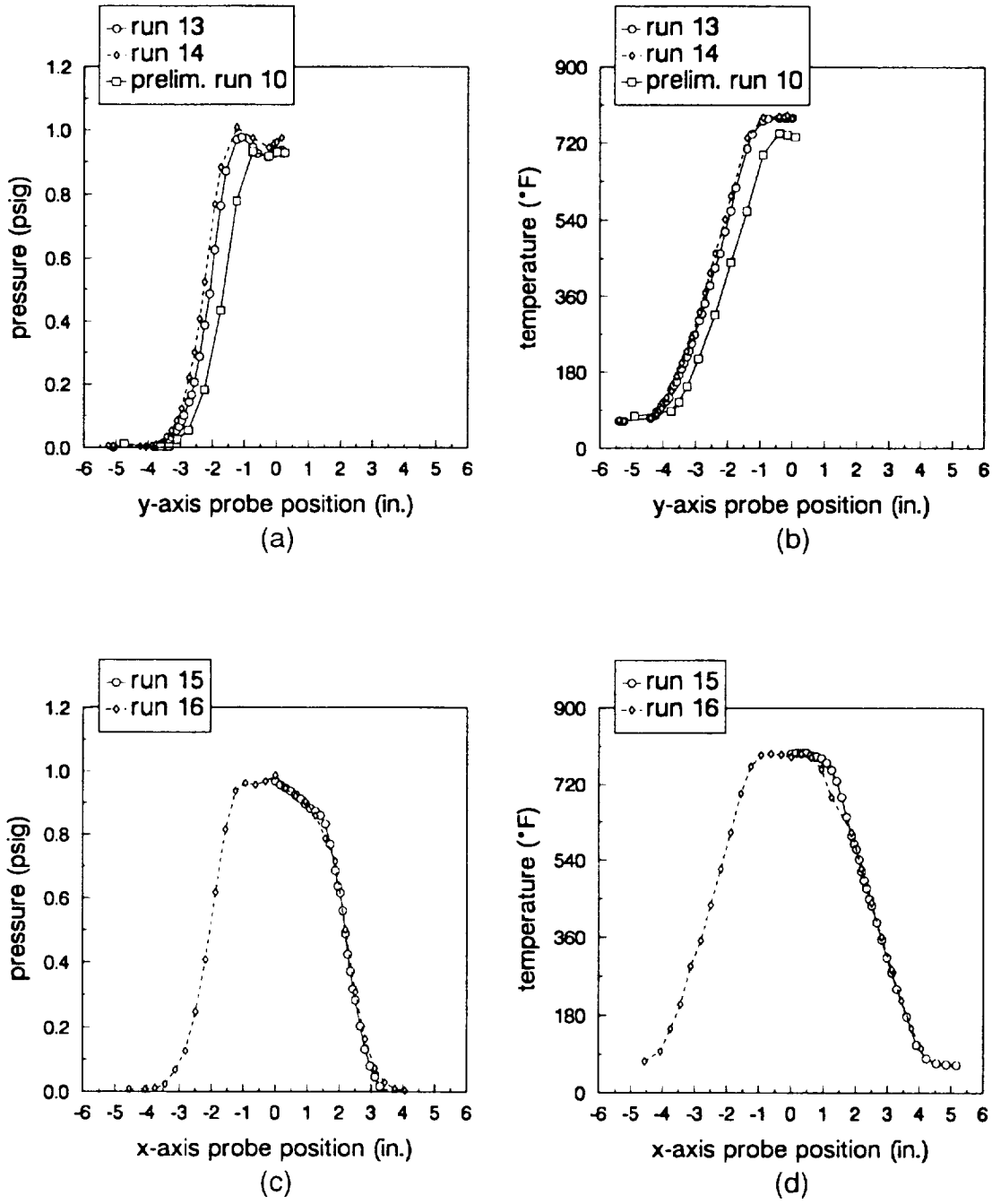

Figure 27. Experimental temperature and pressure measurements obtained two diameters downstream, z = 9.0 in.

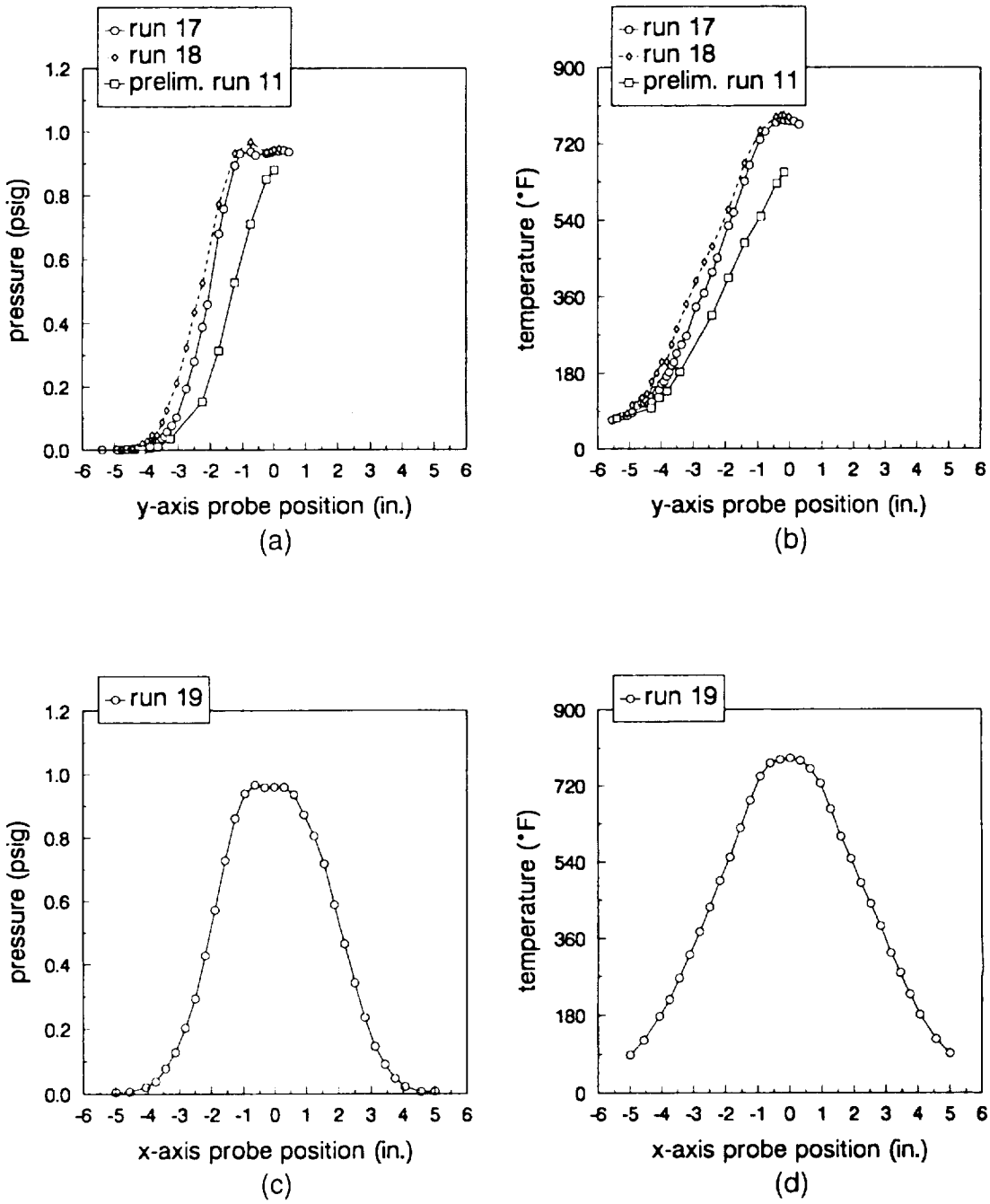

Figure 28. Experimental temperature and pressure measurements obtained three diameters downstream, z = 13.5 in.

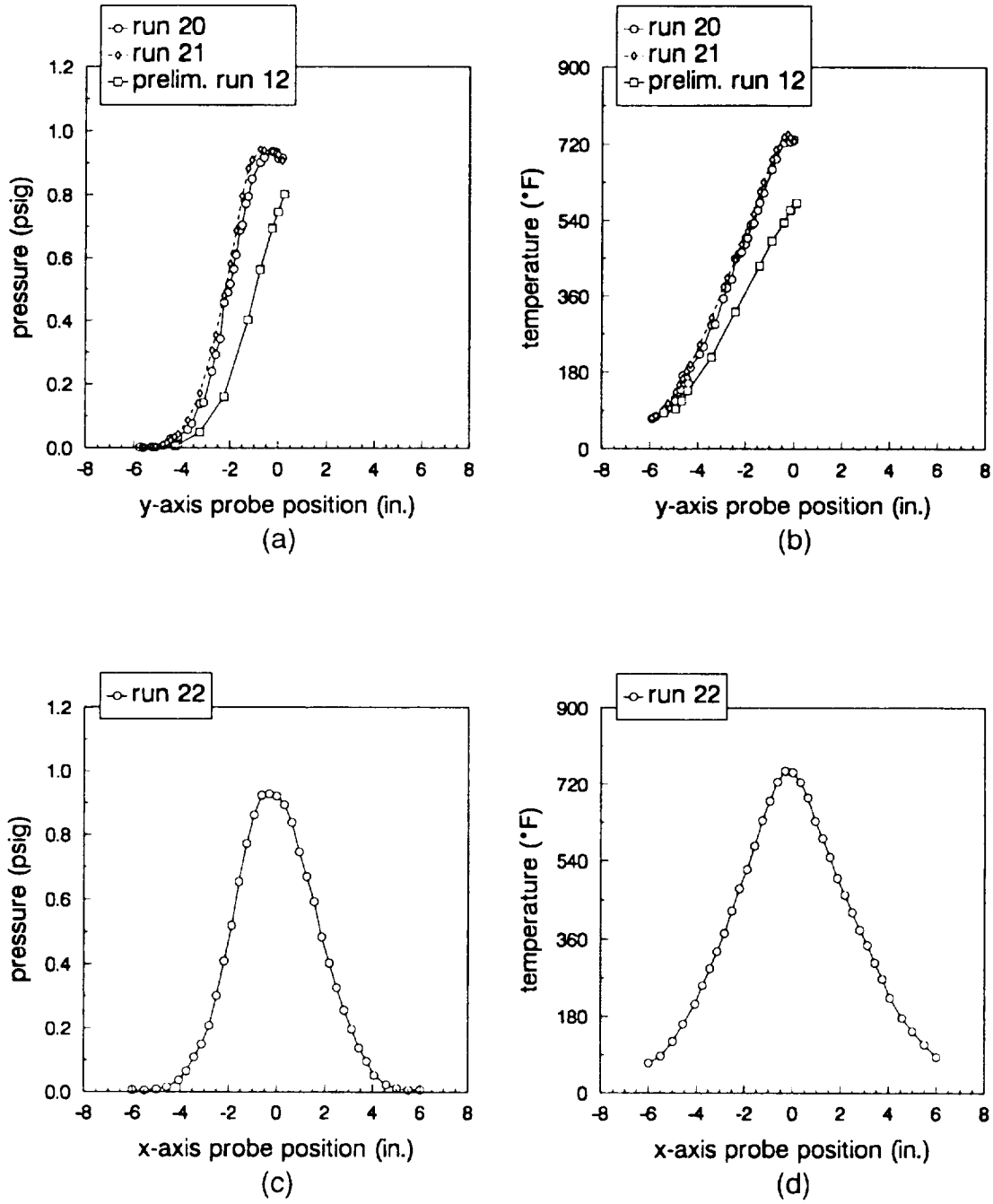

Figure 29. Experimental temperature and pressure measurements obtained four diameters downstream, z = 18.0 in.

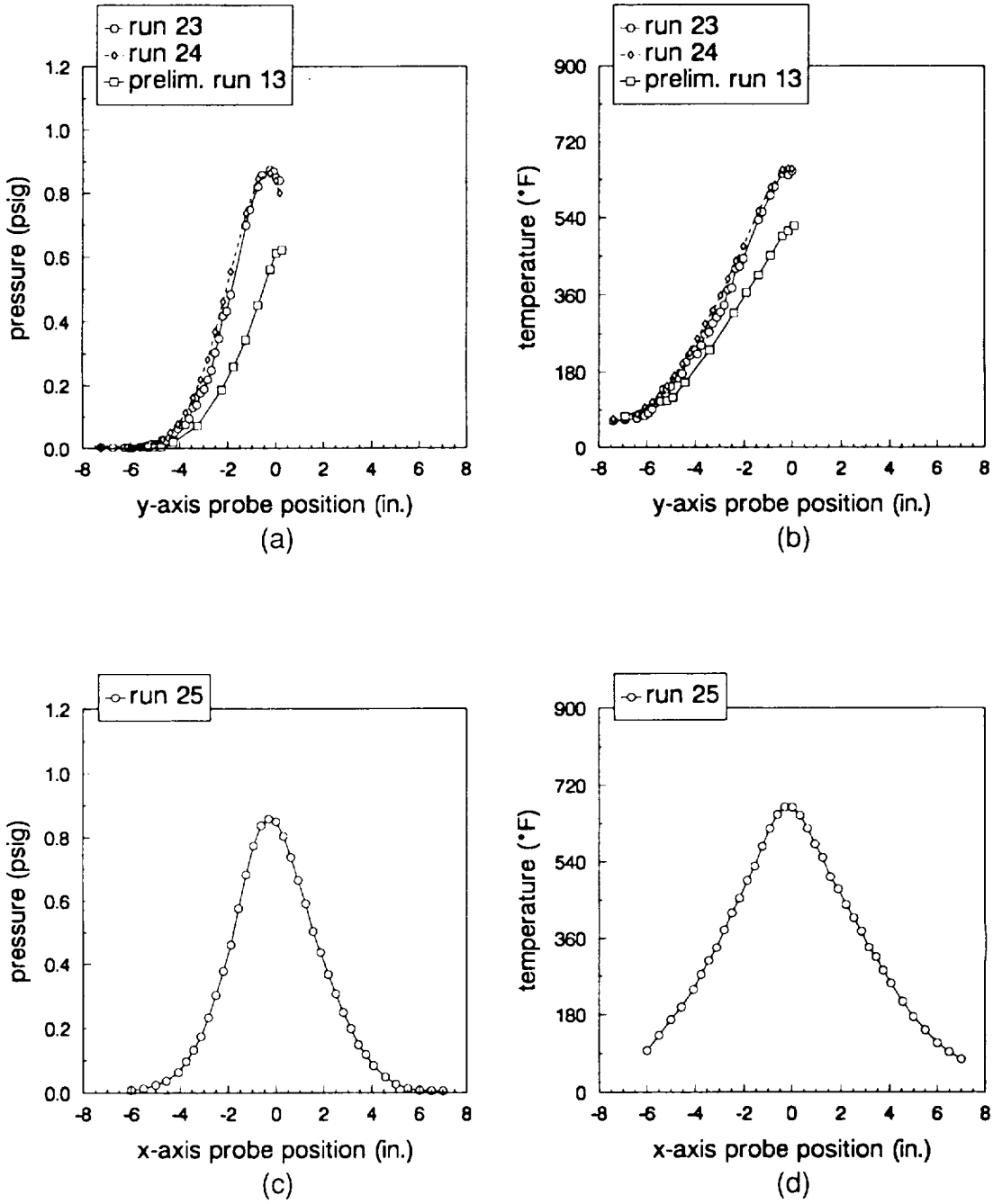

Figure 30. Experimental temperature and pressure measurements obtained five diameters downstream, z = 22.5 in.

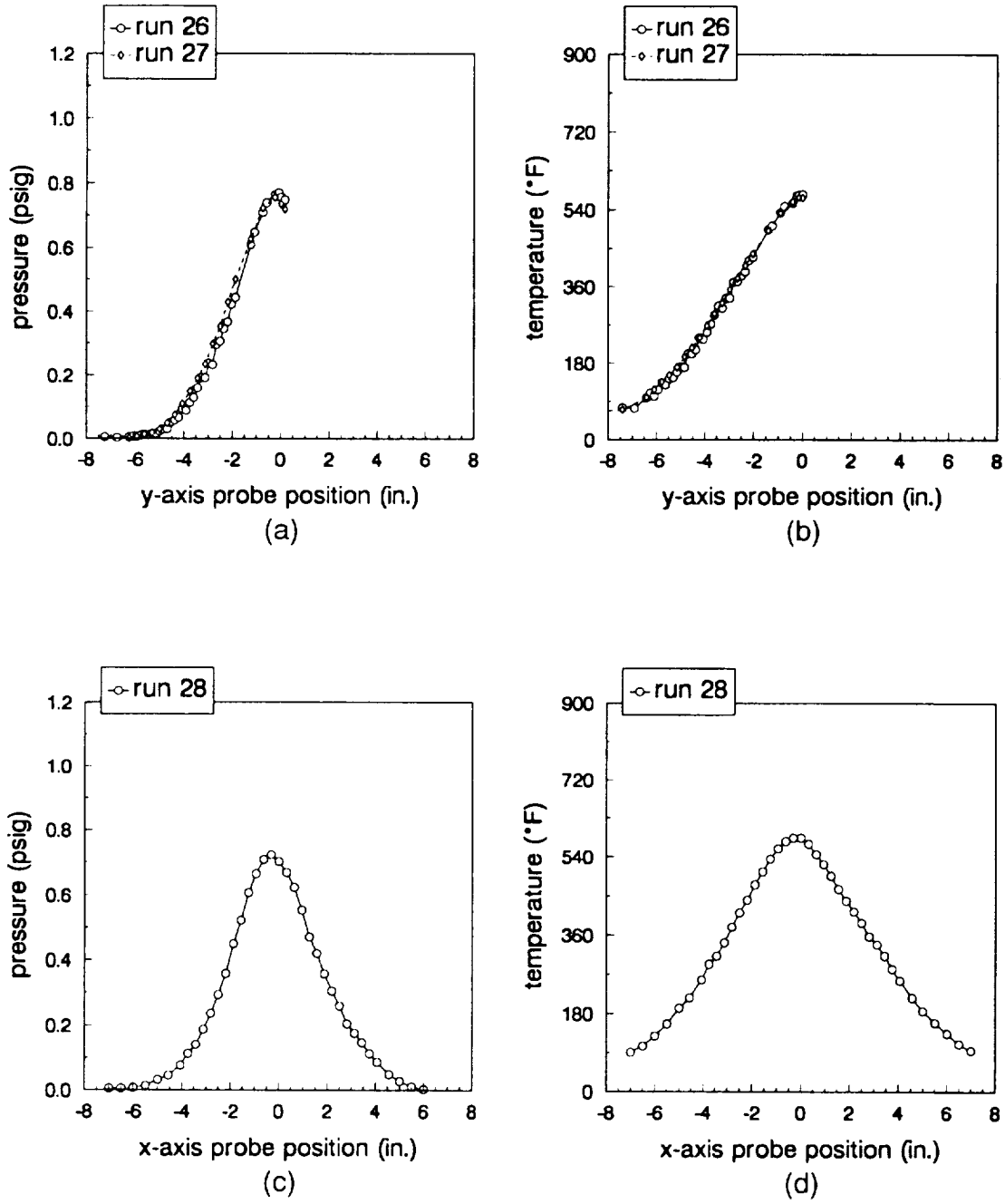

Figure 31. Experimental temperature and pressure measurements obtained six diameters downstream, z = 27.0 in.

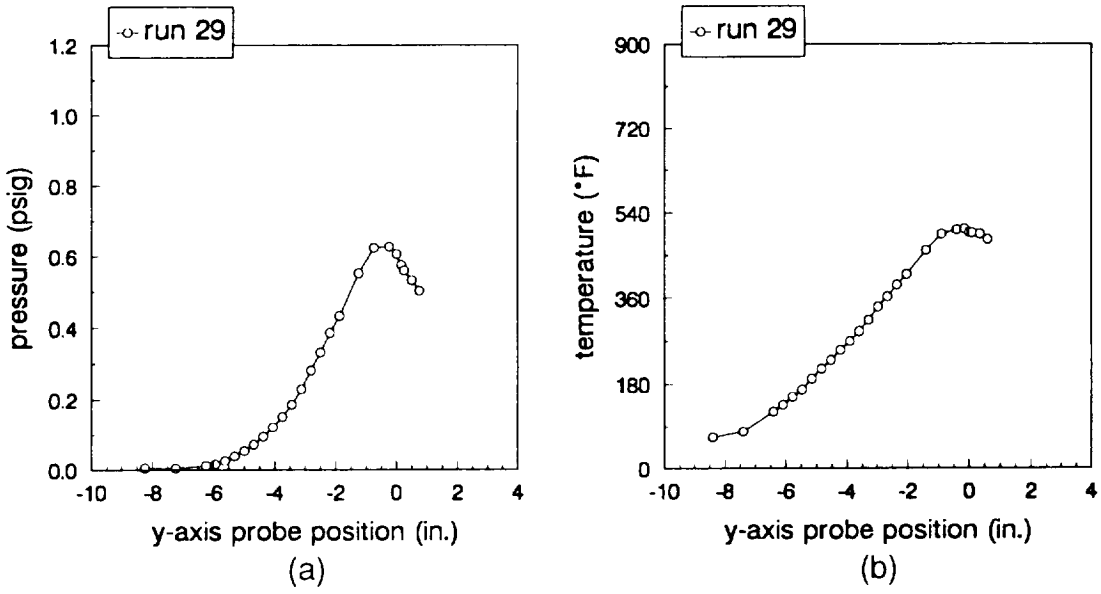

Figure 32. Experimental temperature and pressure measurements obtained seven diameters downstream, z = 31.5 in.

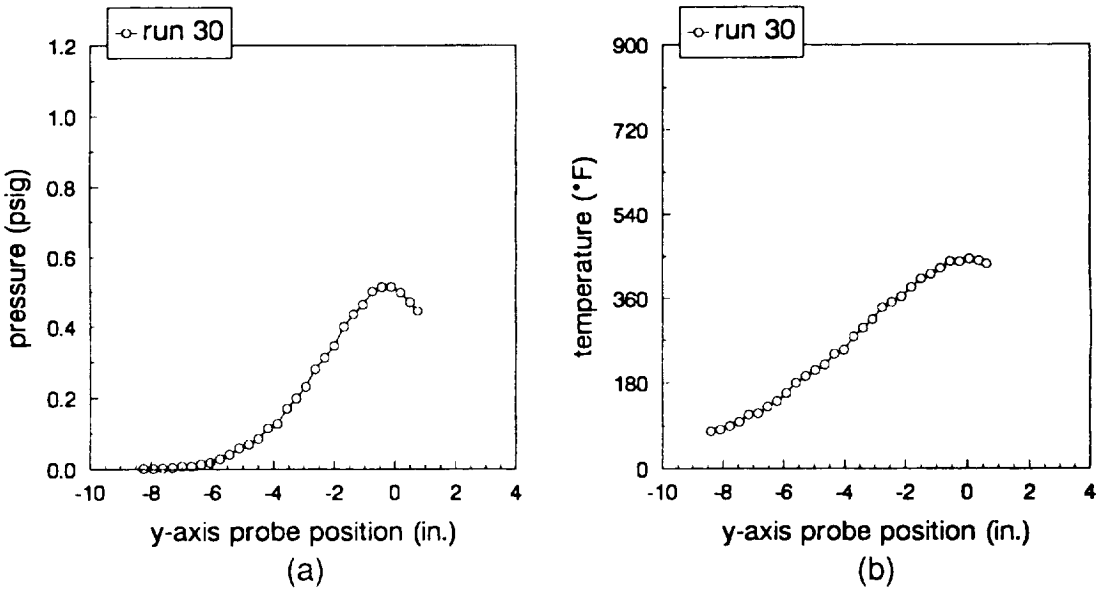

Figure 33. Experimental temperature and pressure measurements obtained eight diameters downstream, z = 36.0 in.

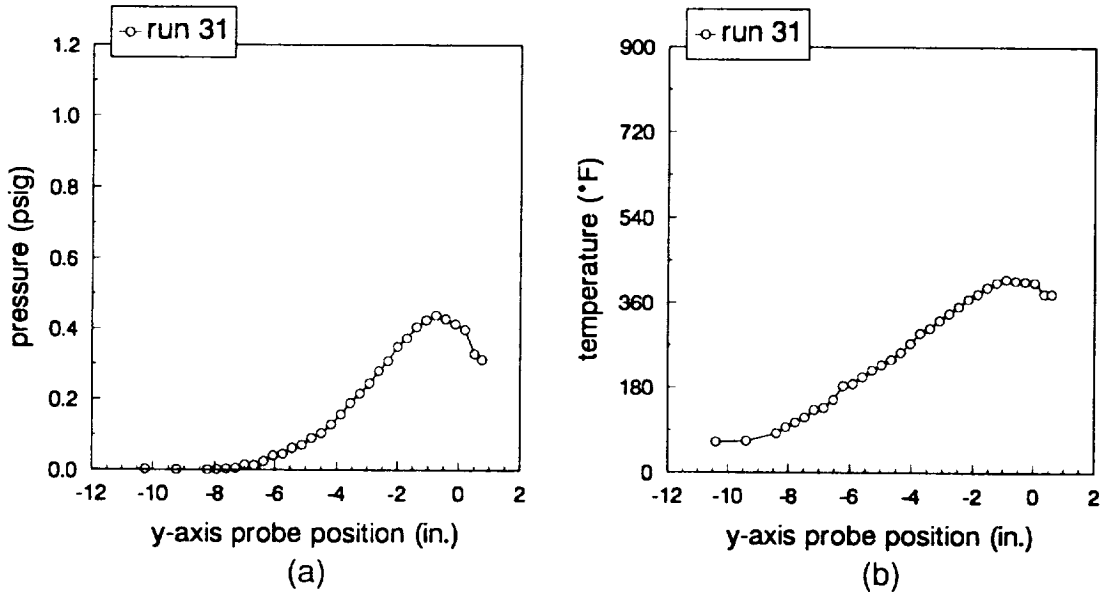

Figure 34. Experimental temperature and pressure measurements obtained nine diameters downstream, z = 40.5 in.

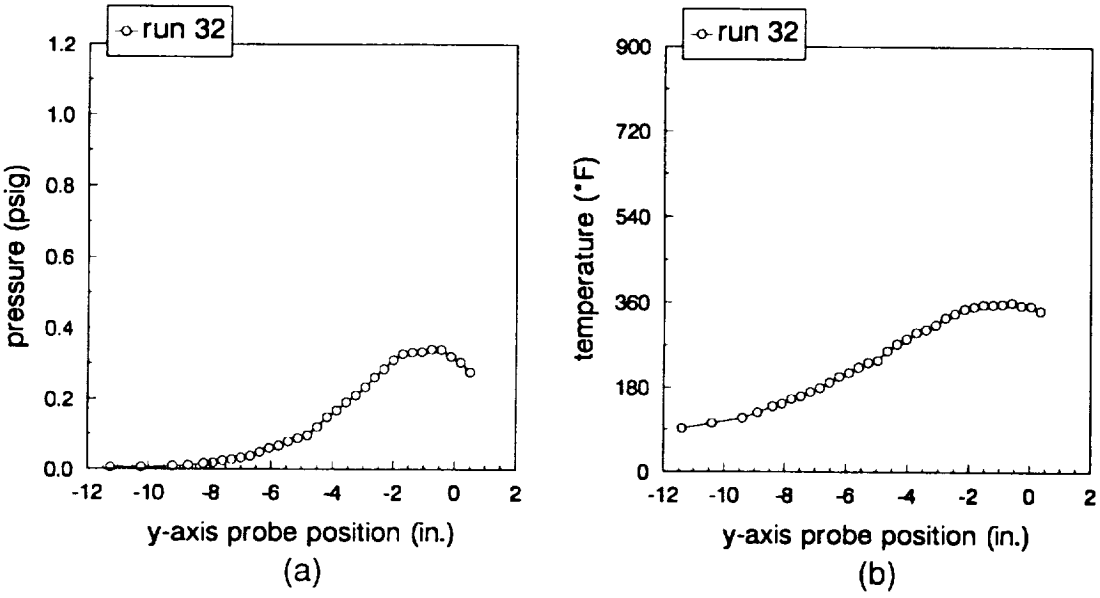

Figure 35. Experimental temperature and pressure measurements obtained ten diameters downstream, z = 45.0 in.

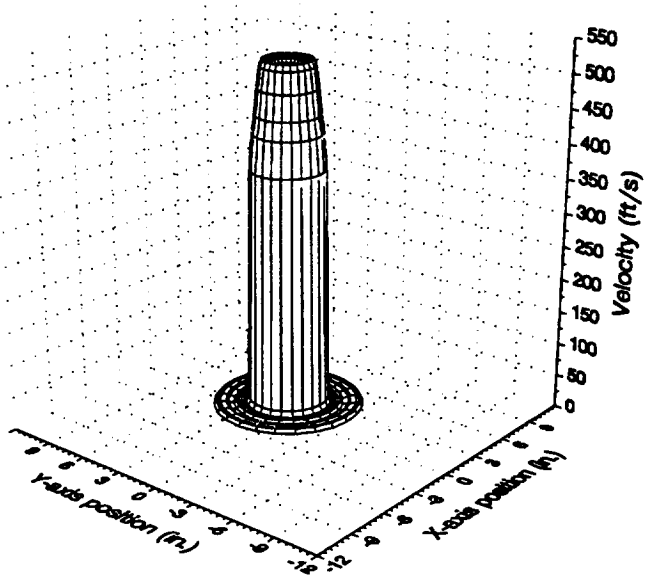

(a)

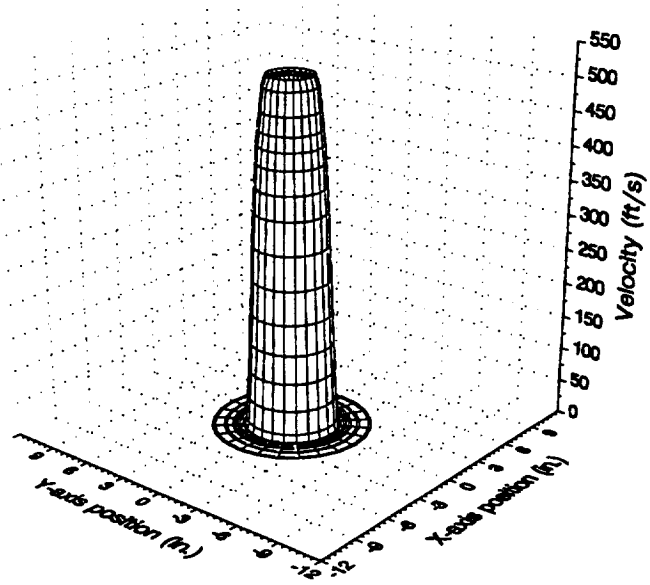

(b)

Figure 36. (a) Velocity profile at the exit plane, z = 0.0 in. (b) Velocity profile at one-half diameter downstream, z = 2.25 in.

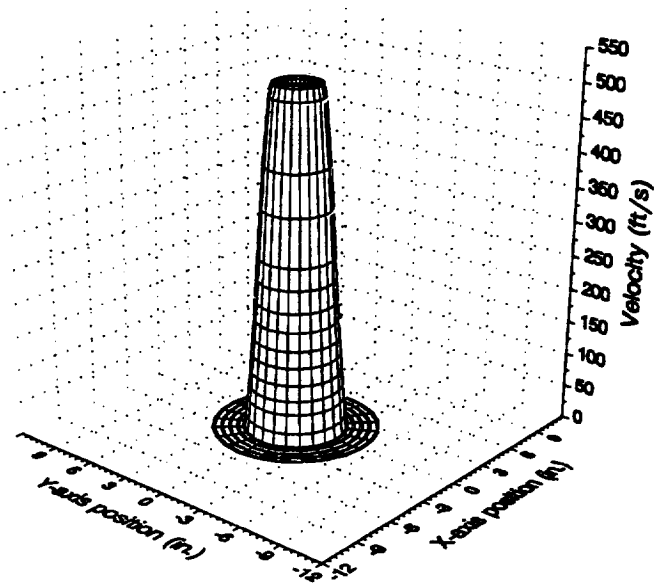

(a)

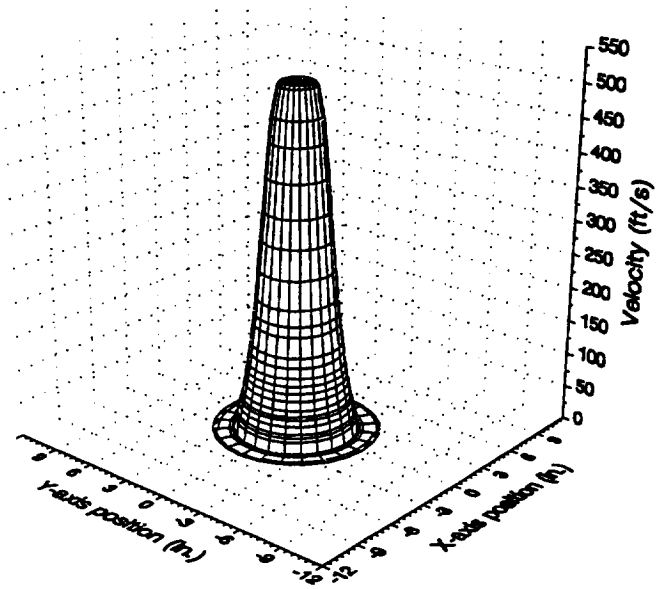

(b)

Figure 37. (a) Velocity profile at one diameter downstream, z = 4.5 in. (b) Velocity profile at two diameters downstream, z = 9.0 in.

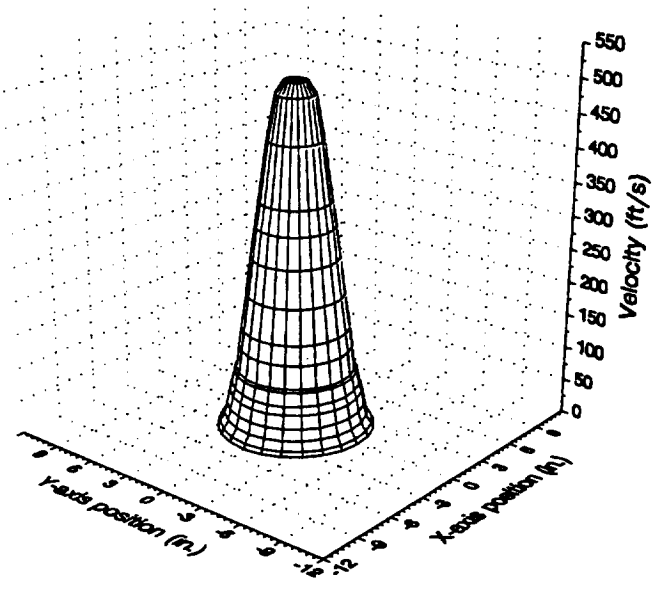

(a)

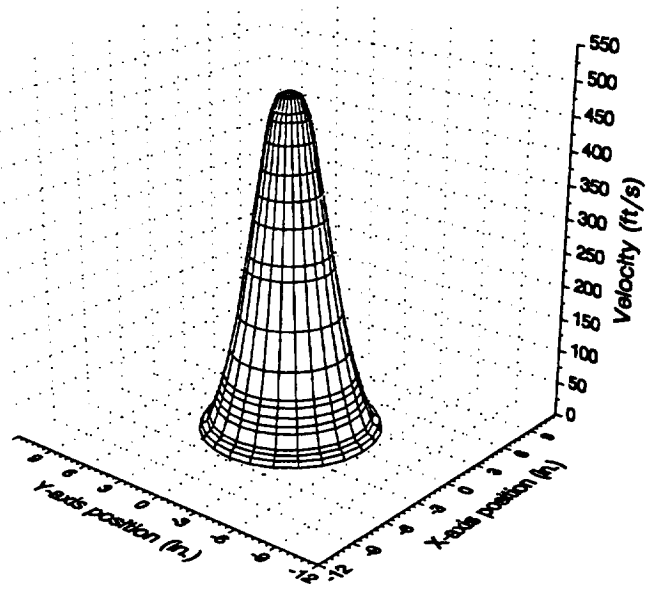

(b)

Figure 38. (a) Velocity profile at three diameters downstream, z = 13.5 in. (b) Velocity profile at four diameters downstream, z = 18.0 in.

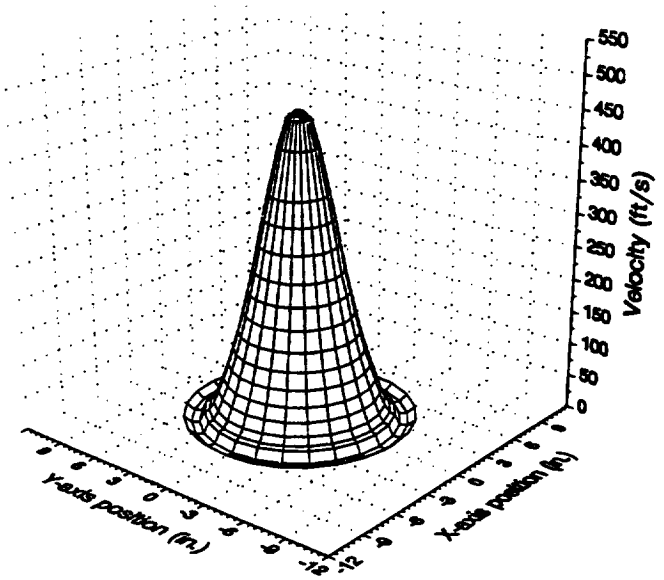

(a)

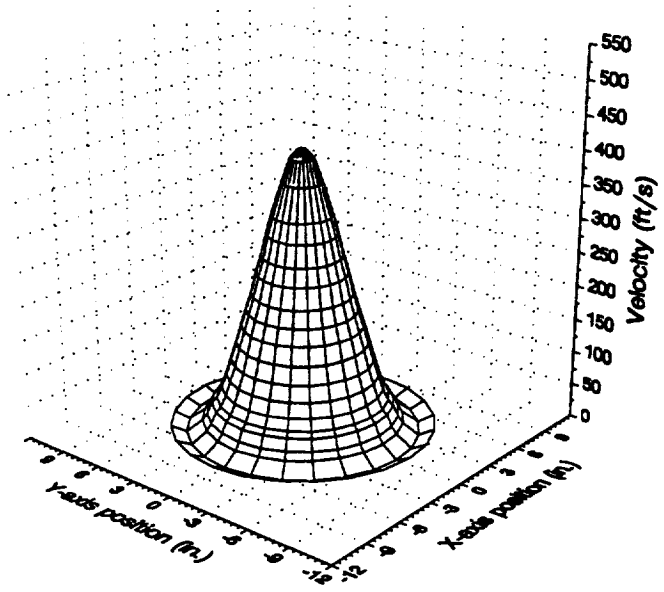

(b)

Figure 39. (a) Velocity profile at five diameters downstream, z = 22.5 in. (b) Velocity profile at six diameters downstream, z = 27.0 in.

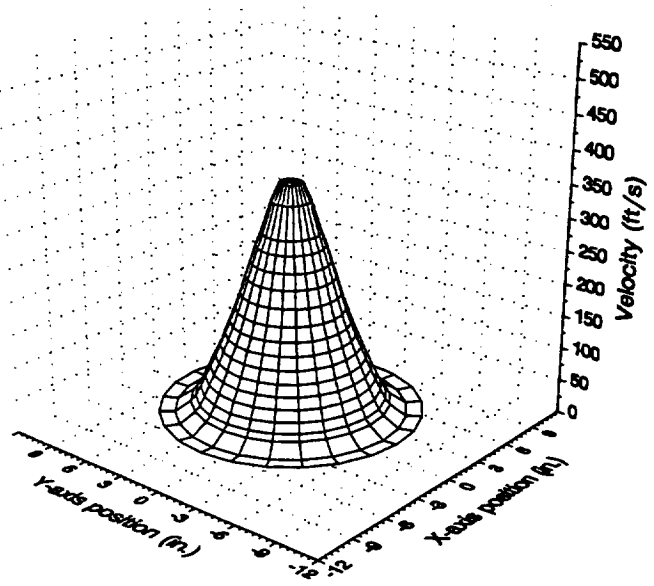

(a)

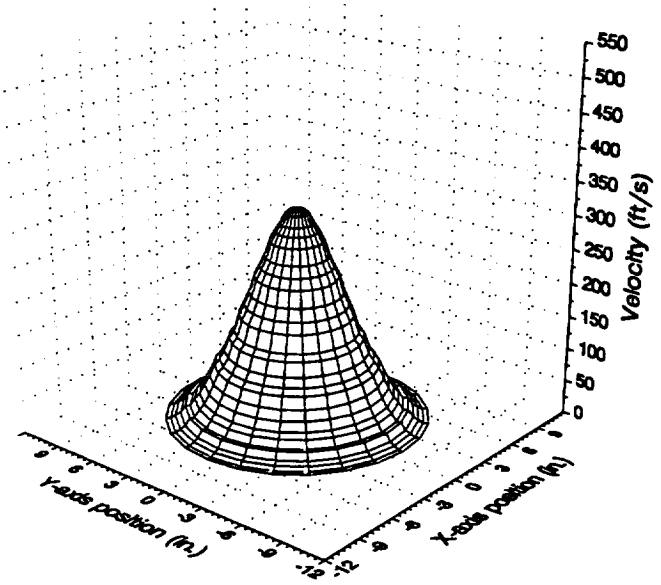

(b)

Figure 40. (a) Velocity profile at seven diameters downstream, z = 31.5 in. (b) Velocity profile at eight diameters downstream, z = 36.0 in.

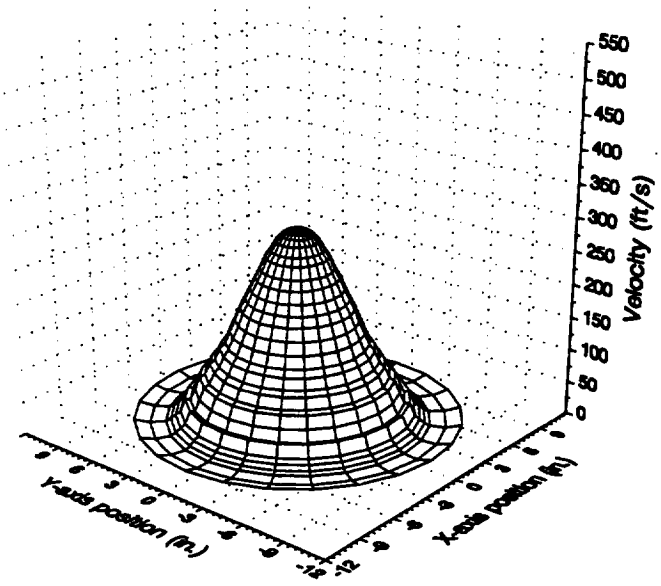

(a)

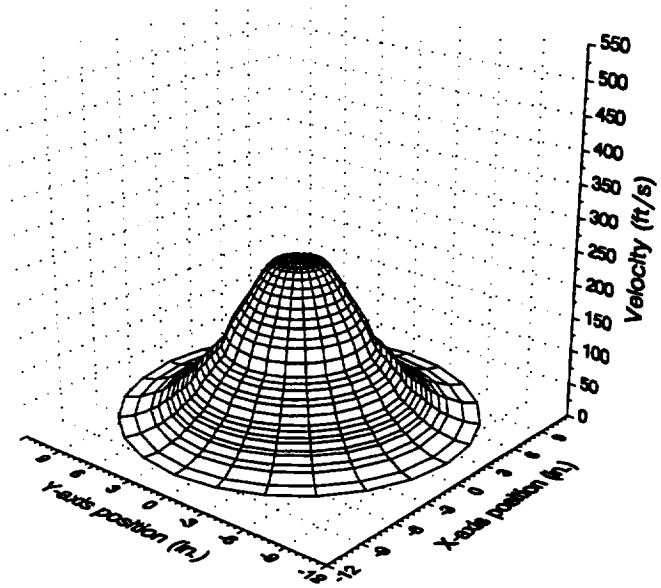

(b)

Figure 41. (a) Velocity profile at nine diameters downstream, z = 40.5 in. (b) Velocity profile at ten diameters downstream, z = 45.0 in.

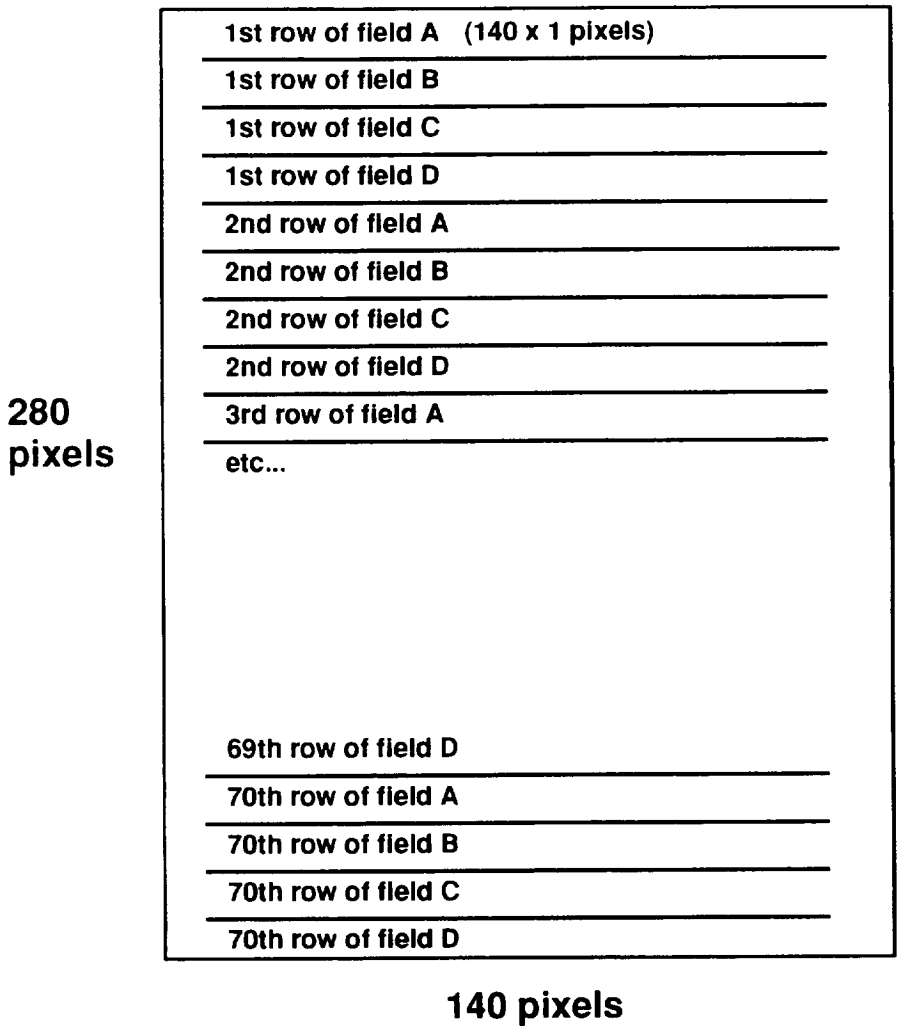

Four "fields" of data, A, B, C, D, each consisting of 140 x 70 pixels, are "interlaced" together to create one "frame" of data of 140 x 280 pixels.

Figure 42. Illustration of the construction of a "field" of data.

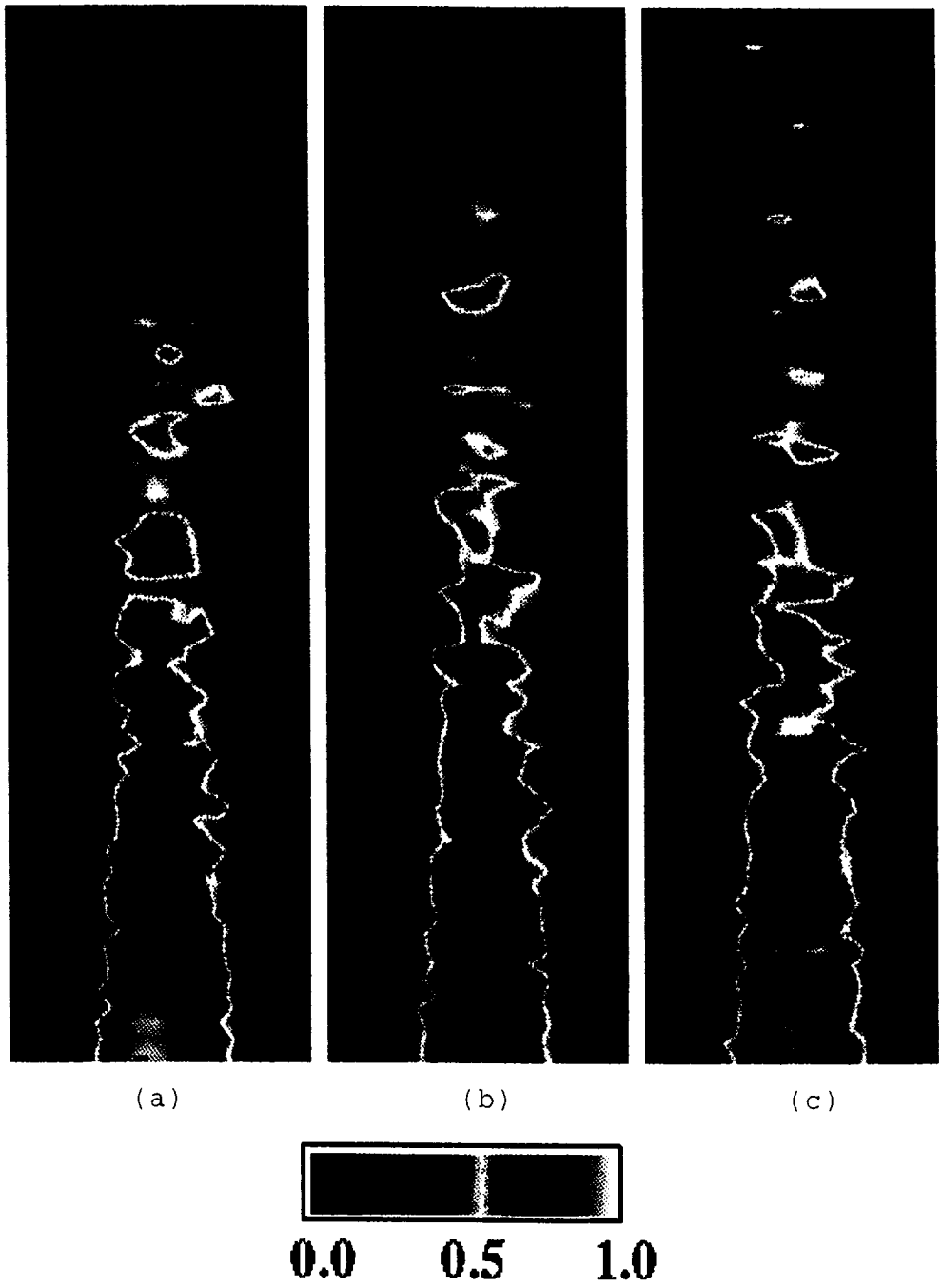

Figure 43. Three consecutively measured fields of filtered MWB infrared data.

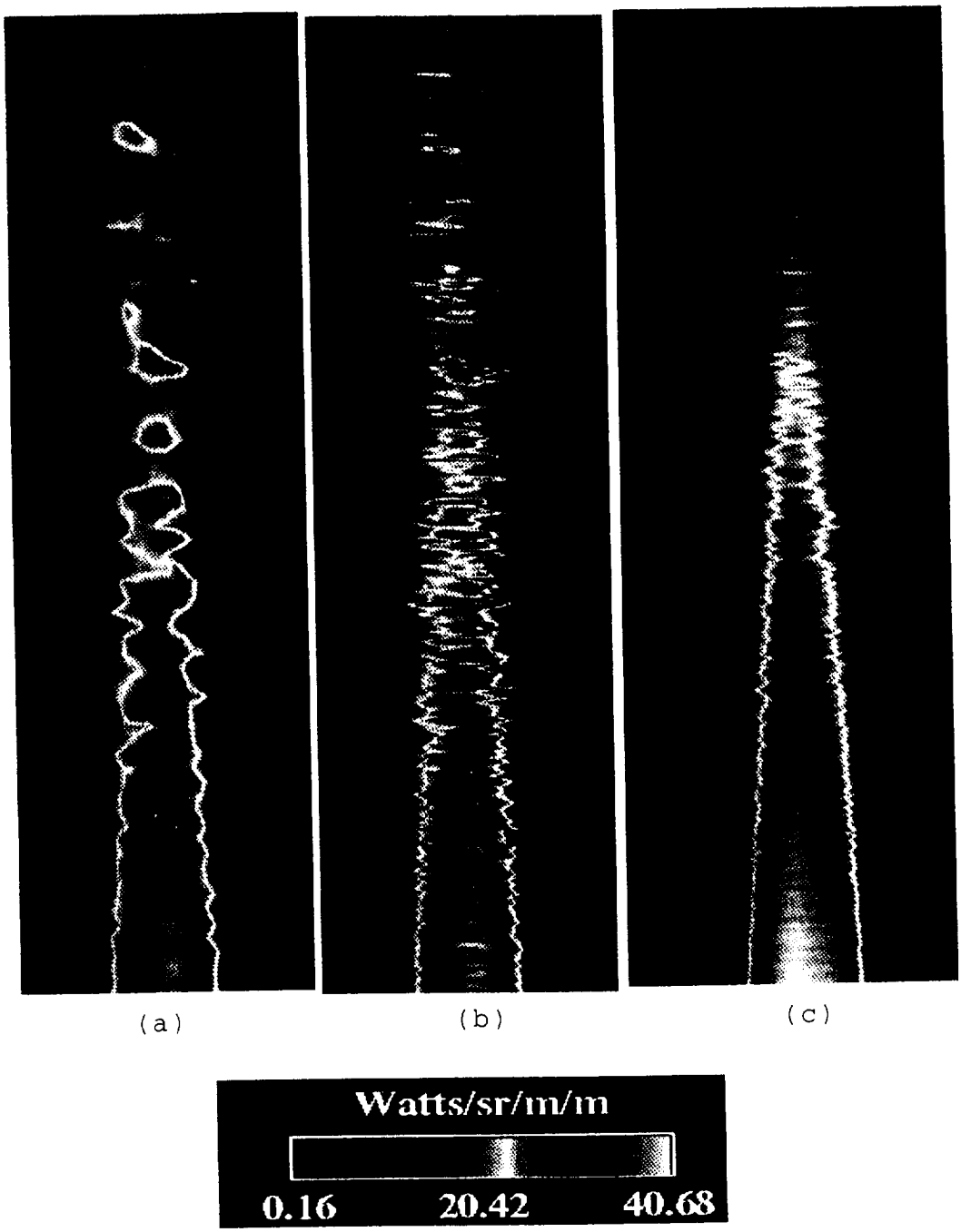

Figure 44. MWB infrared images of the APU exhaust plume.

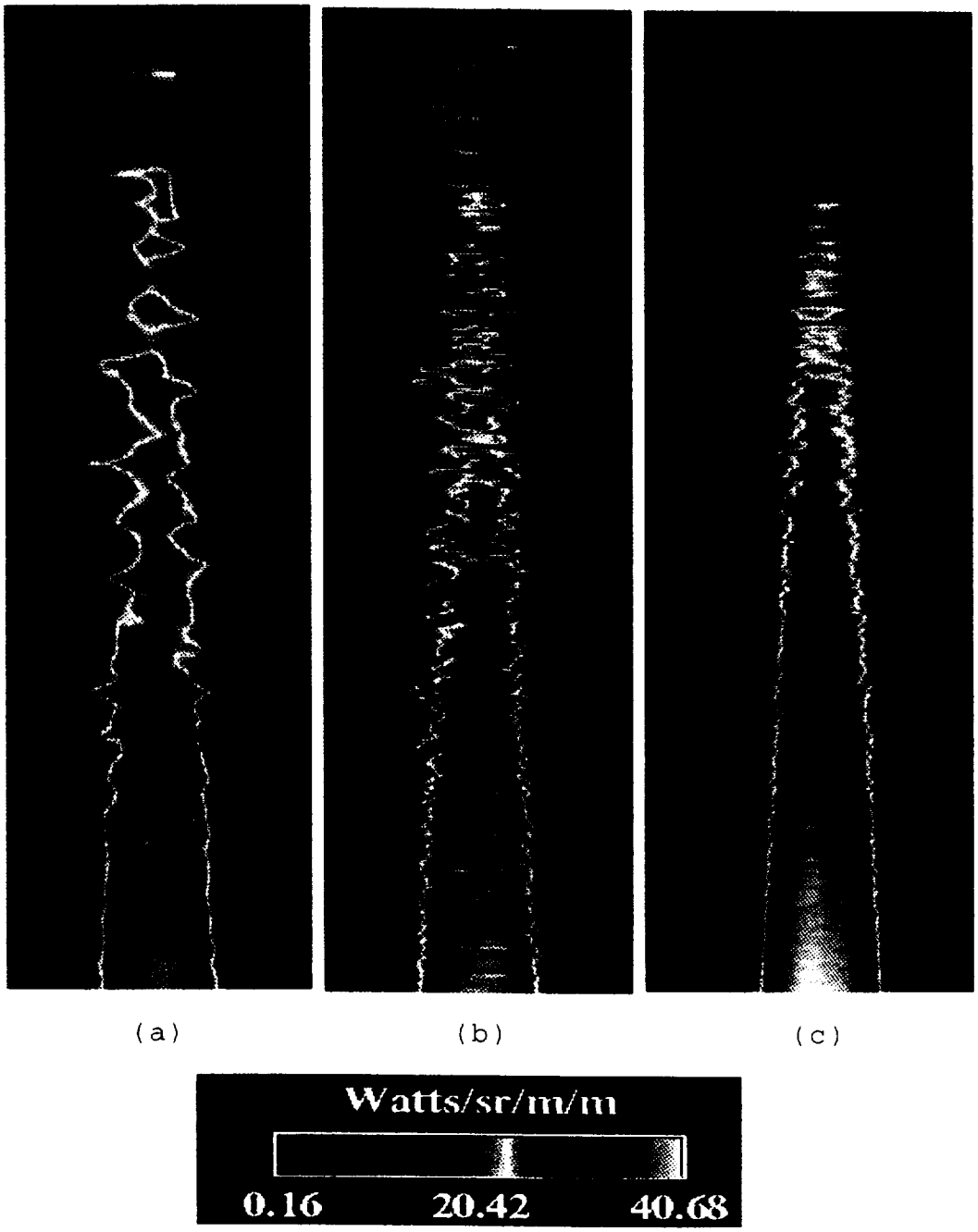

Figure 45. Filtered MWB infrared images of the APU exhaust plume.

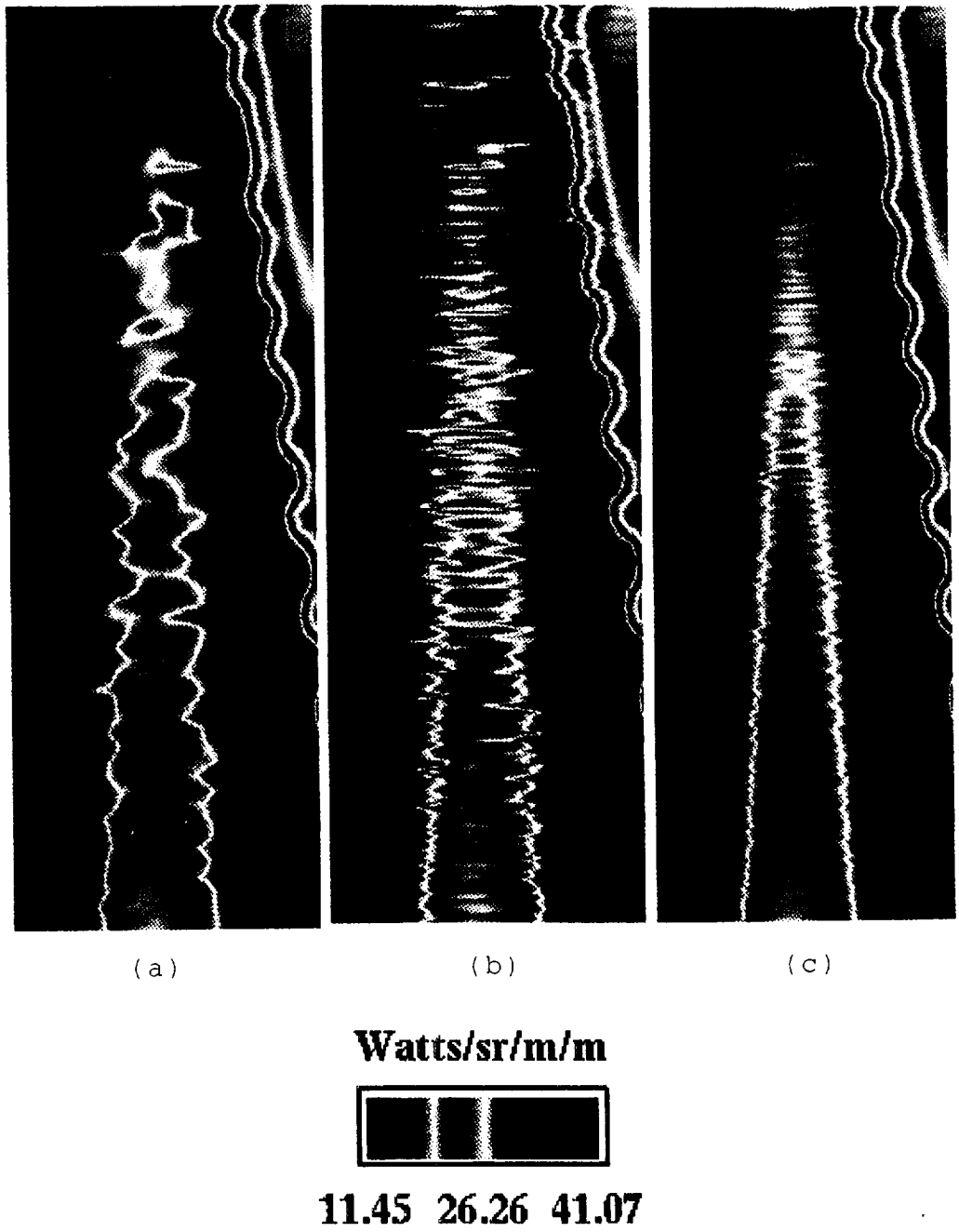

Figure 46. LWB infrared images of the APU exhaust plume.

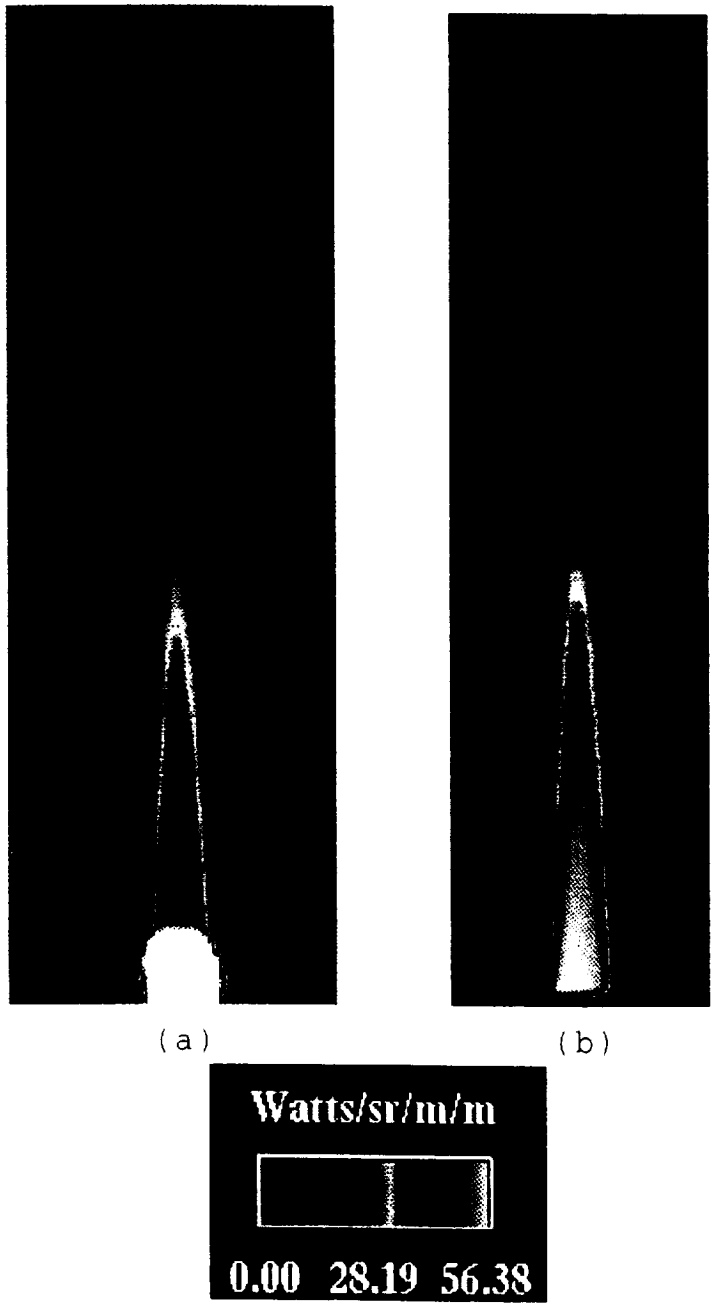

Figure 47. Averaged MWB infrared images of the APU exhaust plume.

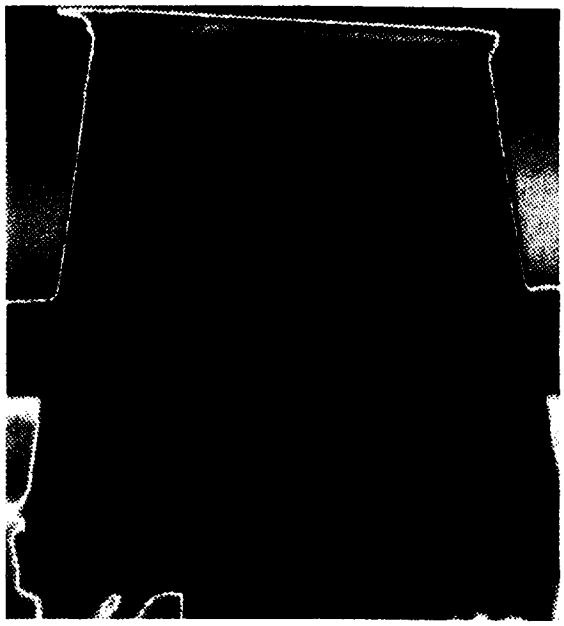

(a)

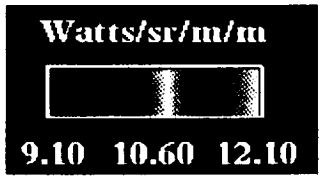

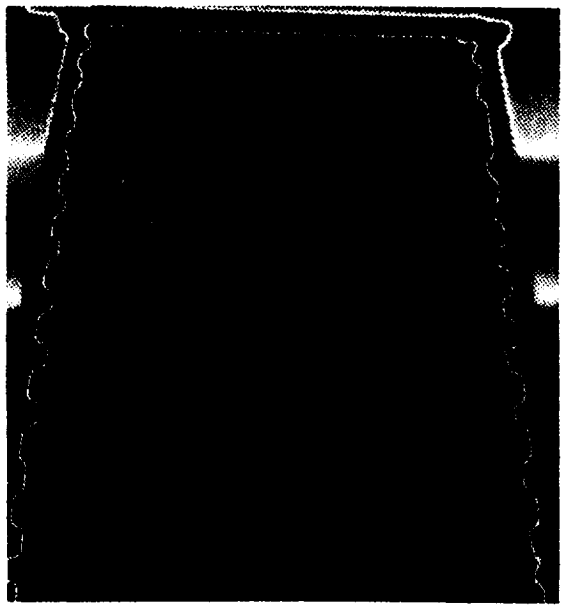

(b)

Figure 48. Infrared images of the aluminized Mylar backdrop.

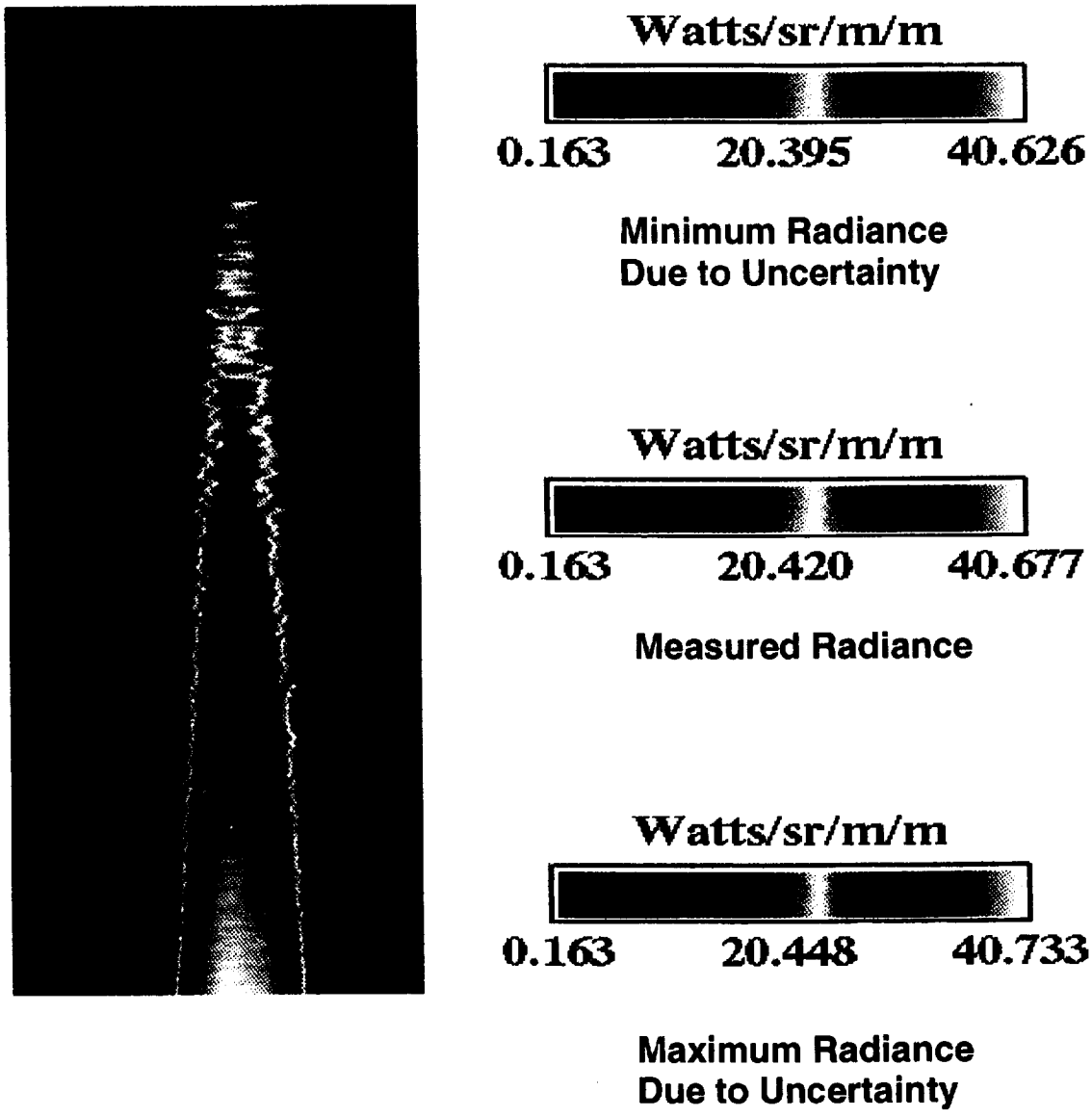

Figure 49. The uncertainty of a measured infrared image.

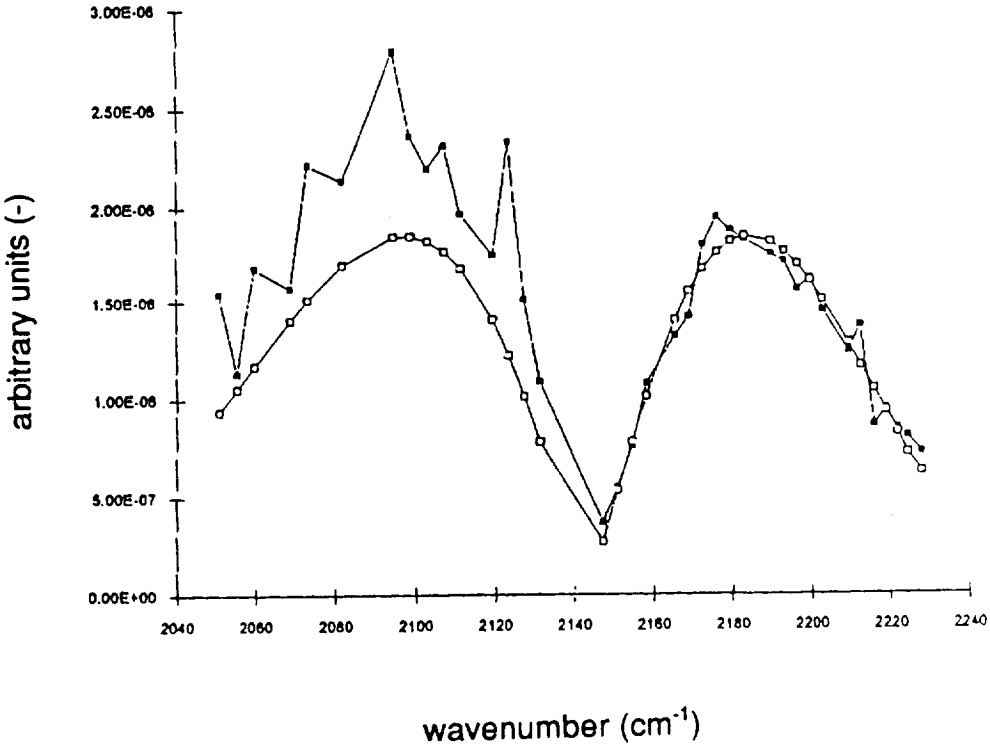

Figure 50. Results from the Midac Spectrometer.

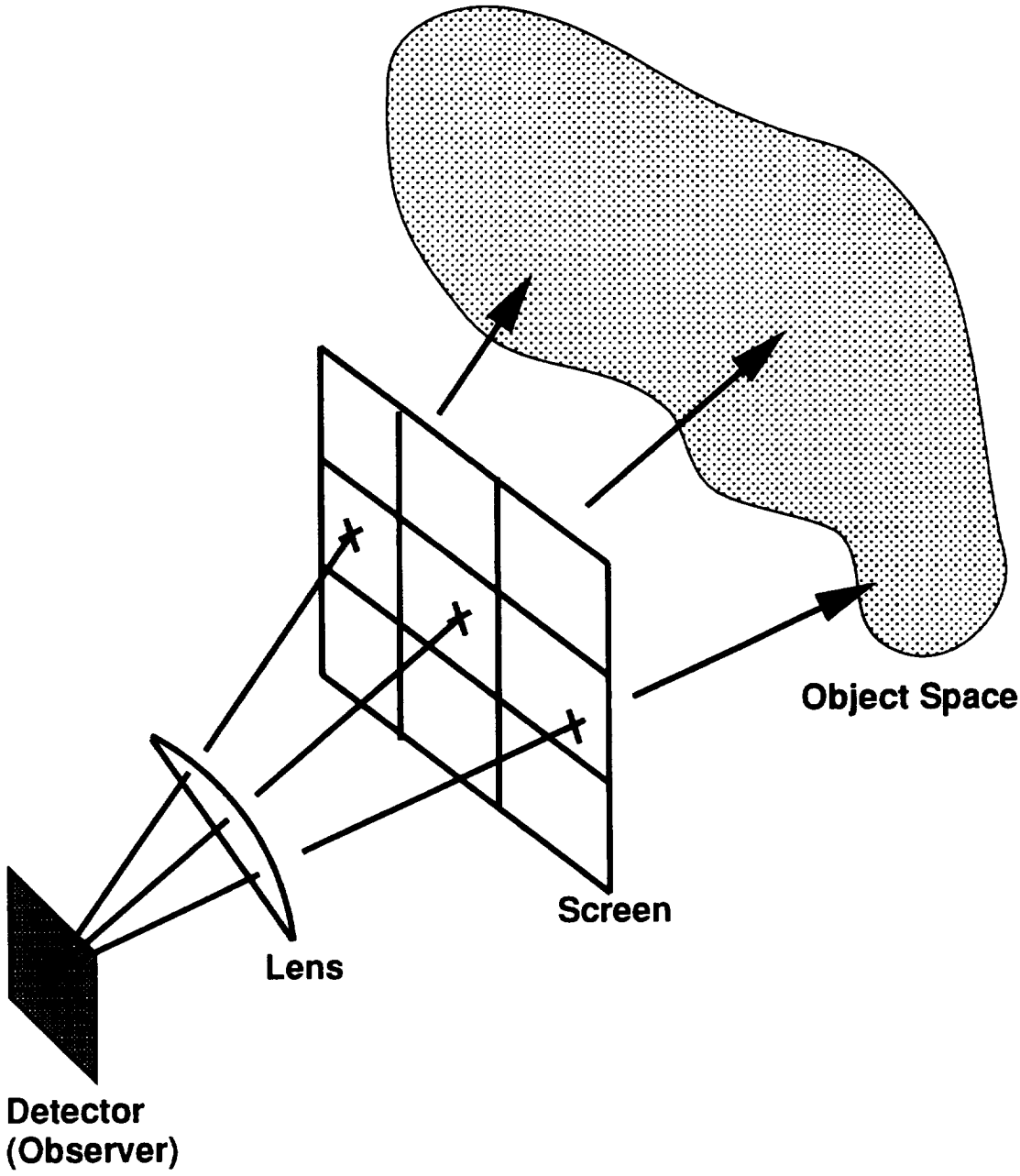

Figure 51. The three-dimensional CFD solution space is reduced to a two-dimensional infrared image by the ray-tracing process.

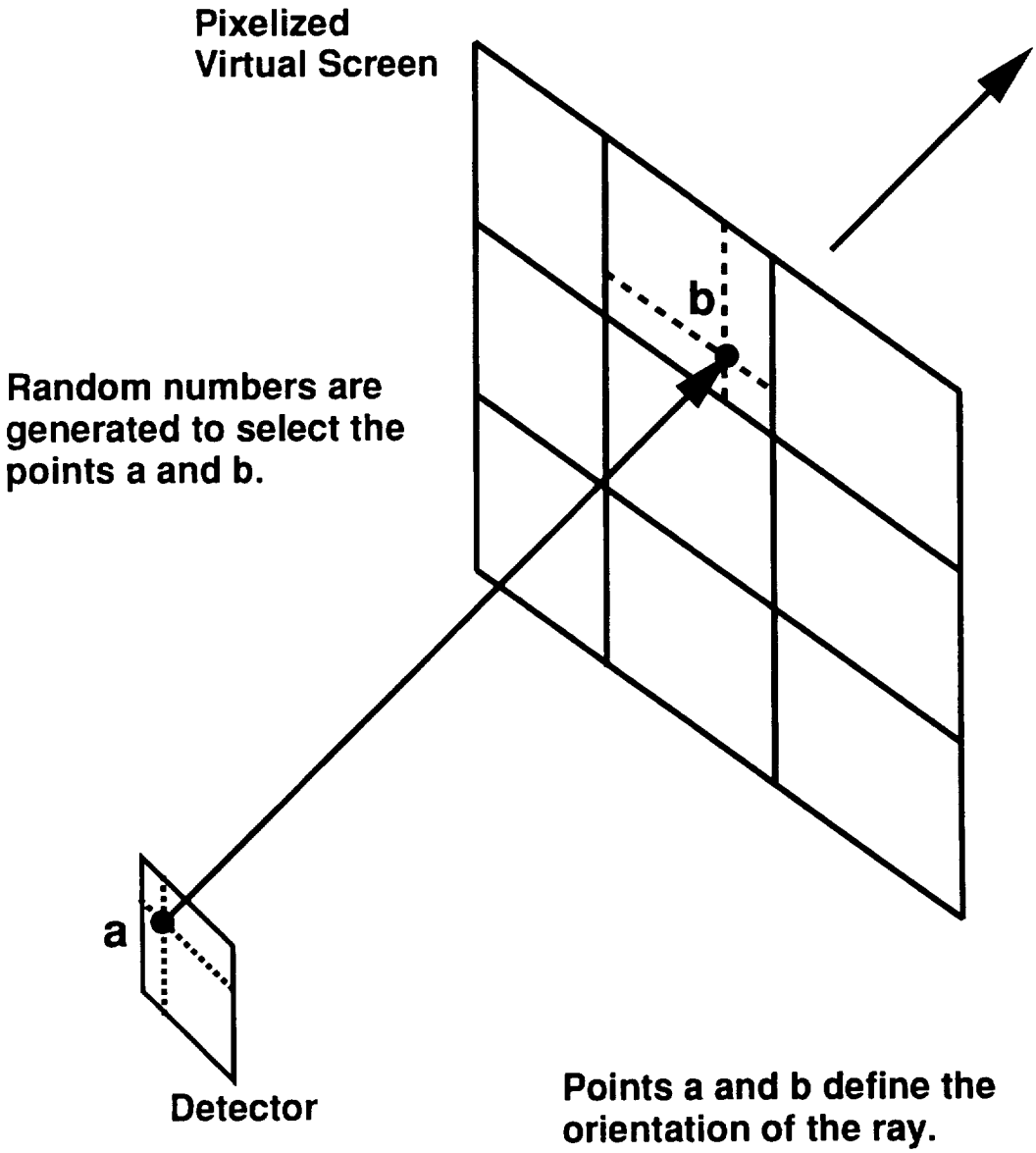

Figure 52. Diagram depicting how the initial orientation of a ray is decided.

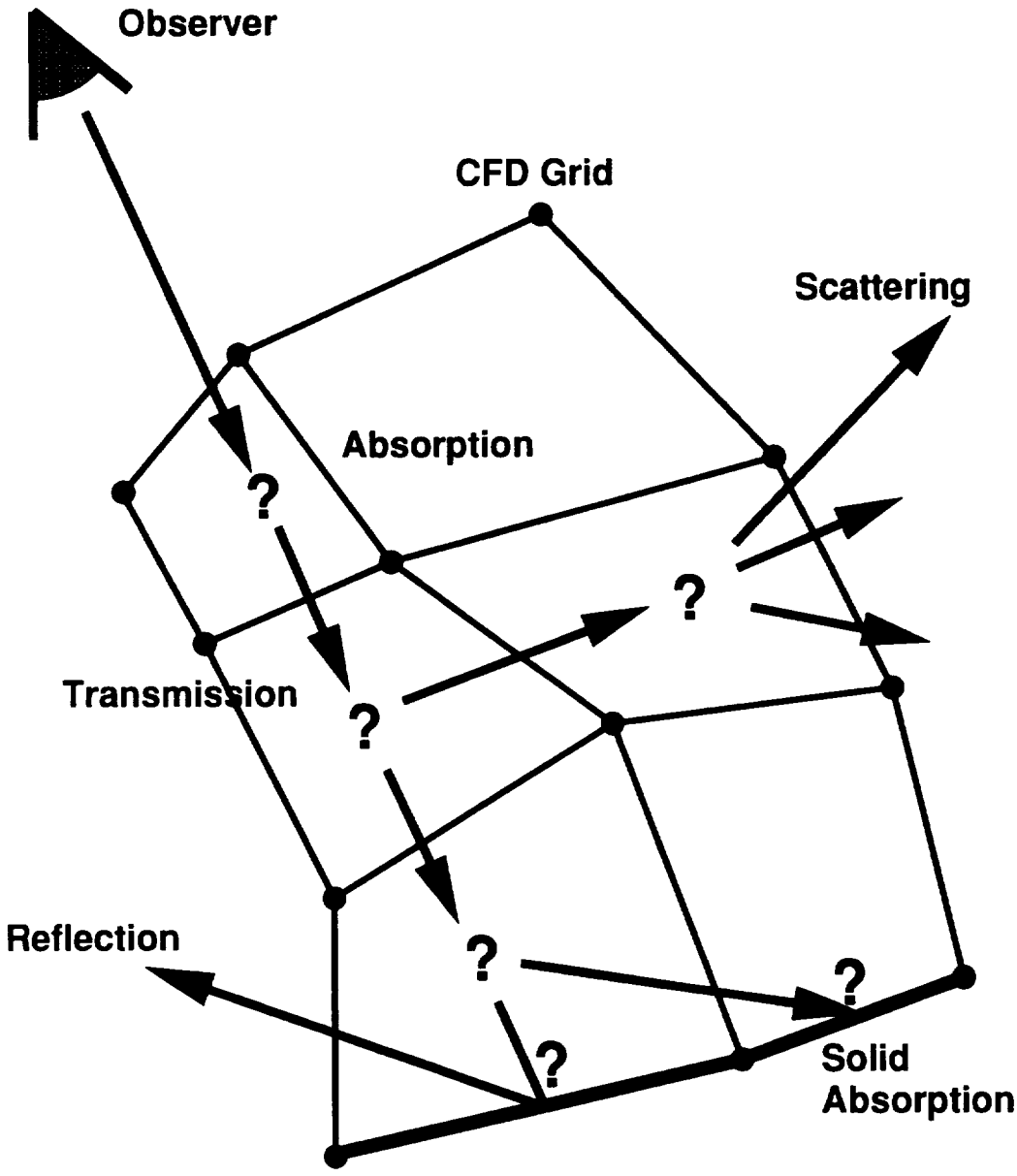

Figure 53. All possible outcomes for a ray as it traverses through the CFD solution space.

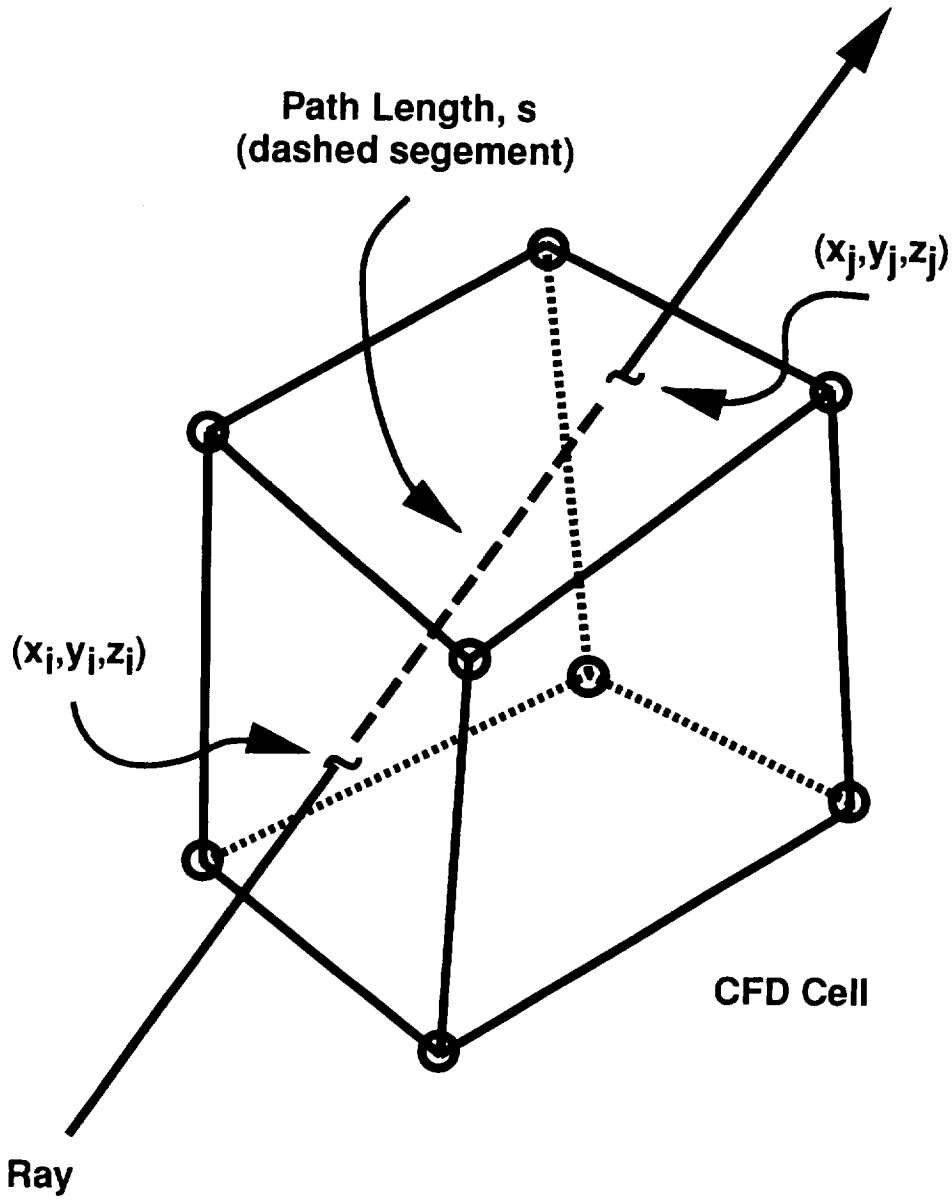

Figure 54. Diagram depicting the path taken by a ray as it traverses a three-dimensional CFD solution cell.

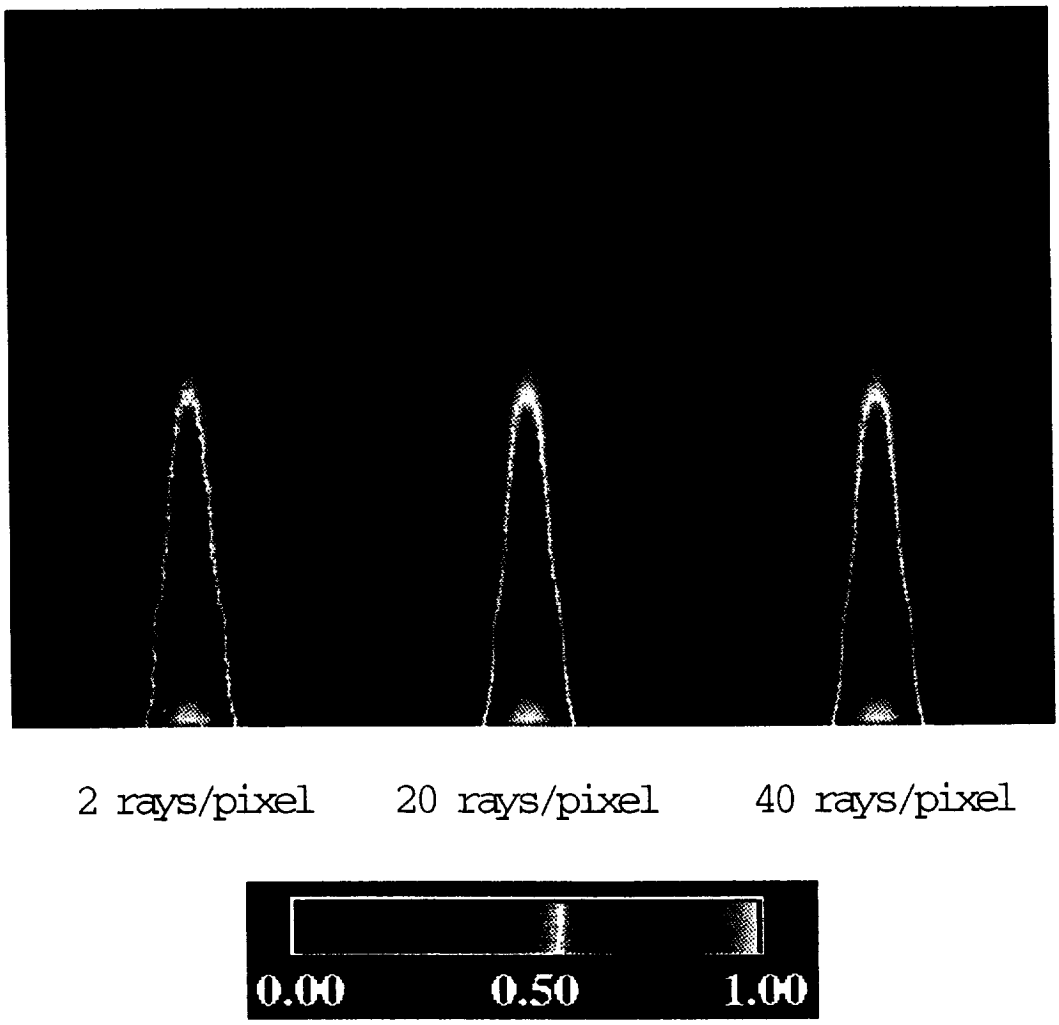

Figure 55. Illustration of the improvement in the quality of a predicted image as the number of rays per pixel increases.

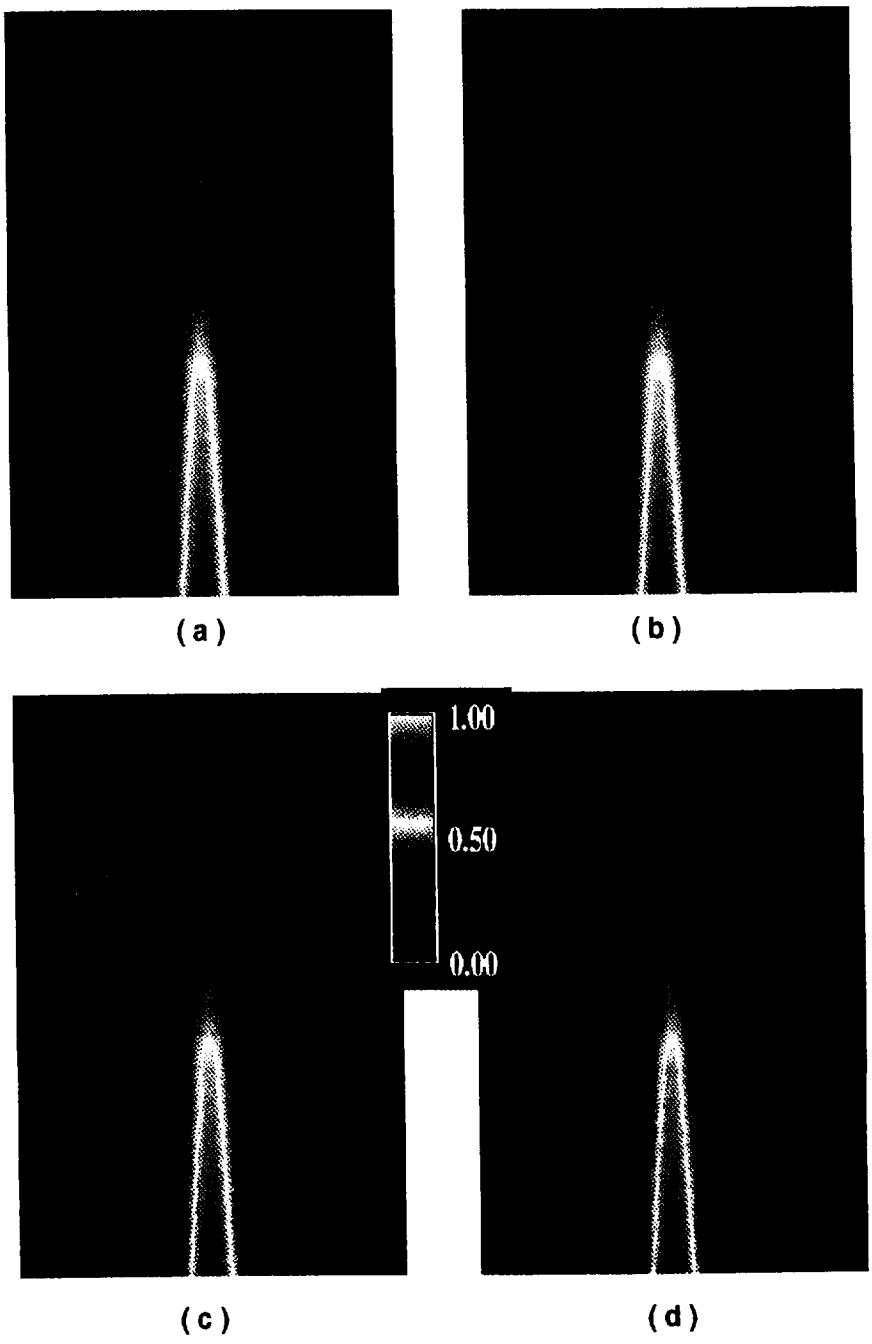

Figure 56. Predicted infrared images depicting the effect of varying the baseline carbon dioxide concentrations.

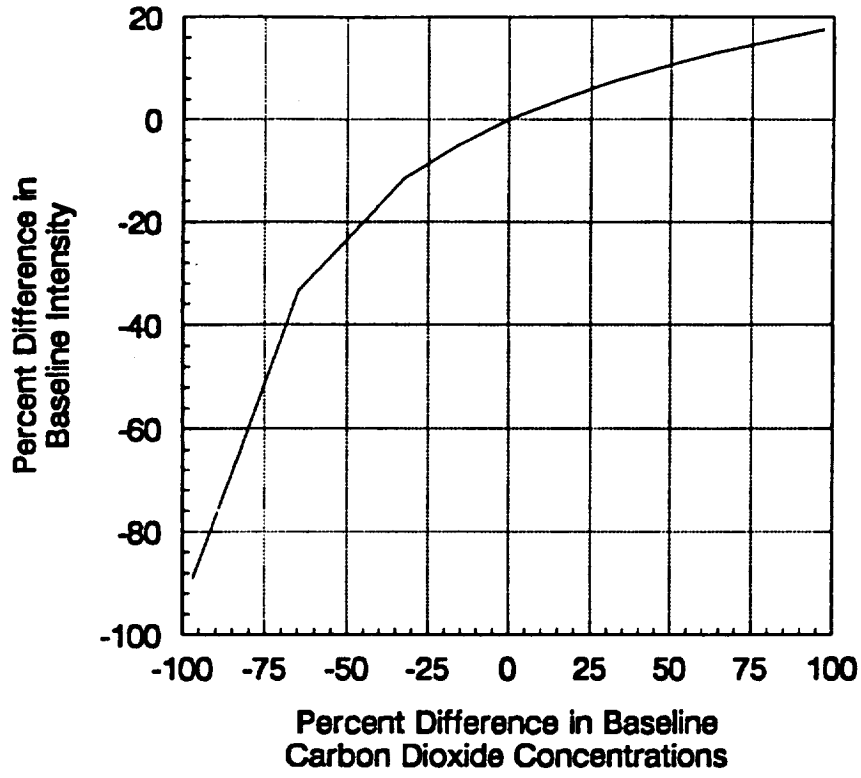

Figure 57. Effect on intensity for a given pixel by varying the baseline carbon dioxide concentrations.

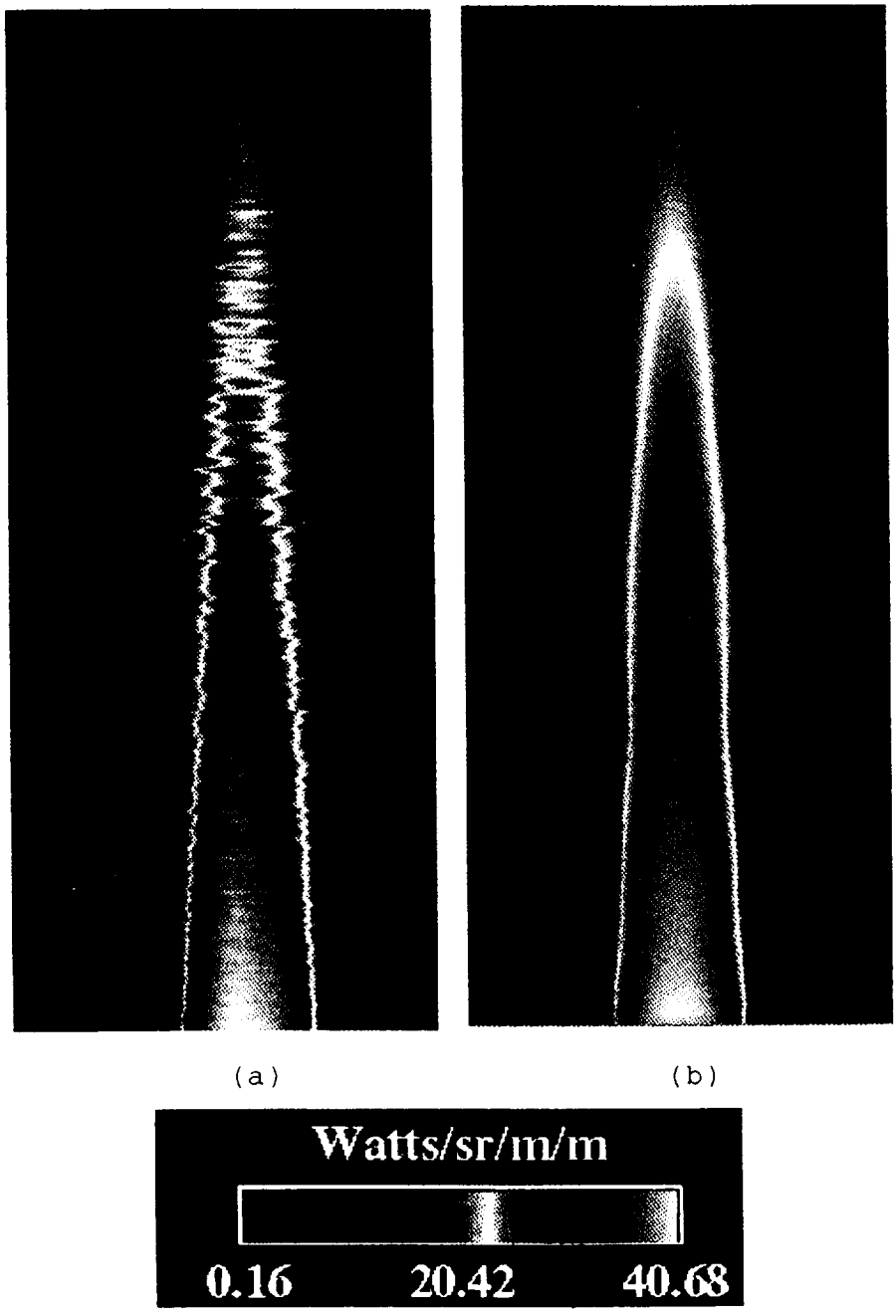

Figure 58. Comparison between an infrared image predicted using the Line of Sight method and an experimental filtered-MWB image averaged over six frames of data.

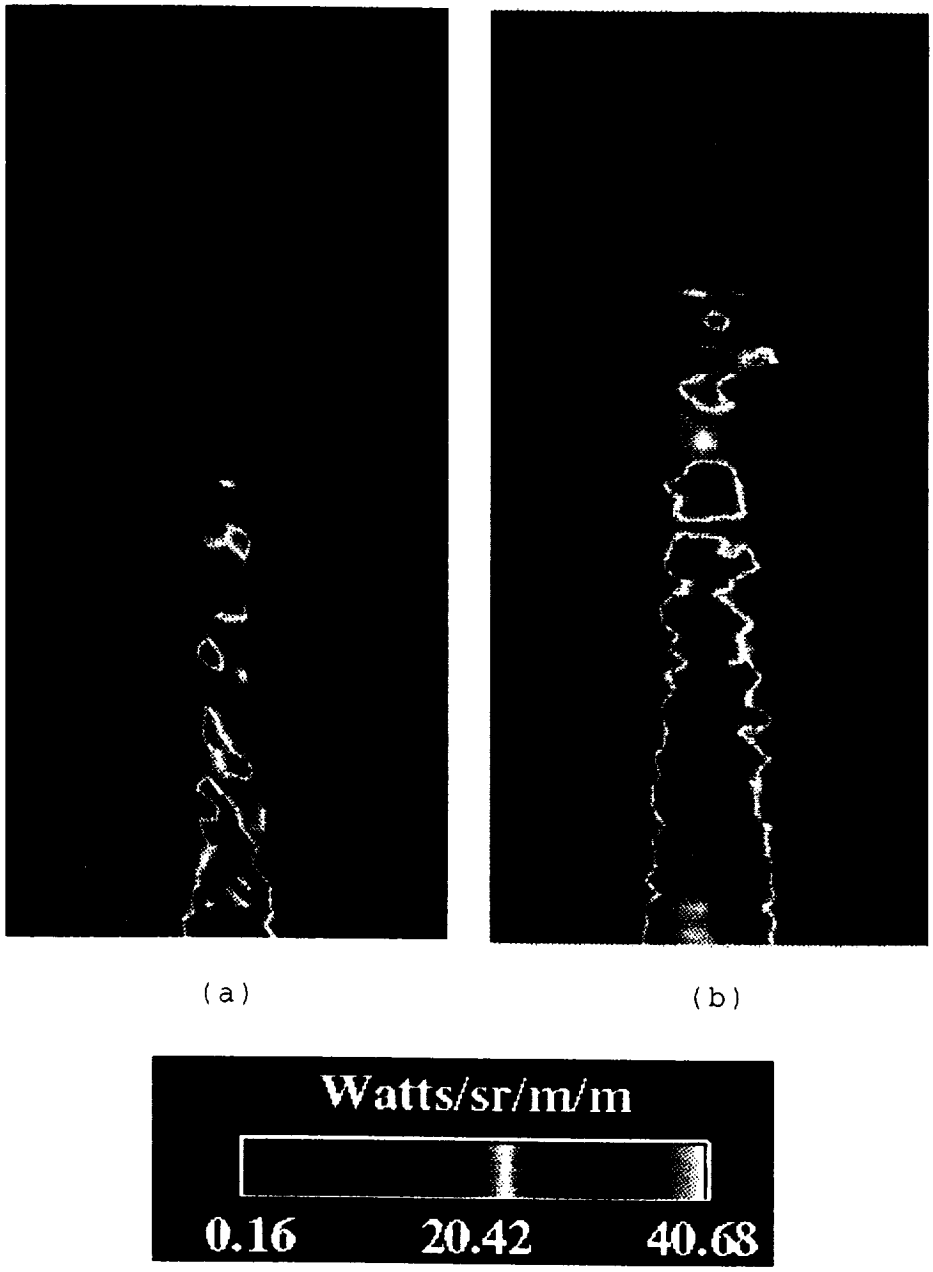

Figure 59. Comparison between an infrared image predicted using the Monte Carlo ray-trace code and an experimental filtered-MWB field of data.

REPORT DOCUMENTATION PAGE

Form Approved
OMB No. 0704-0188

1. AGENCY USE ONLY *(Leave blank)*	2. REPORT DATE	3. REPORT TYPE AND DATES COVERED
	February 1996	Technical Memorandum

4. TITLE AND SUBTITLE

Temperature, Pressure, and Infrared Image Survey of an Axisymmetric Heated Exhaust Plume

5. FUNDING NUMBERS

NCC2-691

6. AUTHOR(S)

Edward L. Nelson,* J. Robert Mahan,† Larry D. Birckelbaw, Jeffrey A. Turk, Douglas A. Wardwell, and Craig E. Hange

7. PERFORMING ORGANIZATION NAME(S) AND ADDRESS(ES)

Ames Research Center
Moffett Field, CA 94035-1000

8. PERFORMING ORGANIZATION REPORT NUMBER

A-961055

9. SPONSORING/MONITORING AGENCY NAME(S) AND ADDRESS(ES)

National Aeronautics and Space Administration
Washington, DC 20546-0001

10. SPONSORING/MONITORING AGENCY REPORT NUMBER

NASA TM-110382

11. SUPPLEMENTARY NOTES

Point of Contact: Edward L. Nelson, Ames Research Center, MS 237-7, Moffett Field, CA 94035-1000
(415) 604-1507

*Defense Group Inc., Moffett Field, California. †Virginia Polytechnic Institute and State University, Blacksburg, Virginia.

12a. DISTRIBUTION/AVAILABILITY STATEMENT

Unclassified — Unlimited
Subject Category 37

12b. DISTRIBUTION CODE

13. ABSTRACT *(Maximum 200 words)*

The focus of this research is to numerically predict an infrared image of a jet engine exhaust plume, given field variables such as temperature, pressure, and exhaust plume constituents as a function of spatial position within the plume, and to compare this predicted image directly with measured data. This work is motivated by the need to validate Computational Fluid Dynamic (CFD) codes through infrared imaging. The technique of reducing the three-dimensional field variable domain to a two-dimensional infrared image invokes the use of an inverse Monte Carlo ray trace algorithm and an infrared band model for exhaust gases.

This report describes an experiment in which the above-mentioned field variables were carefully measured. Results from this experiment, namely tables of measured temperature and pressure data, as well as measured infrared images, are given. The inverse Monte Carlo ray trace technique is described. Finally, experimentally obtained infrared images are directly compared to infrared images predicted from the measured field variables.

14. SUBJECT TERMS	15. NUMBER OF PAGES
Infrared imaging, Radiation heat transfer, Axisymmetric exhaust plume	146
	16. PRICE CODE: A07

17. SECURITY CLASSIFICATION OF REPORT	18. SECURITY CLASSIFICATION OF THIS PAGE	19. SECURITY CLASSIFICATION OF ABSTRACT	20. LIMITATION OF ABSTRACT
Unclassified	Unclassified		